UNIVERSIDADE ESTADUAL PAULISTA
"JÚLIO DE MESQUITA FILHO"
Campus de Ilha Solteira

UNIVERSIDADE ESTADUAL PAULISTA "JÚLIO DE MESQUITA FILHO"

CAMPUS DE ILHA SOLTEIRA

DEPARTMENT OF ELECTRICAL ENGINEERING

High gain approach and sliding mode control applied to quadrature interferometer

Abordagem de alto ganho e controle de modos deslizantes aplicados ao interferômetro de quadratura

Luiz Henrique Vitti Felão

Ilha Solteira
2019

Luiz Henrique Vitti Felão

High gain approach and sliding mode control applied to quadrature interferometer

Abordagem de alto ganho e controle de modos deslizantes aplicados ao interferômetro de quadratura

Thesis presented to the post-graduation course of the Engineering Faculty of Ilha Solteira – FEIS – UNESP to obtain the Ph.D grade in Electrical Engineering.

Specialty: Automation.

Advisor: Prof. Dr. Cláudio Kitano

Ilha Solteira

2019

FICHA CATALOGRÁFICA
Desenvolvido pelo Serviço Técnico de Biblioteca e Documentação

F48h

Felão, Luiz Henrique Vitti.
High gain approach and sliding mode control applied to quadrature interferometer / Luiz Henrique Vitti Felão. -- Ilha Solteira: [s.n.], 2019
113 f. : il.

Tese (doutorado) - Universidade Estadual Paulista. Faculdade de Engenharia de Ilha Solteira. Área de conhecimento: Automação, 2019

Orientador: Cláudio Kitano
Inclui bibliografia

1. Interferometria óptica. 2. Interferômetro de quadratura. 3. Controle por modos deslizantes.

João Josué Barbosa
Serviço Técnico de Biblioteca e Documentação
Diretor Técnico
CRB 8-5642

unesp

UNIVERSIDADE ESTADUAL PAULISTA

Câmpus de Ilha Solteira

CERTIFICADO DE APROVAÇÃO

TÍTULO DA TESE: HIGH GAIN APPROACH AND SLIDING MODE CONTROL APPLIED TO QUADRATURE INTERFEROMETER

AUTOR: LUIZ HENRIQUE VITTI FELÃO
ORIENTADOR: CLAUDIO KITANO

Aprovado como parte das exigências para obtenção do Título de Doutor em ENGENHARIA ELÉTRICA, área: Automação pela Comissão Examinadora:

Claudio Kitano
Prof. Dr. CLAUDIO KITANO
Departamento de Engenharia Elétrica / Faculdade de Engenharia de Ilha Solteira

Prof. Dr. MARCELO CARVALHO MINHOTO TEIXEIRA
Departamento de Engenharia Elétrica / Faculdade de Engenharia de Ilha Solteira

Prof. Dr. RICARDO TOKIO HIGUTI
Departamento de Engenharia Elétrica / Faculdade de Engenharia de Ilha Solteira

Prof. Dr. JOSEMIR COELHO SANTOS
Departamento de Engenharia de Energia e Automação Elétrica / Universidade de São Paulo

Prof. Dr. GILDER NADER
Centro de Metrologia de Fluidos / Instituto de Pesquisas Tecnológicas do Estado de São Paulo

Ilha Solteira, 29 de julho de 2019

Abstract

Interferometers are extremely sensitive measurement devices, which use the principle of interference between two or more sources of light to generate a pattern of constructive and destructive interference. This pattern contains information about the physical phenomenon under study, and their light intensity can be used to calculate the optical path difference traveled by the two beams. The optical path difference and light intensity relationship is given by a cosine type function. Large disturbances can change the interferometer operation point, reaching nonlinear regions of the interferometric curve and even inducing ambiguities due to the periodicity of the input/output relationship. The present work concerns with the modeling, development and application of a control strategy based on sliding mode control, in a two-beam quadrature interferometer. It was used the high gain approach, which consists in to fully compensate the phase shifts induced on the sensor arm with the control system, in such a way that the voltage control signal becomes proportional to the phase disturbances. Therefore, the demodulation process does not require phase unwrapping algorithms. This implemented system showed capability to improve dynamic range and bandwidth when compared with other control systems in literature that were based on different high gain approach topologies. Also a new method of interferometric phase demodulation is proposed allying this control strategy to a virtual emulated interferometer. This allows keeping the real interferometer in open-loop and retrieving the phase shift information from the control signal of the virtual closed-loop interferometer, thus leading to considerable simplification of the required instrumentation. An ellipse fitting algorithm was applied to the system, allowing the correction of the Lissajous figure formed by both output interferometric signals from an ellipse to a unitary circle. Therefore, the system estimates the phase shift even with quadrature mismatches. Inertial sensors such as accelerometers and gyroscopes can benefit from this system in two major points: first, the sensitivity can be increased without limiting the end of scale of the sensor due to the proportional relation of the voltage control signal and the measured phase shift; and second, the system can be implemented without the need of PZT feedback actuators or modulators and PZT driven circuitry, reducing cost, volume and weight of the sensors.

Key-words: Optical interferometry. Quadrature interferometer. Sliding mode control.

Resumo

Interferômetros são dispositivos de medição extremamente sensíveis, os quais utilizam o princípio de interferência entre duas ou mais fontes de luz para gerar um padrão de interferência construtiva e destrutiva. Este padrão contém informação sobre os fenômenos físicos sob estudo, e sua intensidade luminosa pode ser usada para calcular a diferença de caminho óptico acumulada pelos dois feixes de luz. A diferença de caminho óptico e a intensidade de luz são relacionadas por uma função cossenoidal. Grandes distúrbios podem alterar o ponto de operação do interferômetro, alcançando regiões não lineares da curva característica do interferômetro e até mesmo induzindo ambiguidades, devido à periodicidade da relação entrada/saída. Este trabalho preocupou-se com o modelamento, desenvolvimento e aplicação de uma estratégia de controle baseada em controle com modos deslizantes, em um interferômetro de dois feixes em quadratura. Foi utilizada a abordagem de alto ganho, a qual consiste em utilizar o sistema de controle para compensar completamente os deslocamentos de fase induzidos no braço sensor, de tal forma que o sinal de controle se relaciona com os deslocamentos de fase por uma equação de reta. Portanto o processo de demodulação não necessita de algoritmos de desdobramento de fase. O sistema implementado mostrou capacidade de melhorar a faixa dinâmica e largura de banda quando comparado com outros sistemas de controle na literatura, também baseados na abordagem de alto ganho. Destaca-se que um algoritmo de identificação de elipse foi aplicado no sistema, permitindo a correção da figura de Lissajous formada pelos sinais de saída do interferômetro, de uma elipse para um círculo. Portanto, o sistema estima o deslocamento de fase mesmo com erros na condição de quadratura. Um novo método de demodulação de fase óptica é proposto, aliando esta estratégia de controle com um interferômetro emulado virtualmente. Isto permite manter o interferômetro físico em malha aberta e recuperar a informação de deslocamento de fase a partir do sinal de controle do interferômetro virtual, trazendo considerável simplificação da instrumentação requerida. Sensores inerciais tais como acelerômetros e giroscópios podem se beneficiar deste sistema em dois pontos principais: a sensitividade pode ser aumentada sem limitar o fim de escala do sensor devido à relação proporcional entre o sinal de controle e o deslocamento de fase medido; o sistema pode ser implementado sem a necessidade de moduladores e circuitos de acionamento de PZT, reduzindo o custo, volume e peso.

Palavras-chave: Interferometria óptica. Interferômetro de quadratura. Controle com modos deslizantes.

Dedicated to

Antônia Argentina Vitti Monteiro (*in memoriam*) and Newton Rodrigues Felão (*in memoriam*), whose examples of life have shaped my family by teaching empathy and that with humility one always goes further

Acknowledgements

For those who have shaped my character, my parents Newton and Adélia, sister Isadora, grandmother Jeanette and our entire family. My greatest pride is the love that exists in our family, for being a safe harbor I thank you all.

To Professor Dr. Cláudio Kitano, my advisor, from who I admire the inteligence, competency and professionalism. Thank you very much for accepting me as a doctorate student and for the many lessons. Your dedication is inspiring.

To Professor Dr. Marcelo Carvalho Minhoto Teixeira, without which this work would not have been done, your companionship, suggestions and solidarity influenced me directly. I am grateful for all the learning that I had with you.

To Professor Dr. João Marcos Salvi Sakamoto, for welcoming me into IEAv, believing in me, in our work. For their help and friendship, my heartfelt thanks!

To Professor Dr. Aparecido Augusto de Carvalho, who had a fundamental participation in my formation.

To the friends from our student house, Renan, André, Vander, Marcelo, Joao Carlos, Denis, Joao Gabriel, Manuel, Igor and Dona Jaci, who together formed a second family and a place that I can also call home. Thank you very much.

To laboratory friends Stephany, Joao Paulo, Andryos, Flavio, Galeti, Angel, Guilherme, Gabriel, Renato and Roberta, for the teachings, suggestions, coffees, moments of hard work and also relaxation. You were part of this walk and for that I will be forever grateful. Also to Unesp's servers and employees, in particular to friends, Adilson, Aderson, Hidemassa, Wendel, Chaves and Everaldo, always willing to help! To the great friends Pedro R. Cleto, Bruno J. Silveira and Thiago R. Pentiado, for their strong friendship and companionship.

I would also like to thank FAPESP - São Paulo State Research Support Foundation (Process No. 2017 / 17235-1) for the essential financial support for this research.

“Going in one more round when you don’t think you can, that’s what makes all the difference in your life.” Rocky Balboa

List of Figures

List of Tables

Contents

1 Introduction

The literature about interferometry is a wide and vast subject, since it has been used as a laboratory technique for almost a hundred years. Several developments have increased the accuracy and extended the range of applications of optical interferometry. The most significant of these developments was the advent of the laser in 1960, when, for the first time, an intense source of light, with a remarkably high degree of spatial and temporal coherence became available (HARIHARAN, 2003).

Optical interferometry can be described as a measurement technique, which is based on a phase shift on the electromagnetic field of one beam of light, produced by a physical quantity to be measured. In general, the detection of electromagnetic field phase in optical frequencies (Terahertz) is a nontrivial and prohibitive task, due to the lack of instrumentation capable to operate in such high frequencies. Combining this phase shifted beam with another beam of light (used as a reference of phase), the relative phase can be estimated from the optical intensity, measured with conventional instrumentation, such as quadratic law photodetectors allied to a transimpedance circuit.

The interference phenomenon that occurs with the overlapping of two or more light beams can cause maximum and minimum points of optical intensity as a result of constructive and destructive interference between the different light beams. These intensity distributions are called interference fringes (UDD; SPILLMAN, 2011).

When both light beams of the interferometer have the same wavelength, it is called homodyne interferometer, and when the phase shifted and the reference beams have different wavelengths, it is called heterodyne interferometer.

The main advantage of interferometric sensors comes from their extremely high sensitivity, when compared to other matured sensor technologies. Adversely, this quality is also their main drawback, since they are more susceptible to spurious disturbances which, allied with the nonlinear nature of the interferometer characteristic curve, can cause signal fading (UDD; SPILLMAN, 2011; SHEEM *et al*., 1982), as well as ambiguity of results and direction (CHEN *et al*., 2014). This behavior usually leads to nontrivial procedures to extract the signal of interest, due to the complexity of the signal demodulation process, since it is phase-modulated with a superimposed fading signal.

It will be presented in Chapter 2 that the two-beam homodyne interferometric characteristic curve can be expressed as:

$$I(t) = \frac{I_0}{2}\{1 + Vcos[\Delta\phi(t) + \phi_0]\}, \quad (1)$$

where $I(t)$ is the optical intensity output, I_0 is the optical intensity of the laser beam in the input of the interferometric system and $\Delta\phi(t)$ is the phase shift related with the physical quantity to be measured. Factor V is the fringe visibility, a parameter that varies in the range of 0 up to 1 and takes in account the parallelism between the electrical field and polarization of the two combining beams and their optical intensities. The parameter ϕ_0 ideally is a static phase shift related to the difference between the lengths of the interferometer arms.

When the static phase shift ϕ_0 is equal to $\left(\pm\frac{\pi}{2} + 2k\pi\right)$ rad, for $k \in \mathbb{Z}$, the interferometer operates at its maximum sensitivity points. As it can be seem in Figure 1, where $\Psi = \Delta\phi + \phi_0$, these operation points are located at the center of the quasi-linear regions of the cosine characteristic curve and, consequently, for interest signals $\Delta\phi$ with amplitudes much smaller than $\frac{\pi}{2}$ rad, the output optical intensity can be considered proportional to $\Delta\phi$.

Figure 1 - Interferometric characteristic curve.

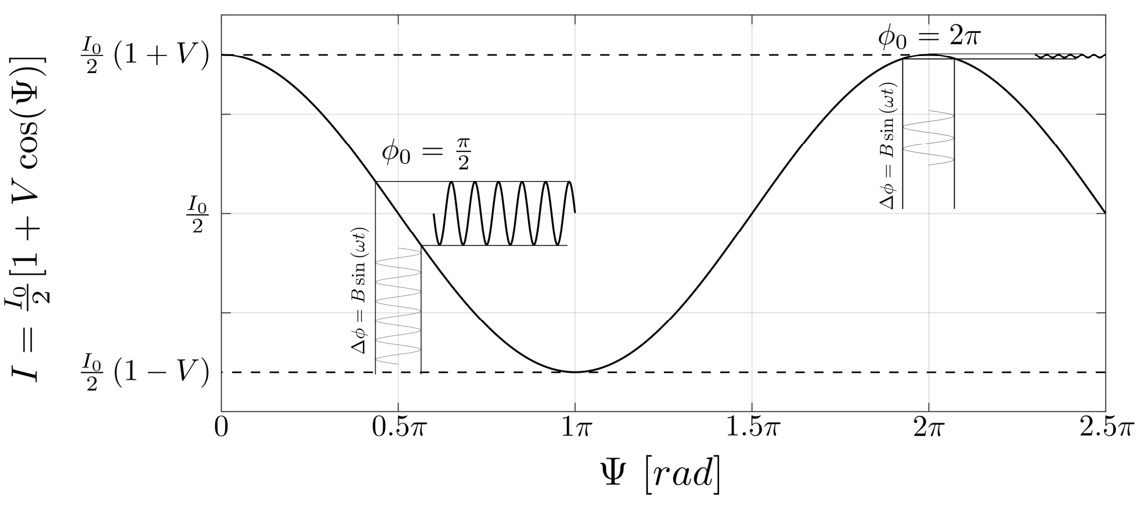

Source: (Modified from MARTIN, 2018)

In an ideal case, ϕ_0 should be constant. However, due to the real-world spurious disturbances over the interferometer, caused by environmental changes, such as, temperature variation (even on the scale of micro kelvin), weak mechanical vibration and air turbulence, it is actually a quasi-static quantity (whose variation usually occurs bellow 20 Hz approximately). Because of this, in practice, it is observed that in a few seconds the amplitude of this drift can easily reach the order of 2π rad or greater (SHEEM *et al.*, 1982). Eventually the drift of ϕ_0 may lead the operation point of the interferometer to $k\pi$ rad, for $k \in \mathbb{Z}$, therefore the operation point may lie in the most nonlinear regions of the characteristic curve. The interferometer input/output relationship in any of these regions distorts and attenuates the output signal, which may vanish (see Figure 1); this phenomenon is known as signal fading.

Another drawback that the nonlinear nature of the interferometric characteristic curve brings is the ambiguity of phase shifts ($\Psi(t)$) direction. As it can be seen in Figure 2, the optical intensity $I(t)$ would be the same, regardless if the phase shift at the input was $\Psi(t)$ or $-\Psi(t)$.

Figure 2 - Interferometric characteristic curve with high modulation depth input signal.

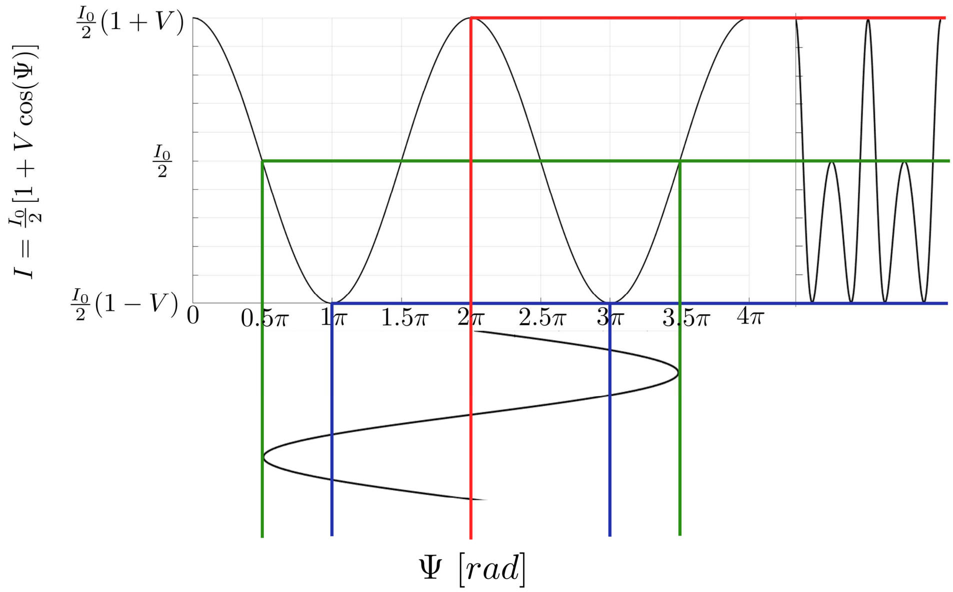

Source: (Modified from MARÇAL, 2008)

Different techniques to overcome the signal fading have been published in literature such as homodyne and heterodyne techniques, with spectral or temporal approaches as well as open-loop or closed-loop methods (UDD; SPILLMAN, 2011).

When using the closed-loop methods, a common and widespread methodology to control nonlinear interferometric systems and avoid the signal fading is to perform the linearization around an operation point by using Taylor series. This approach allows the designer to use the well-developed theory of linear control and, for example, techniques based on root locus, Bode and Nyquist diagrams, and modern control with the description of the system using state space modelling (MELCHIONNI, *et al*., 2015; KARHADE *et al*., 2010; PARK *et al*., 2005). Another interesting approach, sometimes called “feedback interferometry” (SHIRAI et. al, 1999; CHEUNG et. al, 2003), utilizes closed-loop to convert the well-known cosinusoidal input/output curve given by (1) into a saw-tooth profile, where output intensity varies almost linearly within a given interferometer phase range. Works previously reported by some authors (FRITSCH ; ADAMOWSKY, 1981; BASILE *et al*., 1991) presented as main drawbacks of this approach the need for reset circuits and the limitation of operating only in small deviations around the operating point (FLEMMING; ROUTLEY, 2015; CHAO; FA-JIE, 2011), once the control designed for the linearized system can only guarantee local stability.

In the particular case of reset circuits, the reset voltage action will interrupt the measurement function, and this reset glitch can severely compromise the phase detection capability of the sensor temporarily. In many publications, it has been described how to solve this problem by using an optical fiber Michelson interferometer and employing fiber Bragg gratings (FBGs) (XIE *et al*., 2009a; XIE *et al*., 2009b; XIE *et al*., 2009c). However, the reset system is adequate for laboratory conditions but difficult to be used in real-world applications. Moreover, even such an approach still follows the classical concept of a closed-loop interferometer established in the 1980s, by using proportional-integral-derivative (PID) controllers.

In this scenario, one can observe that only few authors exploit the full potential of advanced control theory to solve the interferometry problem, which makes clear that this issue is a very promising field of investigation. Examples of works that use such modern theories include some versions of closed-loop optical voltage sensors (OVS) based on Pockels effect, a kind of polarimetric interferometer whose input-output characteristic curve follows equation (1). Based on the Lyapunov or Lyapunov–Krasovskii functions, control schemes have been designed as robust as possible to solve this problem by LI *et al*. (2015) and LI *et al*. (2014). A control algorithm was developed to guarantee closed-loop OVS mean-square exponential stability with a prescribed H_∞ performance level. Robust control law and Linear Matrix Inequalities (LMIs) were also applied in (HUI *et al*., 2013) to implement a tracking system for the gain drift of the phase modulator based on four-state modulation, which provides a significant improvement in the performance of an optical voltage sensor, and in (DENG *et al*., 2017) for analysing the influence of optical parameters on the performance of closed-loop

OVSs based on Pockels effect, aiming the proposal of a control algorithm that suppresses the nonlinearity caused by the non-ideal parameters of optical devices for optimizing the detection precision of sensor. However, in the context of LMI applied to these systems, the projects still take into account the linearized system. Since the interferometer is a nonlinear system, the linearization can limit the operating range around small deviations from the operation point, and in cases of large disturbances the closed-loop system may reach instability, not ensuring the necessary robustness, accuracy and inserting the need for reset circuits.

The control strategies generally used in closed-loop homodyne interferometers are concerned with the compensation of the spurious low frequency disturbances (ϕ_0). Some authors, however, have used control systems to compensate both the spurious signals and also the signal of interest $\Delta\phi$, by the so called "feedback interferometry", as mentioned before (EOM *et al*., 2001; FRITSCH; ADAMOWSKY, 1981; FISHER; WARDE, 1979). This approach allows obtaining a proportional relationship between the signal of interest and the control signal used to drive the actuator of the system. In this way, the accuracy of the interferometric systems can be combined with an expansion of the measuring range and real-time operation of the system.

The work described by (FISHER; WARDE, 1979) used a single-pole low pass-filter to control a bulk homodyne Mach-Zehnder interferometer, where, by the adjustment of the cutoff frequency and the gain of the filter, the author was capable to compensate $\Delta\phi$ within the limits of 3.5π rad of phase amplitude for low frequencies and amplitudes up to $\frac{\pi}{2}$ rad for 150 Hz of bandwidth. In 1981, Klaus Fritsch and Gregory Adamowsky (FRITSCH; ADAMOWSKY, 1981) proposed an electronic control circuit for a single mode optical fiber Mach-Zehnder interferometer. The control system comprised two cascaded integrators and allowed the detection of phase shifts of the order of 500 μrad rms for frequencies above 500 hertz. After its warmup, the system usually reseted once a minute.

In 2001, (EOM *et al*., 2001) proposed a dynamic compensation of nonlinearity in a homodyne laser interferometer, where a computer collected two phase-quadrature signals, and calculated the DC offsets, the AC amplitudes and the difference from the phase-quadrature by the elliptical fitting with a least-squares method. The authors, however, reached 0.2 Hz for the update rate of the control voltages and concluded that the system cannot be used in real-time applications.

More recently, in the work (XIE *et al*., 2017), the quadrature technique together with a novel iterative algorithm with a digital lock-in phase demodulator was proposed in order to compensate the nonlinear error of a heterodyne interferometer caused by phase demodulating electronics. The algorithm used the quadrature signals, iterative translating and scaling transforms, to correct the phase diagram of the two output signals of the phase demodulator from an ellipse to a circle at the origin. The experimental setup used polarized light in order to obtain the quadrature signals.

Up to the moment, the group at LOE (Laboratory of Optoelectronic - UNESP – Ilha Solteira) has achieved good results in implementing the nonlinear control system based on variable structure in bulk Michelson interferometers and in all-fiber Mach-Zehnder interferometers. This control technique showed robustness, low cost and easy implementation (MARTIN *et al*., 2017a; MARTIN *et al*., 2017b; LYRA *et al*., 2019).

Within this scope, the present work concerns with the application of a novel sliding mode control using the high-gain approach (as designated by Udd and Spillman, 2011) to fully compensate the phase shift of ϕ_0 and $\Delta\phi$ in a Michelson bulk interferometer. The interferometer was modified, as proposed by (LEMES, 2014), in order to generate phase quadrature signals, exploring the spatial phase shift between consecutive interference fringes, therefore without the need of complex polarizing optics. As it will be further discussed in this text, the proposed technique has potential to increase the frequency bandwidth and phase dynamic range of operation when compared to similar systems based on high gain approach described in literature.

Also an innovative concept of demodulation method for quadrature interferometers is presented, having the main advantages of estimating the phase shifts in real-time, without applying phase unwrapping algorithms and without driving a feedback PZT in the reference arm of the interferometer. This proposed method uses the output signals of the open-loop quadrature interferometer and performs a calculation with a dynamic system digitally implemented, in such a way that the overall system becomes equivalent to the closed-loop quadrature interferometer using the high gain approach. In other words, it is an equivalent system, but virtually controlled.

In Chapter 2, a brief theoretical background of two beam interferometers is presented, covering the experiment of Young, which serves as basis for the subsequent deductions of

Michelson bulk interferometer and the modified Michelson interferometer, in order to generate the output signals in quadrature.

The sliding mode control theory is briefly explained in Chapter 3, as well as the modeling of the interferometric system in state space variables and the choice of the sliding surface. Yet in this chapter, the stability analysis, closed-loop simulations and theoretical phase plan are presented. At the end of the chapter we also explained the new concept of demodulation method for quadrature interferometers using the equivalent system virtually controlled.

In Chapter 4, it is described the implementation of the control and logging data system in the chosen embedded plataform, the main difficulties and associated practical issues. The description of the experimental setup and procedures adopted to evaluate the control system are presented. And also, the implemented equivalent system virtually controlled with the ellipse fitting algorithm, in order to guarantee the phase shift estimation, even with mismatches in the quadrature condition between the two interferometers outputs, is discussed.

Finally, in Chapter 5 the main conclusions and proposals for future works are presented.

2 Two-beam optical interferometry

Light can be though as an electromagnetic transversal wave propagating in space (HARIHARAN, 2007), and therefore, it is subjected to the wave interference phenomenon when two or more light beams are superimposed, resulting in constructive or destructive interference. Interferometers are devices based in such phenomenon, generally having two different optical paths, one isolated and another under the influence of the physical quantity to be measured, called respectively reference arm and sensor arm. Both light beams are them combined at a determined spot, where the optical intensity or irradiance is a function of the relative phase between the two beams.

Extremely small deviations in the optical path produce significant changes in the optical intensity due to the order of magnitude of the light wavelength. In this work it was used a HeNe laser (Helium Neon), which operates at 632.8 nm wavelength.

In order to explain the deductions of the optical intensity for the different interferometers, some theory background mainly based in (HECHT, 2002) and (HARIHARAN, 2007) is presented in this section.

The propagation of the light can be studied through its electrical field component (HECHT, 2002). The vector representing the electrical field of a monochromatic light beam propagating in free space can be described as:

$$\vec{e}_{(\vec{r},t)} = \vec{E}_0 cos\left(\omega t - \vec{k}.\vec{r} + \xi\right), \tag{2}$$

where $\vec{E}_0$ express the amplitude and direction of the electrical field oscillation, ω is the frequency in radians per second of the source of light, $\vec{r}$ is the actual position of the wave front being analyzed, $\vec{k}$ is the wave vector, which express the direction of the wave propagation and is related with the wavelength λ and the refractive index of the propagation medium n $\left(|\vec{k}| = \frac{2\pi n}{\lambda}\right)$, and ξ is the initial phase.

One can see that the electrical field also can be expressed by (3):

$$\vec{e}_{(\vec{r},t)} = Re\left\{\vec{E}_0 e^{j\left(\omega t - \vec{k}.\vec{r} + \xi\right)}\right\} = Re\left\{\vec{E} e^{j\omega t}\right\}. \tag{3}$$

A common practice that leads to simplification on mathematical operations and manipulations is to use the complex vector $\vec{E}_{(\vec{r},t)}$ associated with the electrical field, described in (4):

$$\vec{E}_{(\vec{r},t)} = \vec{E}_0 e^{j(-\vec{k}.\vec{r}+\xi)}. \tag{4}$$

The energy that crosses an unit area, normal to the propagation direction of the beam, in unit time, is related with the instantaneous Poynting vector $\vec{s}$:

$$\vec{s} = \vec{e} \times \vec{h}\,, \tag{5}$$

where $\vec{h}$ is the magnetic field vector, which can be expressed by (6):

$$\begin{cases} \vec{h} = Re\left\{\vec{H}_0 e^{j(\omega t-\vec{k}.\vec{r}+\xi)}\right\} = Re\left\{\vec{H} e^{j\omega t}\right\} \\ \vec{H}_{(\vec{r}\,,t)} = \vec{H}_0 e^{j(-\vec{k}.\vec{r}+\xi)} \end{cases}. \tag{6}$$

The optical intensity is proportional to the time average of the Poynting vector, therefore, it can be expressed as:

$$I \propto \frac{1}{T}\int_0^T \vec{e} \times \vec{h}\, dt = \frac{1}{T}\int_0^T Re\left\{\vec{E} e^{j\omega t}\right\} \times Re\left\{\vec{H} e^{j\omega t}\right\} dt$$

$$= \frac{1}{T}\int_0^T Re\left\{\vec{E} e^{j\omega t}\right\} \times \frac{\left(\vec{H} e^{j\omega t} + \vec{H}^* e^{-j\omega t}\right)}{2}\, dt = \frac{1}{2T}\int_0^T Re\left\{\vec{E} \times \vec{H} e^{j2\omega t} + \vec{E} \times \vec{H}^*\right\} dt\,,$$

where T is the period of the monochromatic signal.

The term $\vec{E} \times \vec{H}^*$ does not depend on time, and the average $\frac{1}{2T}\int_0^T Re\left\{\vec{E} \times \vec{H} e^{j2\omega t}\right\} dt$ is equal to zero, therefore:

$$I \propto \frac{1}{2} Re\left\{\vec{E} \times \vec{H}^*\right\}. \tag{7}$$

Considering now a propagation medium without ohmic losses, the complex vector $\vec{H}$ is related to $\vec{E}$ through the relationship (8) (BORN; WOLF, 1986):

$$\vec{H} = \frac{\vec{E}}{z_0}\,, \tag{8}$$

where z_0 corresponds to the intrinsic impedance of the medium.

Considering the laser beam propagating in the free space, $z_0 = 120\pi\ \Omega$. In this thesis the optical intensity I will be considered as the time average of the Poynting vector, normalized by $\frac{1}{2z_0}$:

$$I = \left(\frac{1}{\frac{1}{2z_0}}\right)\frac{1}{2z_0}\ Re\{\vec{E} \times \vec{E}^*\} = \left|\vec{E}\right|^2 = \vec{E} \cdot \vec{E}^* \tag{9}$$

The relationship expressed in (9) will be used in next subsections in order to obtain the characteristic curve of the interferometers.

2.1 Experiment of Young

Thomas Young (1773 – 1829) was a British mathematician and physicist known to be the first scientist to explain the light diffraction on the basis of the wave theory of light (RUBINOWICZ, 1957). The experiment of Young (illustrated in Figure 3) demonstrated for the first time the principle of optical interference, becoming the basis for posterior interferometers (SALEH; TEICH, 2007).

Figure 3 - Young double slit experiment.

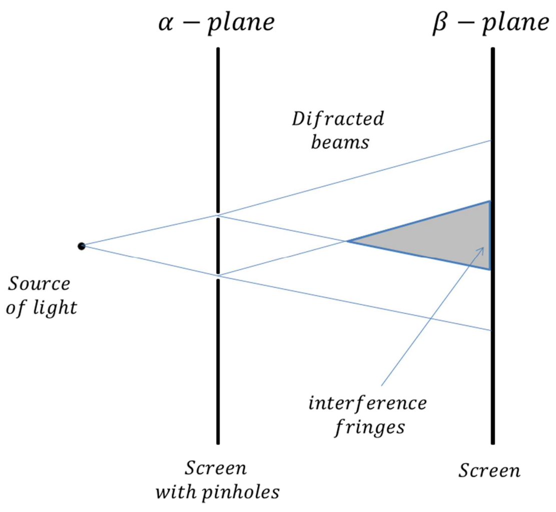

Source: (Modified from HARIHARAN, 2007)

In this experiment, an opaque screen with two pinholes located in the α-plane separates the source of light from the β-plane located at a D distance from the screen, where the interference fringes are formed. The pinholes then can be regarded as secondary sources that overlap their diffracted beams in the shadowed region of β-plane (HARIHARAN, 2007).

In Figure 4 it is shown a closer look at the experiment of Young, which facilitates some considerations and mathematical approximations to obtain the characteristic curve of the interference fringes optical intensity. In the figure, it is assumed that plane β is at a sufficiently large distance D from the pinholes such that the wave can be considered approximately a plane wave.

Figure 4- Illustration of the experiment of Young.

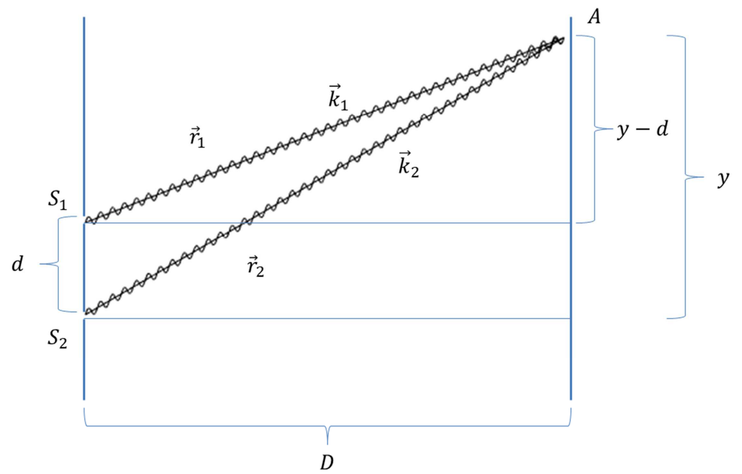

Source: (modified from Hecht, 2002)

The expression of the complex vector associated with the electrical field of the light beams that passed by pinhole 1 and pinhole 2 and reach the plane β are respectively given by:

$$\begin{cases} \vec{E}_1 = \vec{E}_{01} e^{j(\omega t - \vec{k}_1 \cdot \vec{r}_1 + \xi_1)} \\ \vec{E}_2 = \vec{E}_{02} e^{j(\omega t - \vec{k}_2 \cdot \vec{r}_2 + \xi_2)} \end{cases} \quad (10)$$

Assuming now that the distance d between the two pinholes is in the order of micrometers, and, therefore, much smaller than the distance D between the planes α and β, the scalar products between the wave vectors and the coordinates of the wave front can be considered to be in parallel directions, and therefore:

$$\begin{cases} \vec{k}_1 \cdot \vec{r}_1 = k_1 r_1 \\ \vec{k}_2 \cdot \vec{r}_2 = k_2 r_2 \end{cases} . \quad (11)$$

It is known that for the two wavefronts propagating in mediums with the same refractive index, the wavelength will be the same, and also the absolute value of the wave vectors, resulting in:

$$k_1 = \frac{2\pi n}{\lambda} = k_2 = k \, . \quad (12)$$

The electrical field of the overlapped region can be expressed as:

$$\vec{E}_t = \vec{E}_1 + \vec{E}_2 = \vec{E}_{01} e^{j(\omega t - k\, r_1 + \xi_1)} + \vec{E}_{02} e^{j(\omega t - k\, r_2 + \xi_2)} \ , \tag{13}$$

and considering $\vec{E}_{01}$ and $\vec{E}_{02}$ as real vectors, the associated optical intensity is given by:

$$I_t = \left|\vec{E}_t\right|^2 = \left(\vec{E}_1 + \vec{E}_2\right) \cdot \left(\vec{E}_1 + \vec{E}_2\right)^* = \left|\vec{E}_1\right|^2 + \left|\vec{E}_2\right|^2 + \vec{E}_1 . \vec{E}_2^* + \vec{E}_1^* . \vec{E}_2 \Rightarrow$$

$$= \left|\vec{E}_{01}\right|^2 + \left|\vec{E}_{02}\right|^2 + \vec{E}_{01} . \vec{E}_{02}\left[e^{j(k\, r_2 - k\, r_1 + \xi_1 - \xi_2)} + e^{-j(k\, r_2 - k\, r_1 + \xi_1 - \xi_2)}\right] \Rightarrow$$

$$= \left|\vec{E}_{01}\right|^2 + \left|\vec{E}_{02}\right|^2 + 2\vec{E}_{01} . \vec{E}_{02} \cos(k\, r_2 - k\, r_1 + \xi_1 - \xi_2) \, . \tag{14}$$

From Figure 3 one can observe the following relationships:

$$r_1^2 = (y-d)^2 + D^2 \ \Rightarrow r_1 = D\sqrt{1 + \frac{(y-d)^2}{D^2}} \ , \tag{15}$$

and

$$r_2^2 = y^2 + D^2 \ \Rightarrow r_2 = D\sqrt{1 + \frac{y^2}{D^2}} \ . \tag{16}$$

By using Taylor series for $y \ll D$ and $(y-d) \ll D$ in (15) and (16), r_1 and r_2 are approximated by:

$$r_1 \cong D + \frac{(y-d)^2}{2D} \ , \tag{17}$$

and

$$r_2 \cong D + \frac{y^2}{2D} \ . \tag{18}$$

Substituting (17) and (18) in (14), leads to:

$$I_t = I_0\left[1 + V\cos\left(\frac{kd}{D}y - \frac{kd^2}{2D} + \xi_1 - \xi_2\right)\right], \tag{19}$$

where I_0 is the of the optical intensity of the secondary sources, and V is called fringe visibility, a parameter that assumes values between 0 and 1, depending on the parallelism between the vectors $\vec{E}_{01}$ and $\vec{E}_{02}$ and their module similarity (HARIHARAN, 2003; BORN; WOLF, 1986). Those parameters are defined as:

$$I_0 = \left|\vec{E}_{01}\right|^2 + \left|\vec{E}_{02}\right|^2 \quad , \tag{20}$$

and

$$V = \frac{2\vec{E}_{01}.\vec{E}_{02}}{\left|\vec{E}_{01}\right|^2 + \left|\vec{E}_{02}\right|^2} \quad . \tag{21}$$

2.2 Michelson Interferometer

In the 19th century most physicists believed that electromagnetic waves needed a medium to propagate, such as sound travels in air or surface waves in water. This theoretical medium was called “luminiferous aether” and also it was foreseen that with the orbital movement of earth around the sun, the flux of aether in earth surface would originate an “aethereal wind”, which could be detected through the measurement of the relative velocity between aether and earth (AMERICAN PHYSICAL SOCIETY, 2005; HARIHARAN, 2007; BORN; WOLF, 1986). Therefore, Albert Abraham Michelson (1852 – 1931) in partnership with Edward Morley (1838 – 1923) developed an extremely high accuracy experiment, shown in Figure 5, to carry out such measurement and their results showed that aether did not exist. Nowadays the apparatus is known as Michelson interferometer.

Figure 5 - Michelson interferometer.

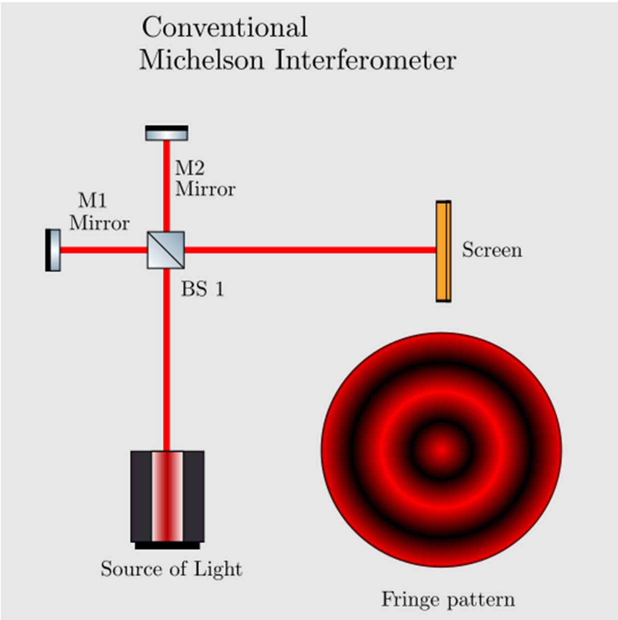

Source: (Modified from Leão, 2004)

The proposed interferometer uses a single source of light that emits a light beam that is divided by a beam splitter, and then each beam propagates in a different optical path, called interferometer arms. At the end of each arm, a mirror is positioned, that reflects the light back to the beam splitter and the two beams are recombined, thereby forming the patterns of constructive and destructive interference on a screen. A percentage of the light beams that reflect back to the beam splitter propagate back to the laser cavity direction and is lost.

The two beams emerging from the beam splitter and going in the direction of the screen can be though as the experiment of Young, and therefore can be described by equation (19). Considering now the expression of the optical intensity at the photodetector positioned at a constant point $y = d/2$ on the screen, the optical intensity becomes:

$$I_p = \frac{I_0}{2}\big(1 + Vcos(\xi_1 - \xi_2)\big)\,. \tag{22}$$

It is noteworthy that the optical intensity of the laser I_0 is divided by two in the expression of I_p , due to the percentage of the recombined beams that returns to the laser cavity (considering the division rate of the beam splitter 50:50).

The term $(\xi_1 - \xi_2)$ is a relative difference of phase, arising from the mismatch between the optical paths traveled by the two beams. Considering that the lengths of the arms 1 and 2 of the interferometer, are respectively $L_1 = L$, $L_2 = L + \Delta L$, and also that the interferometer is in the free space (n=1), the optical paths traversed by the light beams can be written as (BORN; WOLF, 1986):

$$\xi_1 = \frac{2\pi}{\lambda}2L_1 = \frac{2\pi}{\lambda}2L\,, \tag{23}$$

and

$$\xi_2 = \frac{2\pi}{\lambda}2L_2 = \frac{2\pi}{\lambda}2(L + \Delta L), \tag{24}$$

regarding that the total distance traveled by the light beams is two times the length of the interferometers arms. Then, the relative phase difference results in:

$$\Psi = \xi_1 - \xi_2 = \frac{2\pi}{\lambda}2(\Delta L), \tag{25}$$

or

$$\Psi = \frac{4\pi}{\lambda}\Delta L \; = \phi_0\,. \tag{26}$$

If the displacement ΔL has a time varying component, Ψ can be rewritten as:

$$\Psi = \Delta\phi_{(t)} + \phi_0. \tag{27}$$

Substituting (27) in (22) leads to:

$$I_{t(t)} = \frac{I_0}{2}\{1 + Vcos[\Delta\phi_{(t)} + \phi_0]\}. \tag{28}$$

As one can see, (28) and (1) are the same expression, Q.E.D.

In this work the modeling, development and application of a novel control strategy based on sliding mode control is proposed, for two-beam quadrature interferometers, with the high-gain approach (UDD; SPILLMAN, 2011; GIALLORENZI *et al*., 1982). This approach consists of controlling the interferometer in such a way that the phase correction signal compensates the total phase shift $\Delta\phi + \phi_0$ at the input of the interferometer. In this case, by reading the control signal, the demodulation process does not require phase unwrapping algorithms, i.e., the phase correction signal presents a straight-line relationship with the interferometer phase shift $\Delta\phi + \phi_0$.

This control law requires the measurement of the output signals with a phase difference of $\frac{\pi}{2}$ rad. A modified Michelson interferometer was used to obtain the signals in phase quadrature, this modification is explained in the following Section 2.3.

2.3 Modified Michelson interferometer

Generally several changes in the polarization of the laser beam in the interferometer arms are necessary, in order to obtain the output signals in phase quadrature. This is achieved by adding different optical devices, increasing the complexity of the quadrature interferometers, when compared to the homodyne conventional ones.

As described by (LEMES, 2014) it is possible to assemble a quadrature interferometer configuration without the use of polarized optical devices. First, refer to equation (19), which expresses the optical intensity, in the β – plane of the experiment of Young (see Figure 3). One can see that the argument of the cosine function varies with changes in the position y; therefore, two photodetectors in different positions of the fringe pattern will generate signals with a relative phase difference.

The configuration proposed by (LEMES, 2014) is presented in Figure 6. It consists of a conventional Michelson interferometer, with an additional beam splitter BS2 at the output, and two photodetectors, positioned perpendicular to the beams that emerge from BS2. In each of the two outputs of the beam splitter BS2 a circular fringe pattern will form. Placing the two photodetectors at different positions of their respective fringe pattern will generate signals with a relative phase difference, which can be adjusted to obtain the value of $\pi/2$ rad and, consequently, the output signals in quadrature.

Figure 6 - Modified Michelson interferometer.

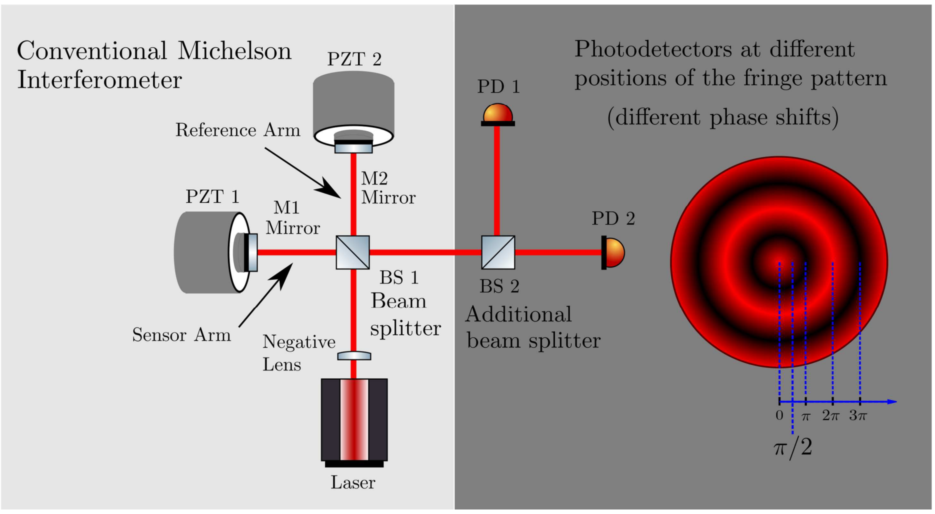

Source: (LEMES, 2014).

The optical intensity at each photodetector is given by (considering BS2 rated as 50:50):

$$I_1 = \frac{I_0}{4}\left[1 + V_1 \cos\left(\frac{kd}{D}y_1 - \frac{kd^2}{2D} + \xi_1 - \xi_2\right)\right] \quad , \tag{29}$$

and

$$I_2 = \frac{I_0}{4}\left[1 + V_2 \cos\left(\frac{kd}{D}y_2 - \frac{kd^2}{2D} + \xi_1 - \xi_2\right)\right] \quad , \tag{30}$$

where y_1 and y_2 are adjusted according to:

$$(y_2 - y_1)\frac{kd}{D} = \frac{\pi}{2} \quad , \tag{31}$$

or

$$y_2 = \left(\frac{D}{kd}\frac{\pi}{2}\right) + y_1 \quad . \tag{32}$$

Substituting (32) in (30) leads to:

$$I_2 = \frac{I_0}{4}\left[1 + V_2 \cos\left(\frac{kd}{D} y_1 + \frac{\pi}{2} - \frac{kd^2}{2D} + \xi_1 - \xi_2\right)\right] \quad , \tag{33}$$

or

$$I_2 = \frac{I_0}{4}\left[1 - V_2 \sin\left(\frac{kd}{D} y_1 - \frac{kd^2}{2D} + \xi_1 - \xi_2\right)\right] \quad . \tag{34}$$

By considering $y_1 = d/2$, grouping the constant terms and simplifying the notation with (25) and (27), equations (29) and (34) are rewritten as:

$$I_1 = \frac{I_0}{4}[1 + V_1 \cos(\Delta\phi + \phi_0)] \quad , \tag{35}$$

and

$$I_2 = \frac{I_0}{4}[1 - V_2 \sin(\Delta\phi + \phi_0)] \quad . \tag{36}$$

The output signal of a quadratic law photodetector, allied with a transimpedance circuit, is proportional to the incident optical intensity. Therefore, the voltage signals $v_{1(t)}$ and $v_{2(t)}$ respectively from the photodetectors PD_1 and PD_2 are expressed by:

$$v_{1(t)} = A_1[1 + V_1 \cos(\Delta\phi + \phi_0)] \quad , \tag{37}$$

and

$$v_{2(t)} = A_2[1 - V_2 \sin(\Delta\phi + \phi_0)] \quad , \tag{38}$$

where the parameters A_1 and A_2 are proportionality constants (measured in volts) that take into account the responsivity of the photodetectors and the gain of the transimpedance circuit, and $V_1$and V_2 , as explained before, are the fringe visibilities.

2.4 Quadrature Correction

The properly work of the proposed control system, as will be further discussed, rely on the feedback signals without the offset (A_1 and A_2 in (37) and (38)) and with the interferometric phase difference of $\frac{\pi}{2}$ radians. These conditions require fine adjustments, and even then, the DC levels or the phase difference between the quadrature signals may slowly vary in time.

Several authors have proposed ways to estimate and correct the errors induced by the quadrature condition mismatches, where it is highlighted a great number of works using methods based on least squares ellipse fitting, such as Heydemann (1981), Birch (1990), Wu, Su and Peng (1996), Eom, Kim and Jeong (2001), Gregorcic, Pozar and Mozina (2009), Pozar and Mozina (2011), among others. Recent approaches are focusing on neural networks and deep learning algorithms to identify and compensate the quadrature errors in resolver based angular position sensors, which also provide the output signals in quadrature conditions; as an example, one can cite Gao *et al*. (2018) and Dhar *et al*. (2010).

The algorithm adopted in this work was implemented for on-line correction of the quadrature signals, therefore the classical methodology presented in (HEYDEMANN, 1981) was chosen, due to the simplicity of implementation and because it does not require heavy processing. The mathematical deduction and algebraic manipulation in order to apply the least squares method to (37) and (38), as proposed by Heydemann (1981), are shown as in the following.

Let us firstly define the desired ideal quadrature signals as $v_{1,id}$, $v_{2,id}$ and the measured signals $v_{1,m}$ and $v_{2,m}$ as expressed in the following equations:

$$v_{1,id}(t) = A_1 V_1 \cos(\Psi)\ , \tag{39}$$

and

$$v_{2,id}(t) = A_1 V_1 \sin(\Psi)\ , \tag{40}$$

and

$$v_{1,m}(t) = A_1 V_1\, cos(\Psi) + A_1\ , \tag{41}$$

and

$$v_{2,m}(t) = A_2 V_2 \sin(\Psi - \alpha) + A_2\ , \tag{42}$$

where the parameter α represents a phase deviation from the quadrature condition. It can be seen that the Lissajous figure formed by v_1^{id} and v_2^{id} is a circle with radius $R = A_1V_1$, while the measured signals v_1^m and v_2^m form an ellipse. Rewriting v_1^{id} and v_2^{id} as function of the measured signals (v_1^m, v_2^m) and substituting the parameter $r = \frac{A_1V_1}{A_2V_2}$, leads to:

$$v_{1,id}(t) = v_{1,m}(t) - A_1\ , \tag{43}$$

$$v_{2,id}(t) = \frac{1}{\cos(\alpha)}\left[r\left(v_{2,m}(t) - A_2\right) + sin(\alpha)(v_{1,m}(t) - A_1)\right]. \tag{44}$$

In this way, it is possible to correct the signals with lack of quadrature, as long as A_1, A_2, r and α are known.

Therefore, in order to estimate such parameters, equations (43) and (44) are substituted in the parametric equation of the ellipse, where the resulting relationship is manipulated into a form suitable to be applied to the least squares method, such as shown below:

$$\left(v_{1,m} - A_1\right)^2 + \left\{\frac{1}{\cos(\alpha)}\left[r\left(v_{2,m} - A_2\right) + \sin(\alpha)\left(v_{1,m} - A_1\right)\right]\right\}^2 = (A_1V_1)^2. \tag{45}$$

From (45) it is obtained:

$$\begin{gathered} {v_{1,m}}^2 - 2A_1v_{1,m} + A_1^2 + \frac{1}{\cos^2(\alpha)}[r^2\left({v_{2,m}}^2 - 2v_{2,m}A_2 + A_2^2\right) + \\ \sin^2(\alpha)\left({v_{1,m}}^2 - 2v_{1,m}A_1 + A_1^2\right) + 2r\left(v_{2,m} - A_2\right)\left(v_{1,m} - A_1\right)\sin(\alpha)] = (A_1V_1)^2\ , \end{gathered} \tag{46}$$

or

$$\begin{aligned} {v_{1,m}}^2[1 + \tan^2(\alpha)] + {v_{2,m}}^2\left[\frac{r^2}{\cos^2(\alpha)}\right] + v_{1,m}\left[-2A_1 - 2A_1\tan^2(\alpha) - \frac{2r\sin(\alpha)}{\cos^2(\alpha)}A_2\right] \\ + v_{2,m}\left[\frac{-2r^2A_2}{\cos^2(\alpha)} - \frac{2rA_1\sin(\alpha)}{\cos^2(\alpha)}\right] + v_{1,m}v_{2,m}\left[\frac{2r\sin(\alpha)}{\cos^2(\alpha)}\right] \\ + A_1^2[1 + \tan^2(\alpha)] + \frac{r^2A_2^2}{\cos^2(\alpha)} + \frac{2r\sin(\alpha)}{\cos^2(\alpha)}A_1A_2 = (A_1V_1)^2\ , \end{aligned} \tag{47}$$

or else

$$v_{1,m}{}^2\left[\frac{1}{\cos^2(\alpha)}\right]+v_{2,m}{}^2\left[\frac{r^2}{\cos^2(\alpha)}\right]+v_{1,m}\left[\frac{-2A_1-2rA_2\sin(\alpha)}{\cos^2(\alpha)}\right]$$
$$+v_{2,m}\left[\frac{-2r^2A_2-2rA_1\sin(\alpha)}{\cos^2(\alpha)}\right]+v_{1,m}v_{2,m}\left[\frac{2r\sin(\alpha)}{\cos^2(\alpha)}\right]+\frac{A_1^2}{\cos^2(\alpha)} \quad (48)$$
$$+\frac{r^2A_2^2}{\cos^2(\alpha)}+\frac{2r\sin(\alpha)}{\cos^2(\alpha)}A_1A_2=(A_1V_1)^2\,.$$

Multiplying both sides of the expression by $\cos^2(\alpha)$, equation (48) can be rewrited as:

$$Av_{1,m}{}^2+Bv_{2,m}{}^2+Cv_{1,m}v_{2,m}+Dv_{1,m}+Ev_{2,m}=1\ , \quad (49)$$

where:

$$\begin{cases} A=[(A_1V_1)^2\cos^2(\alpha)-A_1^2-r^2A_2^2-2rA_1A_2\sin(\alpha)]^{-1} \\ B=r^2A \\ C=2rA\sin(\alpha) \\ D=-2A[A_1+rA_2\sin(\alpha)] \\ E=-2Ar[rA_2+A_1\sin(\alpha)] \end{cases}. \quad (50)$$

The coefficients A, B, C, D and E are obtained from the fitting operation using the least squares method on the experimental data. Therefore, considering $v_{1,m}$ and $v_{2,m}$ as sampled data from the output signals of the interferometer, containing p samples, disposed in $p\times 1$ column vectors, equation (49) can be disposed in matrix format such as:

$$\boldsymbol{X}.\boldsymbol{Q}+\boldsymbol{\varepsilon}=\boldsymbol{Y}\ , \quad (51)$$

where $\boldsymbol{X}\in\mathbb{R}^{px5}$, $\boldsymbol{Q}\in\mathbb{R}^{5x1}$, $\boldsymbol{\varepsilon}\in\mathbb{R}^{px1}$ and $\boldsymbol{Y}\in\mathbb{R}^{px1}$ are expressed by:

$$\boldsymbol{X}=\begin{bmatrix} v_{1,m_1}{}^2 & v_{2,m_1}{}^2 & v_{1,m_1}v_{2,m_1} & v_{1,m_1} & v_{2,m_1} \\ v_{1,m_2}{}^2 & v_{2,m_2}{}^2 & v_{1,m_2}v_{2,m_2} & v_{1,m_2} & v_{2,m_2} \\ \vdots & \vdots & \vdots & \vdots & \vdots \\ v_{1,m_p}{}^2 & v_{2,m_p}{}^2 & v_{1,m_p}v_{2,m_p} & v_{1,m_p} & v_{2,m_p} \end{bmatrix},\quad \boldsymbol{Q}=\begin{bmatrix} A \\ B \\ C \\ D \\ E \end{bmatrix},\quad Y=\begin{bmatrix} 1 \\ 1 \\ \vdots \\ 1 \end{bmatrix}_{px1},\quad \boldsymbol{\varepsilon} \quad (52)$$

It is important to highlight that in the presented notation $v_{i,m\ j}$ represents the measured j-th sample of the i-th output signal, and ε_j represents the j-th error between the experimental data and the fitted curve.

The objective then is to find the matrix $\boldsymbol{Q}$ of the coefficients that minimizes the sum of the squares of the difference between the sampled experimental data and the fitting curve (JOHNSON; FAUNT, 1992). This sum can be expressed in the following terms:

$$S = \sum_{i=1}^{p} \varepsilon_i^2 \ . \tag{53}$$

Isolating the error vector in equation (51), the sum S can be rewritten as:

$$S = \boldsymbol{\varepsilon}^t \boldsymbol{\varepsilon} \ , \tag{54}$$

or

$$S = (\boldsymbol{Y} - \boldsymbol{XQ})^t (\boldsymbol{Y} - \boldsymbol{XQ}) \ , \tag{55}$$

or else

$$S = \boldsymbol{Y}^t\boldsymbol{Y} - \boldsymbol{Y}^t\boldsymbol{XQ} - \boldsymbol{Q}^t\boldsymbol{X}^t\boldsymbol{Y} + \boldsymbol{Q}^t\boldsymbol{X}^t\boldsymbol{XQ} \ . \tag{56}$$

The minimum error is achieved when the gradient of S is equal to zero. Deriving S in relation to the matrix $\boldsymbol{Q}$ and equaling it to zero results in:

$$\frac{\partial \mathrm{S}}{\partial \boldsymbol{Q}} = -\boldsymbol{Y}^t\boldsymbol{X} - \boldsymbol{Y}^t\boldsymbol{X} + \boldsymbol{2Q}^t\boldsymbol{X}^t\boldsymbol{X} = 0 \ , \tag{57}$$

or

$$\frac{\partial \mathrm{S}}{\partial \boldsymbol{Q}} = 2(-\boldsymbol{Y}^t\boldsymbol{X} + \boldsymbol{Q}^t\boldsymbol{X}^t\boldsymbol{X}) = 0 \ , \tag{58}$$

or else

$$\frac{\partial \mathrm{S}}{\partial \boldsymbol{Q}} = 2(-\boldsymbol{X}^t\boldsymbol{Y} + \boldsymbol{X}^t\boldsymbol{XQ})^t = 0 \Longrightarrow \boldsymbol{X}^t\boldsymbol{XQ} = \boldsymbol{X}^t\boldsymbol{Y} \ . \tag{59}$$

Therefore, the resulting coefficients can be calculated by equation (60):

$$\boldsymbol{Q} = (\boldsymbol{X}^t\boldsymbol{X})^{-1}\boldsymbol{X}^t\boldsymbol{Y} \ , \tag{60}$$

and the ellipse parameters are obtained using the following relationships:

$$r = \sqrt{\frac{B}{A}} \ , \quad \alpha = \arcsin\left(\frac{C}{2rA}\right) \ , \quad A_1 = \frac{2BD - EC}{C^2 - 4AB} \ , \quad A_2 = \frac{2AE - CD}{C^2 - 4AB} \ . \tag{61}$$

Using this method, a Matlab routine was designed to simulate the non-ideal interferometric measured signals, $v_{1,m}$ and $v_{2,m}$, and perform the correction algorithm. In Figure 7 both signals are presented, as function of time, with an Additive white Gaussian noise (AWGN) to the deterministic signal. In Figure 8 are shown the Lissajous figure formed by the simulated signals together with the ellipse curve, fitted by the method proposed by Heydemann (1981). By the last, in Figure 9 the Lissajous figure formed by the corrected quadrature signals is shown. The elaborated simulation routine is presented in Appendix at the end of this work.

Figure 7 - Simulated measured interferometric signals.

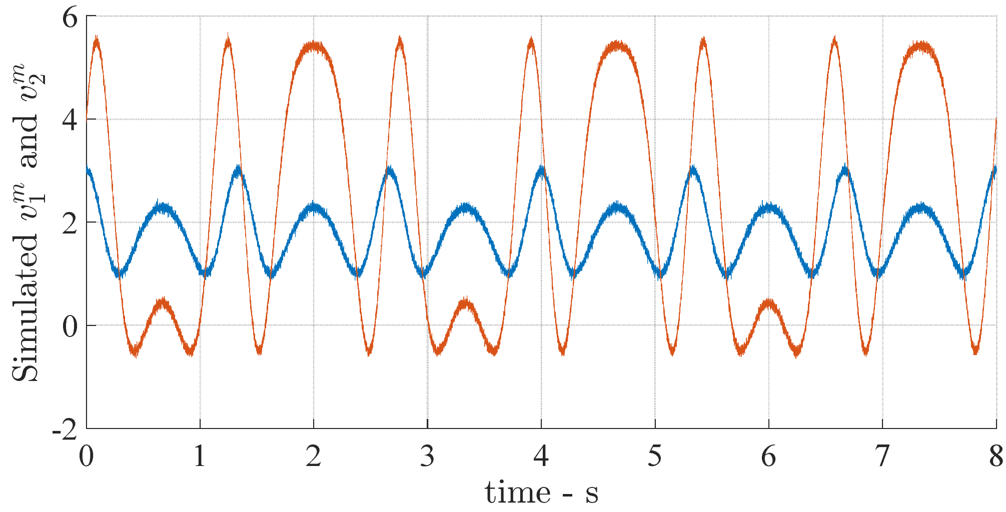

Source: elaborated by the author.

Figure 8 - $v_{1,m}$, $v_{2,m}$ Lissajous figure and fitted ellipse.

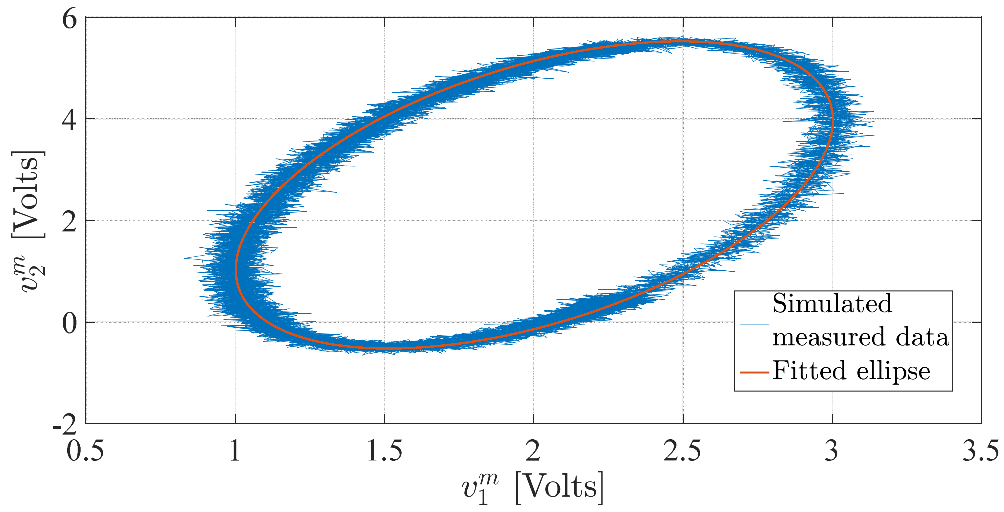

Source: elaborated by the author.

Figure 9 – Lissajous figure of the quadrature corrected signals $v_{1,id}$, $v_{2,id}$.

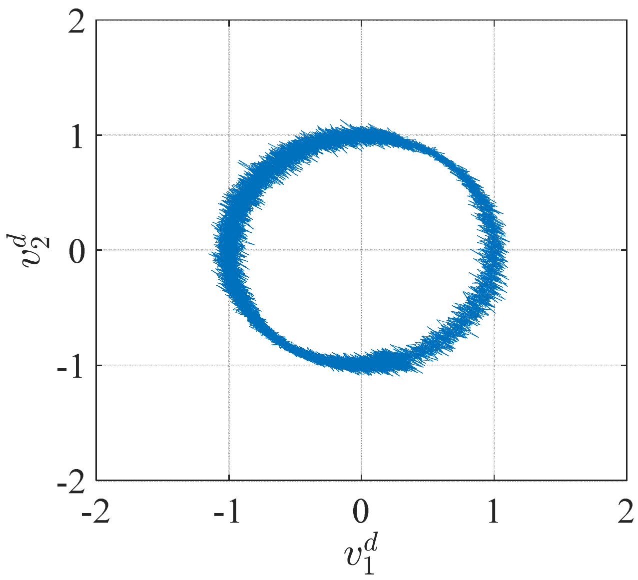

Source: elaborated by the author.

3 Sliding Mode control

This chapter gives a brief theoretical background about the sliding mode control technique and the modeling of the interferometric system, where the stability analysis of the closed-loop system is carried out using an analytical method and by a graphical approach. Closed-loop simulations, showing the behavior of the system around the different groups of equilibrium points are presented, where the chattering phenomenon is observed and discussed. Also at the end of this chapter it is presented a new concept of phase demodulation technique, based on the same proposed control law but designed as a virtually implemented equivalent closed-loop system.

Dynamic systems driven by a control law that is a discontinuous function of the state variables can originate the so-called sliding mode. This operating regime is characterized by a fast switching control action, which forces the system trajectory to certain regions of the state space, where the system will present the desired behavior. These regions are referred to as sliding surfaces (UTKIN, 1982). The main advantages of such control strategy are: the robustness with respect to parameters variation, disturbance rejection, decoupling designing procedure and simple implementation (UTKIN, 1993).

Let us consider the state space representation of a generic dynamic system be:

$$\dot{\boldsymbol{x}} = \boldsymbol{f}(t, \boldsymbol{x}, \boldsymbol{u}) \ , \tag{62}$$

with

$$\boldsymbol{u} = \begin{cases} \boldsymbol{u}^{+}_{(x)} & if\ s(x) > 0 \\ \boldsymbol{u}^{-}_{(x)} & if\ s(x) < 0 \end{cases} , \tag{63}$$

where $\boldsymbol{x} \in \mathbb{R}^n$ is the state space n-dimensional vector of the system, $\boldsymbol{f}(t, \boldsymbol{x}, \boldsymbol{u}) \in \mathbb{R}^n$, and $\boldsymbol{u}$ is a scalar control action with discontinuous function. The sliding surface $s(x)$ is a closed space in the state space defined as:

$$\{x(t) |\ s(x) = 0\} \, . \tag{64}$$

Therefore, the problem of designing a sliding mode control system consists in choosing the appropriate sliding variable s, and afterwards, design the appropriate control function u to drive the system to the sliding surface (RIBEIRO, 2006).

According to (BARBASHIN, 1967), the sliding mode exists on a discontinuous surface whenever the distances to this surface and the velocity of its change are of opposite signs, at the vicinities of the sliding manifold, i.e. when:

$$lim_{s\to 0^+}\ \dot{s} < 0 \quad \text{and} \quad lim_{s\to 0^-}\ \dot{s} > 0\,. \tag{65}$$

This condition is achieved if the control action guarantees the reachability criterion, given by (66), where η is a strictly positive constant:

$$\frac{d}{dt}\left(\frac{1}{2}s^2(x)\right) \leq -\eta|s(x)|\ . \tag{66}$$

As will be seen, it will be chosen $s(x_1) = x_1$, and therefore:

$$\frac{d}{dt}\left(\frac{1}{2}s^2(x)\right) = \frac{2}{2}s(x_1)\frac{ds(x_1)}{dt} \ = s(x_1)\ \dot{s}(x_1)\,, \tag{67}$$

or

$$s(x)\,\dot{s}(x) \leq -\eta|s(x)|\ , \tag{68}$$

meaning that the multiplication of the sliding variable s by its temporal derivate results in a negative number, satisfying the existence condition (65).

In order to apply the aforementioned control strategy in the interferometric system (shown in Figure 5), a suitable state space modeling is carried out in the next section, as well as the choice of the sliding surface and control law.

3.1 Sliding mode control applied to the interferometric system

The modified Michelson interferometer, showed in Figure 5, was assembled with the mirrors M1 and M2 attached at PZT1 and PZT2 respectively. The PZT at the sensor arm is used to induce the signal of interest $\Delta\phi$, while the PZT at the reference arm is responsible to induce the phase correction signal ϕ_c.

A block diagram of the interferometric dynamic system is shown in Figure 10, for $\phi = \Delta\phi + \phi_0 + \phi_c$ and where it was chosen the output signal of the photodetector 1, without the DC component (A_1 in (37)), as a state space variable, leading to:

Figure 10 - Block diagram of the interferometric dynamic system.

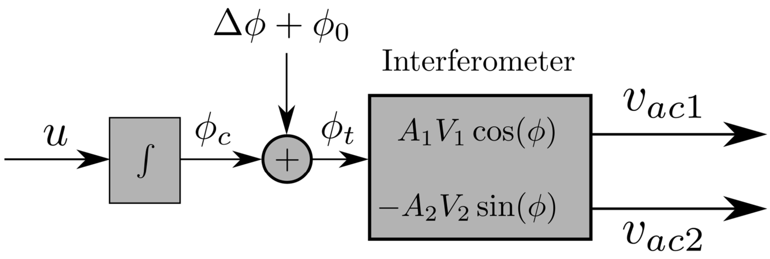

Source: elaborated by the author.

$$v_{ac1} = A_1V_1cos(\phi_c + \Delta\phi + \phi_0) = x_{1(t)}\,, \tag{69}$$

and so

$$\begin{aligned}\dot{x}_{1(t)} &= \frac{d}{dt}\big(A_1V_1cos(\phi_c + \Delta\phi + \phi_0)\big)\\ &= -A_1V_1sin(\phi_c + \Delta\phi + \phi_0)\big(\dot{\phi}_c + \Delta\dot{\phi} + \dot{\phi}_0\big).\end{aligned} \tag{70}$$

Defining the function $f(\phi_c + \Delta\phi + \phi_0)$ as:

$$f(\phi_c, \Delta\phi, \phi_0) = -A_1V_1\sin(\phi_c + \Delta\phi + \phi_0), \tag{71}$$

which will be referred as f for simplicity of notation, and substituting equation (71) in equation (70), leads to:

$$\dot{x}_{1(t)} = f\,\dot{\phi}_c + f\big(\Delta\dot{\phi} + \dot{\phi}_0\big). \tag{72}$$

According to Figure 10,

$$\dot{\phi}_c = u\,, \tag{73}$$

and so

$$\dot{x}_{1(t)} = f\,u + f\,\big(\Delta\dot{\phi} + \dot{\phi}_0\big)\,. \tag{74}$$

Regarding now the output signal of the photodetector 2, without DC component (A_2 in (38)), and equation (74), v_{ac2} can be written as:

$$v_{ac2} = \frac{A_2V_2}{A_1V_1}f = -A_2V_2\sin(\phi_c + \Delta\phi + \phi_0)\,. \tag{75}$$

Following the nomenclature established by Udd and Spillman (2011), the high-gain approach considers the signals $\Delta\phi + \phi_0$ as disturbances to be rejected, while keeping the interferometer operating at one of the quadrature points, where the output $v_{ac1} = A_1V_1\cos(\Delta\phi + \phi_0 + \phi_c) = 0$. Thereby, a suitable choice for the sliding variable is:

$$s(x_1) = v_{ac1} = x_1, \tag{76}$$

or

$$s(x_1) = A_1 V_1 \cos(\phi_c + \Delta\phi + \phi_0)\,. \tag{77}$$

Let us now use the equivalent control method as described by (UTKIN, 1977) to obtain the equations of the phase correction signal ϕ_c. This method is used to obtain the control signal of a continuous dynamic system equivalent to the original discontinuous one, considering that the system is confined in the sliding surface. This means that $s(x) = 0$ and $\dot{s}(x) = 0$ as well, therefore:

$$\begin{cases} s(x) = x_1 = 0 \\ \dot{s}(x) = \dot{x}_1 = 0 \end{cases} \Leftrightarrow \begin{cases} \phi_c = -\Delta\phi - \phi_0 + \dfrac{k\pi}{2} \\ \dot{\phi}_c = -\Delta\dot{\phi} - \dot{\phi}_0 \end{cases} \quad \text{where k is odd.} \tag{78}$$

From (78) it can be seen that for the system confined to the sliding surface, ϕ_c will follow the displacements induced between the interferometer arms. This result can be interpreted as illustrated in Figure 11, where it is presented the transfer curves taking as input the total phase shift at the input of the interferometer adding the equilibrium point to which the system initially converged. For the system obeying the reachability criterion (as it will be further explained), the operation of the system will be confined to one of the straight lines.

Figure 11 - Transfer curves of ϕ_c in relation to $\Delta\phi + \phi_0$.

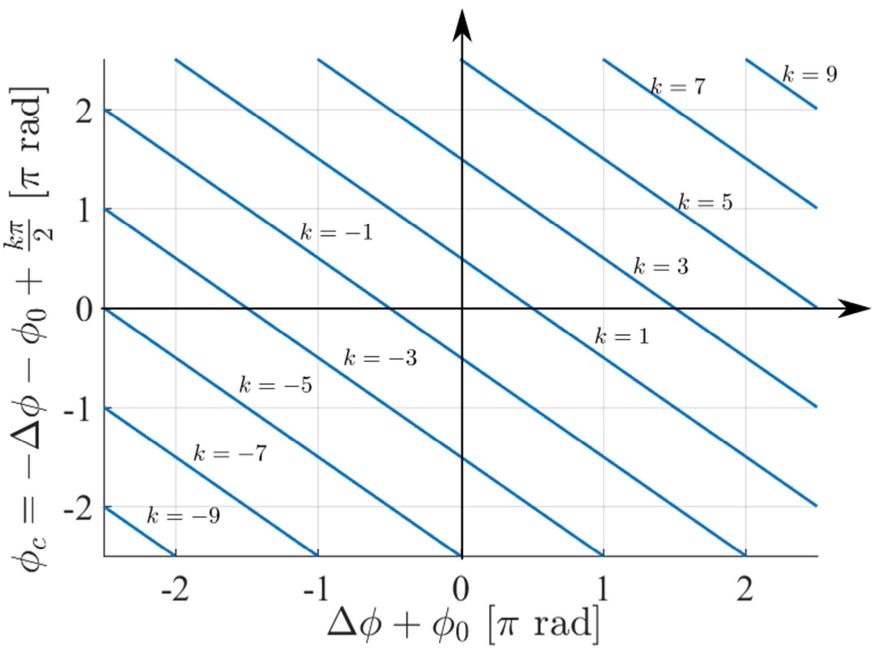

Source:(elaborated by the author).

It is necessary now, to obey the reachability criterion, thus ensuring the convergence of the system trajectory to the sliding surface. By the substitution of equation (77) in equation (67) and remembering that $u = \dot{\phi}_c$, the following expression is obtained:

$$s_{(x_1)}\dot{s}_{(x_1)} = A_1V_1\cos(\phi_c + \Delta\phi + \phi_0)\,[-A_1V_1\sin(\phi_c + \Delta\phi + \phi_0)]\big(\dot{\phi}_c + \Delta\dot{\phi} + \dot{\phi}_0\big)\,, \tag{79}$$

or

$$s_{(x_1)}\dot{s}_{(x_1)} = (x_1 f)\big(u + \Delta\dot{\phi} + \dot{\phi}_0\big). \tag{80}$$

Choosing the control law as:

$$u = -Csign(x_1 f), \tag{81}$$

and substituting in equation (80), it is obtained:

$$s_{(x_1)}\dot{s}_{(x_1)} = (x_1 f)\big(-Csign(x_1 f) + \Delta\dot{\phi} + \dot{\phi}_0\big)\,. \tag{82}$$

The block diagram of the closed-loop system with this control law is represented in Figure 12, where $v_{ac2} = f(x_1)$, considering $A_1V_1 = A_2V_2$. However this is not a necessary condition for the correct work of the control system, once that the multiplication $(x_1 f)$ is inside the argument of "$sign$" function.

Figure 12 – Closed-loop system

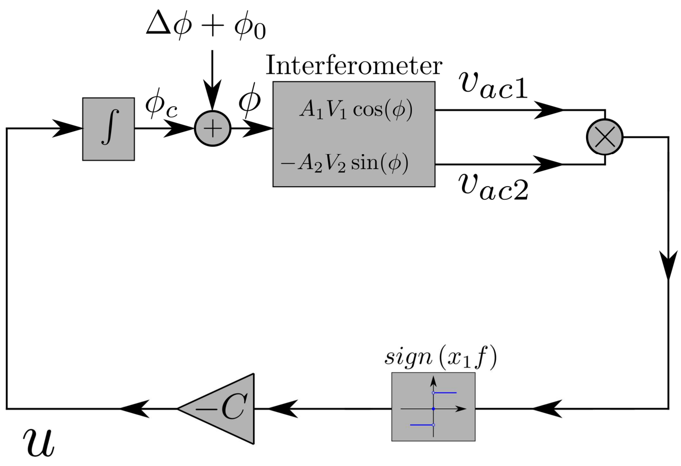

Source: elaborated by the author.

The parameter C is the total gain of the feedback system and $(x) = \begin{cases} -1, & if\ \ x < 0 \\ +1, & if\ \ x > 0 \end{cases}$, is the sign function.

It is known that the function $|x|$ and $sign(x)$ are related by $|x| = x\, sign(x)$, and $x = |x| sign(x)$. Therefore, equation (82) can be rewritten as:

$$s_{(x_1)}\dot{s}_{(x_1)} = -C(x_1 f)sign(x_1 f) + (x_1 f)\left(\Delta\dot{\phi} + \dot{\phi}_0\right), \tag{83}$$

or

$$s_{(x_1)}\dot{s}_{(x_1)} = -C(x_1 f)sign(x_1 f) + (x_1 f)sign^2(x_1 f)\left(\Delta\dot{\phi} + \dot{\phi}_0\right), \tag{84}$$

or else

$$s_{(x_1)}\dot{s}_{(x_1)} = \left(-C + \left(\Delta\dot{\phi} + \dot{\phi}_0\right)sign(x_1 f)\right)\ (x_1 f)sign(x_1 f). \tag{85}$$

Choosing $C > C_n + \left|\Delta\dot{\phi} + \dot{\phi}_0\right| sign(x_1 f)$, where C_n is a strictly positive constant, leads to:

$$\begin{aligned} s_{(x_1)}\dot{s}_{(x_1)} < \Big(-\left(C_n + \left|\Delta\dot{\phi} + \dot{\phi}_0\right| sign(x_1 f)\right) \\ + \left(\Delta\dot{\phi} + \dot{\phi}_0\right)sign(x_1 f)\Big)\ (x_1 f)sign(x_1 f), \end{aligned} \tag{86}$$

or

$$s_{(x_1)}\dot{s}_{(x_1)} < (x_1 f)\left(\Delta\,\dot{\phi} + \dot{\phi}_0\right) - C_n|x_1 f| - \left|\Delta\,\dot{\phi} + \dot{\phi}_0\right||x_1 f|\,. \tag{87}$$

It can be seen that the upper bound of the right side of equation (87) occurs when $(x_1 f) > 0$ and $\left(\Delta\,\dot{\phi} + \dot{\phi}_0\right) > 0$, or, when $(x_1 f) < 0$ and $\left(\Delta\,\dot{\phi} + \dot{\phi}_0\right) < 0$. Both cases lead to:

$$s_{(x_1)}\dot{s}_{(x_1)} \leq\ -C_n|f||x_1|\,. \tag{88}$$

From equation (88), it can be seen that the reachability criterium is satisfied for every $f \neq 0$. In other words, for every initial condition of the argument of the function f such that $\Delta\phi + \phi_0 + \phi_c \neq k\pi, k \in \mathbb{Z}$, the system will reach and remain within the sliding surface.

Finally, considering $\eta = C_n|f|$, the following expression is obtained:

$$s_{(x_1)}\dot{s}_{(x_1)} <\ -\eta\left|s_{(x_1)}\right|. \tag{89}$$

3.2 Stability Analysis

In this Section, the study of the closed-loop system stability is carried out, using an analytical method through the variation rates of the state variables in the vicinities of the equilibrium points. For this purpose, it is considered that the system is without disturbance inputs. Afterwards, a graphical approach is used to give a more intuitive understanding of the control action, by comparing the control signal and the characteristic output curve of the interferometer.

3.2.1 Equilibrium points

First the equilibrium points of the closed-loop system must be determined. These are points where the variation rates of the state space variables are equal to zero, let us consider $\Delta\phi + \phi_0 = 0$, and denote such points by ϕ_c^*. Regarding equation (74) the equilibrium points can be obtained as follows:

$$\dot{x}_1(t) = fu \ . \tag{90}$$

Substituting (81),

$$\dot{x}_1(t) = f\big(-Csign(x_1 f)\big), \tag{91}$$

and using $sign[x_1(\phi_c^*) f(\phi_c^*)] = sign[x_1(\phi_c^*)]\ sign[f(\phi_c^*)]$, together with $x = |x| sign(x)$,

$$\dot{x}_{1(t)} = -C|f(\phi_c^*)| sign[x_1(\phi_c^*)] \ = 0, \tag{92}$$

where two conditions are originated:

$$f(\phi_c^*) = -A_1 V_1 \sin(\phi_c^*) = 0 \qquad \Rightarrow \quad \phi_c^* \ = k\pi \ , \qquad k \in \mathbb{Z} \tag{93}$$

from (71), or,

$$sign[x_1(\phi_c^*)] = sign[A_1 V_1 \cos(\phi_c^*)\ ] = 0 \Rightarrow \phi_c^* = \frac{\pi}{2} + k\pi\ , k \in \mathbb{Z} \tag{94}$$

The union of the conditions gives origin to the equilibrium points:

$$\phi_c^* = \frac{k\pi}{2} \qquad , \quad k \in \ \mathbb{Z} \tag{95}$$

3.2.2 Analytical method

The stability of the state variable x_1 at the vicinities of the equilibrium points can be studied through the lateral limits of $\dot{x}_1$, tending to the equilibrium points. First the equilibrium points are divided in the following four sets: $\left\{ \phi_c^* = -\frac{\pi}{2} + 2k\pi \ |k \in \mathbb{Z}\right\}$, $\left\{ \phi_c^* = \frac{\pi}{2} + 2k\pi \ |k \in \mathbb{Z}\right\}$, $\{ \phi_c^* = 2k\pi \ |k \in \mathbb{Z}\}$, and $\{ \phi_c^* = (2k+1)\pi \ |k \in \mathbb{Z}\}$, due to the differences in the inclination, positivity and negativity of the points in the interferometric curve. Then, after applying the lateral limits, if the value of $\dot{x}_1$ forces the system trajectory to the equilibrium point, it is classified as stable, otherwise, it is an unstable equilibrium point:

a) For $\phi_c^* = -\frac{\pi}{2} + 2k\pi$:

$$\lim_{\phi_c \to \left(-\frac{\pi}{2}+2k\pi\right)^-} \dot{x}_1(\phi_c) = \lim_{\phi_n \to \left(-\frac{\pi}{2}\right)^-} \dot{x}_1(\phi_n + 2k\pi) \,, \tag{96}$$

or

$$\lim_{\phi_n \to \left(-\frac{\pi}{2}\right)^-} \dot{x}_1 = \lim_{\phi_n \to -\frac{\pi}{2}^-} \Big(-C|f(\phi_n + 2k\pi)| sign\big(x_1(\phi_n + 2k\pi)\big)\Big) \,, \tag{97}$$

or

$$\lim_{\phi_n \to -\frac{\pi}{2}^-} \dot{x}_1 = \lim_{\phi_n \to -\frac{\pi}{2}^-} \big(-C|-A_1V_1 \sin(\phi_n + 2k\pi)| sign(A_1V_1 \cos(\phi_n + 2k\pi))\big) \tag{98}$$

or

$$\lim_{\phi_n \to -\frac{\pi}{2}^-} \dot{x}_1 = \lim_{\phi_n \to -\frac{\pi}{2}^-} \big(-C|-A_1V_1 \sin(\phi_n)| sign(A_1V_1 \cos(\phi_n))\big) \tag{99}$$

or

$$\lim_{\phi_n \to -\frac{\pi}{2}^-} \dot{x}_1 = CA_1V_1 > 0 \tag{100}$$

This indicates that for ϕ_c less than $-\frac{\pi}{2} + 2k\pi$, but infinitesimally close to $-\frac{\pi}{2} + 2k\pi$, the variable x_1 will increase its value. By the other hand,

$$\lim_{\phi_c \to \left(-\frac{\pi}{2}+2k\pi\right)^+} \dot{x}_1(\phi_c) = \lim_{\phi_n \to \left(-\frac{\pi}{2}\right)^+} \dot{x}_1(\phi_n + 2k\pi) \,, \tag{101}$$

or

$$\lim_{\phi_n \to -\frac{\pi}{2}^+} \dot{x}_1 = \lim_{\phi_n \to -\frac{\pi}{2}^+} \Big(-C|f(\phi_n + 2k\pi)| sign\big(x_1(\phi_n + 2k\pi)\big)\Big) \,, \tag{102}$$

or

$$\lim_{\phi_n \to -\frac{\pi}{2}^+} \dot{x}_1 = \lim_{\phi_n \to -\frac{\pi}{2}^+} \big(-C|-A_1V_1 \sin(\phi_n + 2k\pi)| sign(A_1V_1 \cos(\phi_n + 2k\pi))\big) \,, \tag{103}$$

or

$$\lim_{\phi_n \to -\frac{\pi}{2}^+} \dot{x}_1 = \lim_{\phi_n \to -\frac{\pi}{2}^+} \left(-C|-A_1V_1 \sin(\phi_n)| sign(A_1V_1 \cos(\phi_n))\right), \tag{104}$$

or

$$\lim_{\phi_n \to -\frac{\pi}{2}^+} \dot{x}_1 = -CA_1V_1 < 0\,. \tag{105}$$

This result demonstrates that for ϕ_c greater than $-\frac{\pi}{2} + 2k\pi$, but infinitesimally close to $-\frac{\pi}{2} + 2k\pi$, the variable x_1 will decrease its value.

These points $\phi_c^* = -\frac{\pi}{2} + 2k\pi$ are stable, as it can be seen in Figure 13, where the interferometer output characteristic curve, $x_1 = A_1V_1 \cos(\phi_c)$, is negative for $\phi_c \to \left(-\frac{\pi}{2} + 2k\pi\right)^-$ and the value of x_1 increases. While, for $\phi_c \to \left(-\frac{\pi}{2} + 2k\pi\right)^+$ the variable x_1 is positive and the value of x_1 decreases, thereby in both conditions the value of x_1 is pushed to zero.

The analysis will be carried out, considering now the points where $\phi_c^* = \frac{\pi}{2} + 2k\pi$, $k \in \mathbb{Z}$.

b) For $\phi_c^* = \frac{\pi}{2} + 2k\pi$:

$$\lim_{\phi_c \to \left(\frac{\pi}{2} + 2k\pi\right)^-} \dot{x}_{1(\phi_c)} = \lim_{\phi_n \to \left(\frac{\pi}{2}\right)^-} \dot{x}_1(\phi_n + 2k\pi)\,, \tag{106}$$

or

$$\lim_{\phi_n \to \frac{\pi}{2}^-} \dot{x}_1 = \lim_{\phi_n \to \frac{\pi}{2}^-} \left(-C|f(\phi_n + 2k\pi)| sign\big(x_1(\phi_n + 2k\pi)\big)\right), \tag{107}$$

or

$$\lim_{\phi_n \to \frac{\pi}{2}^-} \dot{x}_1 = \lim_{\phi_n \to \frac{\pi}{2}^-} \left(-C|-A_1V_1 \sin(\phi_n + 2k\pi)| sign(A_1V_1 \cos(\phi_n + 2k\pi))\right), \tag{108}$$

or

$$\lim_{\phi_n \to \frac{\pi}{2}^-} \dot{x}_1 = \lim_{\phi_n \to \frac{\pi}{2}^-} \left(-C|-A_1V_1 \sin(\phi_n)| sign(A_1V_1 \cos(\phi_n))\right), \tag{109}$$

or

$$\lim_{\phi_n \to \frac{\pi}{2}^-} \dot{x}_1 = -CA_1V_1 < 0\ . \tag{110}$$

It can be seen, that for ϕ_c less than $\frac{\pi}{2} + 2k\pi$, but infinitesimally close to $\frac{\pi}{2} + 2k\pi$, the variable x_1 will decrease its value. By the other hand,

$$\lim_{\phi_c \to \left(\frac{\pi}{2}+2k\pi\right)^+} \dot{x}_1(\phi_c) = \lim_{\phi_n \to \left(\frac{\pi}{2}\right)^+} \dot{x}_1(\phi_n + 2k\pi) \,, \tag{111}$$

or

$$\lim_{\phi_n \to \frac{\pi}{2}^+} \dot{x}_1 = \lim_{\phi_n \to \frac{\pi}{2}^+} \Big(-C|f(\phi_n + 2k\pi)|sign\big(x_1(\phi_n + 2k\pi)\big)\Big) \,, \tag{112}$$

or

$$\lim_{\phi_n \to \frac{\pi}{2}^+} \dot{x}_1 = \lim_{\phi_n \to \frac{\pi}{2}^+} \big(-C|-A_1V_1 \sin(\phi_n + 2k\pi)|sign(A_1V_1 \cos(\phi_n + 2k\pi))\big) \,, \tag{113}$$

or

$$\lim_{\phi_n \to \frac{\pi}{2}^+} \dot{x}_1 = \lim_{\phi_n \to \frac{\pi}{2}^+} \big(-C|-A_1V_1 \sin(\phi_n)|sign(A_1V_1 \cos(\phi_n))\big) \,, \tag{114}$$

or

$$\lim_{\phi_n \to \frac{\pi}{2}^+} \dot{x}_1 = CA_1V_1 > 0 \ . \tag{115}$$

This result shows that for ϕ_c greater than $\frac{\pi}{2} + 2k\pi$, but infinitesimally close to $\frac{\pi}{2} + 2k\pi$, the variable x_1 will increase its value.

Again, it can be seen that these are stable equilibrium points, where the interferometer output characteristic curve, $x_1 = A_1V_1 \cos(\phi_c)$, showed in Figure 13, is positive for $\phi_c \to \left(\frac{\pi}{2} + 2k\pi\right)^-$ and the value of x_1 decreases. While, for $\phi_c \to \left(\frac{\pi}{2} + 2k\pi\right)^+$ the variable x_1 is negative and the value of x_1 increases, thereby in both conditions the value of x_1 is pushed to zero.

The same procedure will be followed for the points where $\phi_c^* = 2k\pi$, $k \in \mathbb{Z}$ and for the points where $\phi_c^* = (2k+1)\pi$, $k \in \mathbb{Z}$.

c) For $\phi_c^* = 2k\pi$:

$$\lim_{\phi_c \to (2k\pi)^-} \dot{x}_1(\phi_c) = \lim_{\phi_n \to 0^-} \dot{x}_1(\phi_n + 2k\pi) \,, \tag{116}$$

or

$$\lim_{\phi_n \to 0^-} \dot{x}_1 = \lim_{\phi_n \to 0^-} \left(-C|f(\phi_n + 2k\pi)|sign\left(x_1(\phi_n + 2k\pi)\right)\right), \tag{117}$$

or

$$\lim_{\phi_n \to 0^-} \dot{x}_1 = \lim_{\phi_n \to 0^-} \left(-C|-A_1V_1 \sin(\phi_n + 2k\pi)|sign(A_1V_1 \cos(\phi_n + 2k\pi))\right), \tag{118}$$

or

$$\lim_{\phi_n \to 0^-} \dot{x}_1 = \lim_{\phi_n \to 0^-} \left(-C|-A_1V_1 \sin(\phi_n)|sign(A_1V_1 \cos(\phi_n))\right), \tag{119}$$

or

$$\lim_{\phi_n \to 0^-} \dot{x}_1 \to 0^- . \tag{120}$$

In such a way that for ϕ_c less than $2k\pi$, but infinitesimally close to $2k\pi$, the variable x_1 will decrease its value. Otherwise,

$$\lim_{\phi_c \to (2k\pi)^+} \dot{x}_1(\phi_c) = \lim_{\phi_n \to 0^+} \dot{x}_1(\phi_n + 2k\pi), \tag{121}$$

or

$$\lim_{\phi_n \to 0^+} \dot{x}_1 = \lim_{\phi_n \to 0^+} \left(-C|f(\phi_n + 2k\pi)|sign\left(x_1(\phi_n + 2k\pi)\right)\right), \tag{122}$$

or

$$\lim_{\phi_n \to 0^+} \dot{x}_1 = \lim_{\phi_n \to 0^+} \left(-C|-A_1V_1 \sin(\phi_n + 2k\pi)|sign(A_1V_1 \cos(\phi_n + 2k\pi))\right), \tag{123}$$

or

$$\lim_{\phi_n \to 0^+} \dot{x}_1 = \lim_{\phi_n \to 0^+} \left(-C|-A_1V_1 \sin(\phi_n)|sign(A_1V_1 \cos(\phi_n))\right), \tag{124}$$

or

$$\lim_{\phi_n \to 0^+} \dot{x}_1 \to 0^- . \tag{125}$$

One can see that for ϕ_c greater than $2k\pi$, but infinitesimally close to $2k\pi$, the variable x_1 will decrease its value. Therefore, these points are unstable, since they are the maximum points of the interferometric curve, and, from both sides, the variation rate of x_1 is negative, moving the system away from these equilibrium points. This behavior is illustrated in Figure 13.

d) For $\phi_c^* = (2k + 1)\pi$:

$$\lim_{\phi_c \to (2k+1)\pi^-} \dot{x}_1(\phi_c) = \lim_{\phi_n \to \pi^-} \dot{x}_1(\phi_n + 2k\pi) , \tag{126}$$

or

$$\lim_{\phi_n \to \pi^-} \dot{x}_1 = \lim_{\phi_n \to \pi^-} \Big(-C|f(\phi_n + 2k\pi)|sign\big(x_1(\phi_n + 2k\pi)\big)\Big) , \tag{127}$$

or

$$\lim_{\phi_n \to \pi^-} \dot{x}_1 = \lim_{\phi_n \to \pi^-} \big(-C|-A_1V_1 \sin(\phi_n + 2k\pi)|sign(A_1V_1 \cos(\phi_n + 2k\pi))\big) , \tag{128}$$

or

$$\lim_{\phi_n \to \pi^-} \dot{x}_1 = \lim_{\phi_n \to \pi^-} \big(-C|-A_1V_1 \sin(\phi_n)|sign(A_1V_1 \cos(\phi_n))\big) , \tag{129}$$

or

$$\lim_{\phi_n \to \pi^-} \dot{x}_1 \to 0^+ . \tag{130}$$

It can be seen that the points $\phi_c^* = (2k+1)\pi$ are the points of minimum in the interferometric curve, and when $\phi_c \to (2k+1)\pi^-$ the value of x_1 is negative while $\dot{x}_1$ is positive, implying in the growth of x_1. Otherwise,

$$\lim_{\phi_c \to (2k+1)\pi^+} \dot{x}_1(\phi_c) = \lim_{\phi_n \to \pi^+} \dot{x}_1(\phi_n + 2k\pi) , \tag{131}$$

or

$$\lim_{\phi_n \to \pi^+} \dot{x}_1 = \lim_{\phi_n \to \pi^+} \Big(-C|f(\phi_n + 2k\pi)|sign\big(x_1(\phi_n + 2k\pi)\big)\Big) , \tag{132}$$

or

$$\lim_{\phi_n \to \pi^+} \dot{x}_1 = \lim_{\phi_n \to \pi^+} \big(-C|-A_1V_1 \sin(\phi_n + 2k\pi)|sign(A_1V_1 \cos(\phi_n + 2k\pi))\big) , \tag{133}$$

or

$$\lim_{\phi_n \to \pi^+} \dot{x}_1 = \lim_{\phi_n \to \pi^+} \big(-C|-A_1V_1 \sin(\phi_n)|sign(A_1V_1 \cos(\phi_n))\big) , \tag{134}$$

or

$$\lim_{\phi_n \to \pi^+} \dot{x}_1 \to 0^+ . \tag{135}$$

This result shows an unstable behavior of the minimum value points of the interferometric curve, $\phi_c^* = (2k+1)\pi$, considering that x_1 is negative and from both sides, x_1 increases, moving away from these equilibrium points.

Figure 13 - Stability of the output characteristic curve of the interferometer.

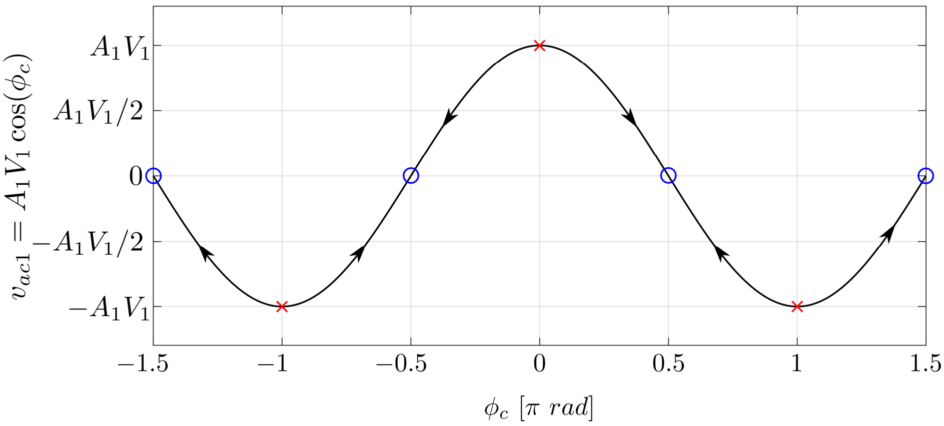

Source: elaborated by the author.

Considering now the hypothesis of the initial condition of the system be $\Delta\phi + \phi_0 + \phi_c = k\pi$ for $k \in \mathbb{Z}$, i.e. $f = 0$, the system will remain in this position only if $\dot{f}$ is equal to zero to every subsequent time. The expression of $\dot{f}$ is obtained from (71), (73) and (81), and is given by:

$$\dot{f} = -A_1 V_1 \cos(\Delta\phi + \phi_0 + \phi_c)\left[\Delta\,\dot{\phi} + \dot{\phi}_0 - C\,sgn(x_1 f)\right]. \tag{136}$$

In this initial condition $cos(\Delta\phi + \phi_0 + \phi_c)$ will be equal to $+1$ or -1, therefore, from equation (136), $\dot{f} = \mp A_1V_1\left[\Delta\,\dot{\phi} + \dot{\phi}_0 - C\,sgn(x_1 f)\right]$, which will be zero only if $\Delta\,\dot{\phi} + \dot{\phi}_0 - C\,sgn(x_1 f) = 0$. Even if such condition happens in an initial state it will not hold for the subsequent time due to the variation of $\Delta\,\dot{\phi} + \dot{\phi}_0$ and the repulsion around $f = 0$, therefore when $f \neq 0$ the reachability criterium holds and the system converges to the sliding surface.

3.2.3 Graphical interpretation

Another intuitive approach that can be used to study the behavior of the system is the graphical analysis of the state variable x_1 and the control signal u, which are plotted in Figure 14. Let us rewrite the control signal as (from (69), (71) and (81)):

$$u = -Csign[(A_1V_1\cos(\phi_c))(-A_1V_1\sin(\phi_c))], \tag{137}$$

or

$$u = -Csign\left[-\frac{(A_1V_1)^2}{2}\sin(2\phi_c)\right] = Csign\left[\frac{(A_1V_1)^2}{2}\sin(2\phi_c)\right]. \tag{138}$$

Figure 14 - Output of the interferometer and control signal u considering $C = A_1V_1$.

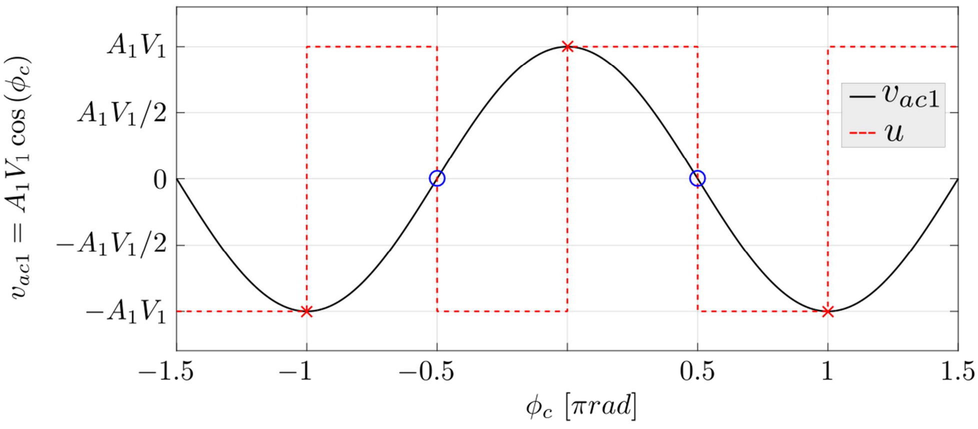

Source: elaborated by the author.

According to (73), the phase correction signal ϕ_c is equal to the integral of the control signal u, represented as the red traced line. Therefore, if $u > 0$, ϕ_c increases, and for $u < 0$, ϕ_c decreases. Note that in Figure 13, when traversing the ϕ_c-axis in the increasing direction, the locals where the control signal changes from positive to negative values constitute stable equilibrium points. Once that if ϕ_c is to the left of this point, the control signal forces the phase correction signal to increase, while if ϕ_c is to the right, u will force ϕ_c to decrease. The inverse behavior is observed when the control signal transition goes from negative to positive values.

It is noteworthy that the points $\left\{ \phi_c^* = -\frac{\pi}{2} + 2k\pi \,|k \in \mathbb{Z}\right\}$ and $\left\{ \phi_c^* = \frac{\pi}{2} + 2k\pi \,|k \in \mathbb{Z}\right\}$ are interpreted as stable equilibrium points, while $\{ \phi_c^* = 2k\pi \,|k \in \mathbb{Z}\}$, and $\{ \phi_c^* = (2k + 1)\pi \,|k \in \mathbb{Z}\}$ are unstable ones, in agreement with the analytical method. Also the different stable equilibrium points as, for instance, $\frac{\pi}{2}$ and $-\frac{\pi}{2}$, have opposite sign slopes in the interferometer characteristic curve, and therefore, a phase shift of π radians is introduced when working at the points $\left\{ \phi_c^* = \frac{\pi}{2} + 2k\pi \,|k \in \mathbb{Z}\right\}$. However for the operation using the high gain approach, this behavior does not induce ambiguity in direction, because the system always generate a phase correction signal to suppress the phase disturbances at the input of the interferometer. For example, if the system is working at the operation point $\phi_c^* = -\frac{\pi}{2}$, the slope of the interferometric curve is positive and therefore, a disturbance in the positive direction of the phase $\Psi = \Delta\phi + \phi_0$ will cause a reaction, decreasing the value of ϕ_c . Considering now the interferometer working at the operation point $\phi_c^* = \frac{\pi}{2}$, if any phase disturbance in the positive direction of $\Psi = \Delta\phi + \phi_0$ occurs, the control action again will decrease the value of ϕ_c, as it can be seen by the sign of the control signal in the region between $\frac{\pi}{2}$ and π in Figure 13.

The next step in the development of this work was to carry out the closed-loop simulations, using the software MATLAB and Simulink. The methodology and obtained results are explained in Section 3.3.

3.3 Simulation of the closed-loop system

Firstly the system comprising the interferometer and the control law was assembled in the software Simulink. The block diagram is shown in Figure 15.

Figure 15 – Closed-loop block diagram in Simulink software.

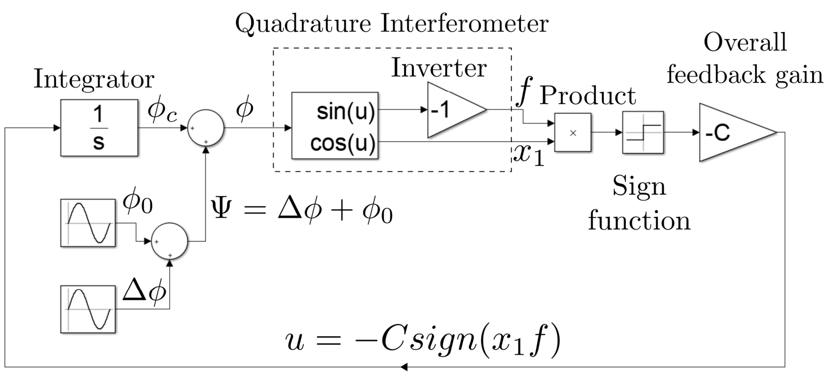

Source: elaborated by the author.

The signal generator blocks are responsible to simulate the input signals ϕ_0 and $\Delta\phi$. They were firstly configured with amplitudes of 1 radian peak and frequencies of 3 Hz and 500 Hz respectively. The modified Michelson interferometer is represented as the block with sine and cosine outputs and the inverter, generating the signals $x_1 = v_{ac1} = A_1V_1\cos(\Delta\phi + \phi_0 + \phi_c)$ and $f = v_{ac2} = -A_2V_2\sin(\Delta\phi + \phi_0 + \phi_c)$, with the parameters A_1V_1 and A_2V_2 set to the unity value. The control signal $u = -Csign(x_1 f)$ is formed with the blocks Product, Sign and gain –C. The block Sign implements the relay function, responsible for the discontinuous control action and the gain –C represents the total overall gain of the closed-loop. Obeying the reachability condition, the overall gain of the closed-loop can be chosen as:

$$C = C_n > \left|\Delta\dot{\phi} + \dot{\phi}_0\right| . \tag{139}$$

A sufficient condition, to guarantee the stability of the system, is to choose:

$$C_n > |\Delta\dot{\phi}| + |\dot{\phi}_0| \geq |\Delta\dot{\phi} + \dot{\phi}_0| \, , \tag{140}$$

for

$$\begin{cases} \Delta\phi = \sin(2\pi 500t) \\ \Delta\dot{\phi} = 2\pi 500 \cos(2\pi 500t) \end{cases} , \tag{141}$$

and so

$$\Delta\dot{\phi} \cong 3141.6 \cos(3141.6t) \, . \tag{142}$$

Also

$$\begin{cases} \phi_0 = \sin(2\pi 3t) \\ \dot{\phi}_0 = 2\pi 3 \cos(2\pi 3t) \end{cases} , \tag{143}$$

and so

$$\dot{\phi}_0 \cong 18.85 \cos(18{,}85t). \tag{144}$$

Then, (140) leads to $C_n > 3141.6 + 18.85 = 3160.4$, and thus, C_n can be chosen as $C_n = 3200$.

The simulations were performed using the solver ODE3 with the step sizes (dt) of 100 μs, 10 μs and 1 μs, to study the influence of the sampling period on the control system. The results of the output signal $x_1 = A_1 V_1 cos(\phi)$, for $\phi = \Delta\phi + \phi_0 + \phi_c$, are shown in Figure 16. It is noted that with the decrease of the sampling period, the output signal becomes increasingly closer to zero, remembering that in the high gain approach the objective is to fully compensate the signals of interest and spurious disturbances, thereby the phase correction signal becomes $\phi_c = -\Delta\phi - \phi_0 + \frac{k\pi}{2}$ for k odd.

Figure 16 – Simulated interferometer output signal $x_1 = AVcos\ (\phi)$ for different sampling periods (dt).

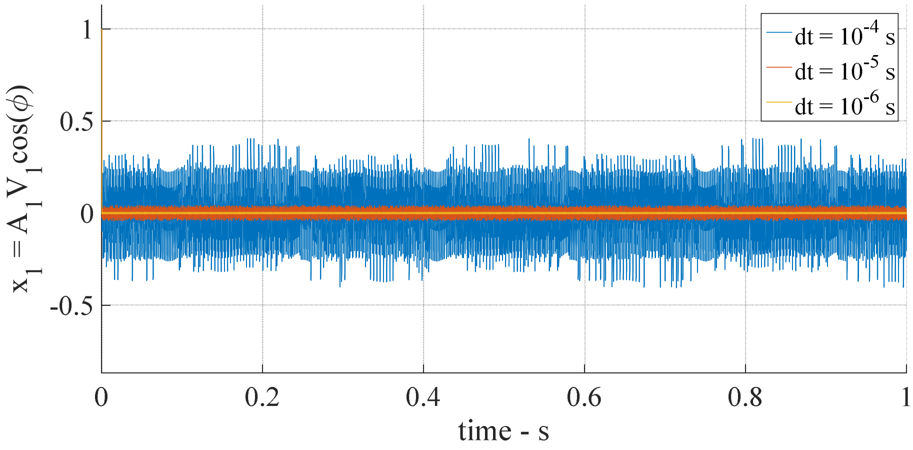

Source: elaborated by the author.

In Figures 17 and 18 are shown the signals $\Delta\phi + \phi_0$ and $-\phi_c$, simulated with sampling period of 10 μs and 1 μs respectively, after a first order Butterworth high-pass filter with cutoff frequency of 20 Hz. The filtering process attenuates the spurious disturbances ϕ_0 so the signal of interest $\Delta\phi$ can be compared to the phase correction signal.

Figure 17 - Phase correction signal and $\phi_0 + \Delta\phi$ for 10 μs of sampling period

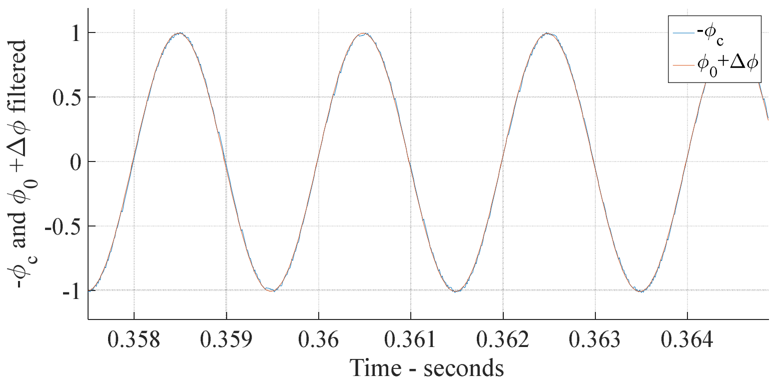

Source: elaborated by the author.

Figure 18- Phase correction signal and $\phi_0 + \Delta\phi$ for 1 μs of sampling period

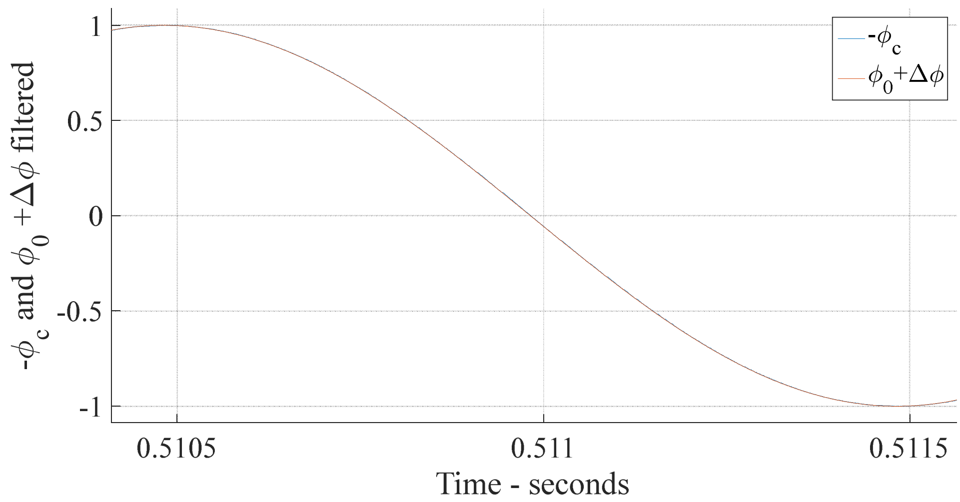

Source: elaborated by the author.

The results show again that the smaller the sampling period, the closer the phase correction signal is to the signals $\Delta\phi + \phi_0$, demonstrating its capability to operate in high gain mode.

The amplitude values of both ϕ_0 and $\Delta\phi$ were changed to 4 radians, therefore, the overall gain needed to be increased to satisfy the reachability criterion, resulting in $\Delta\phi = 4\sin(2\pi 500t)$, $\phi_0 = 4\sin(2\pi 3) \Rightarrow C > 12642$, were it was chosen $C = 12800$ as a sufficient condition. Then simulations where performed in order to verify the convergence to the stable equilibrium points. The behavior in open- and closed-loop of x_1 and f are respectively shown in Figures 19 and 20, regarding the input phase shift given by $\phi_0 + \Delta\phi$ and initial condition chosen as $\phi_c + \phi_0 + \Delta\phi \ = \ 0.7\pi$ radians.

Figure 19 – Open- and closed-loop x_1 signal for initial condition 0.7π

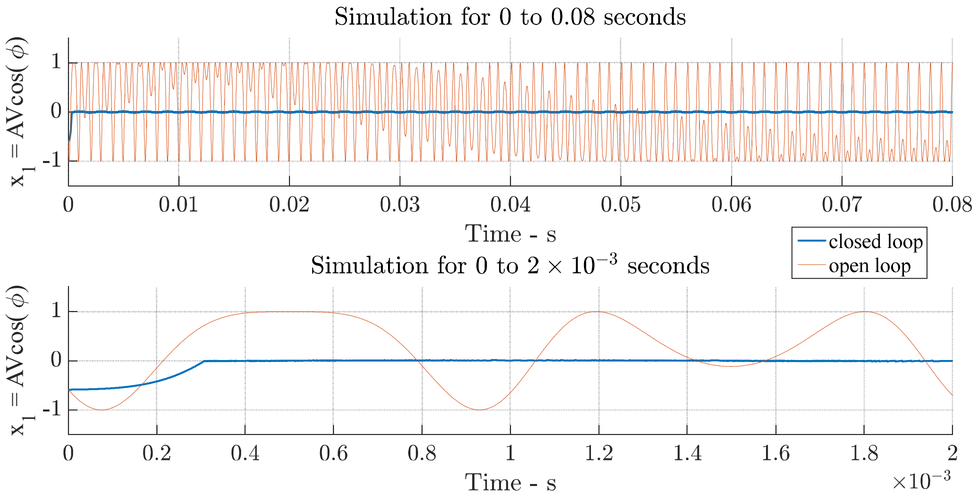

Source: elaborated by the author.

Figure 20 – Open- and closed-loop f signal for initial condition 0.7π

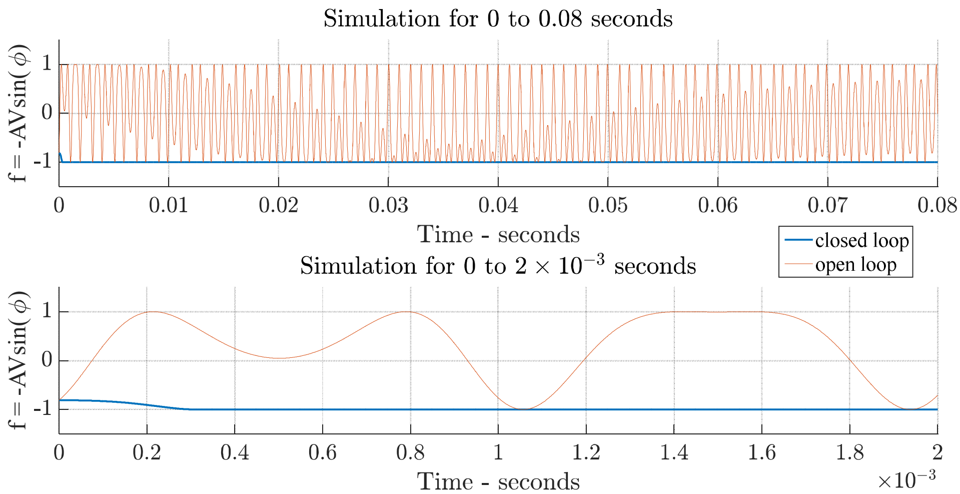

Source: elaborated by the author.

Also the comparison between the phase shifts $\phi_0 + \Delta\phi$ and the phase correction signal ϕ_c are shown in Figure 21, where it can be seen that the sum of both signals results in the approximately constant value of $\frac{\pi}{2}$. Therefore, the simulation agree with the stability analysis (see Figure 13), once that with the initial value of input phase equals to 0.7π the initial condition lies in the attraction region of the equilibrium point $\frac{\pi}{2}$.

Figure 21 - Input phases and closed-loop correction signal (ϕ_c) for initial condition 0.7π radians

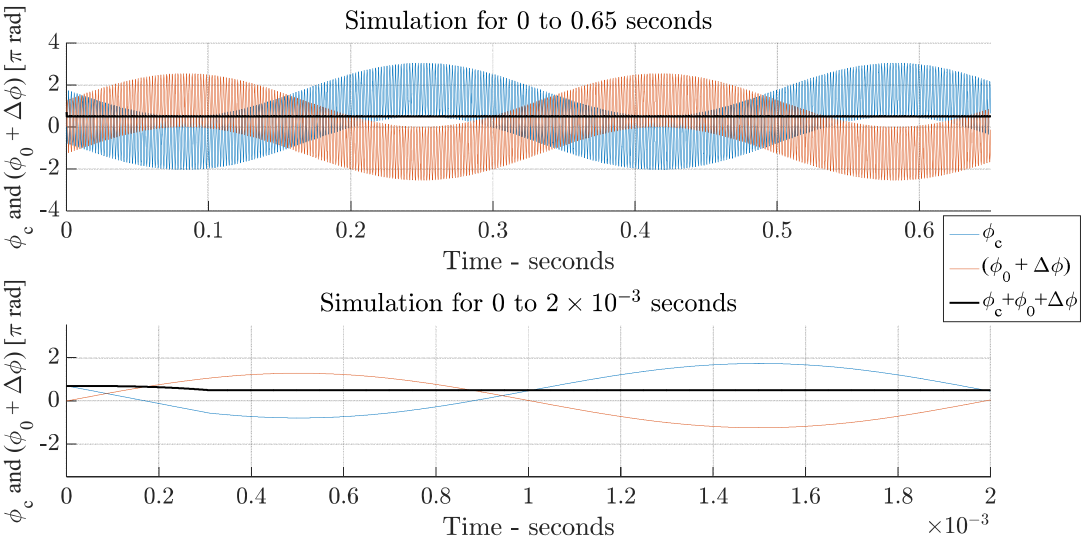

Source: elaborated by the author.

Repeating the simulations for the initial condition $\phi_c + \phi_0 + \Delta\phi = 1.0001\pi$ results in the convergence of the state trajectory to $x_1 \rightarrow 0$ and $f \rightarrow 1$ as can be seen in Figures 22, 23 and 24.

Figure 22 – Open- and closed-loop x_1 signal for initial condition 1.0001π

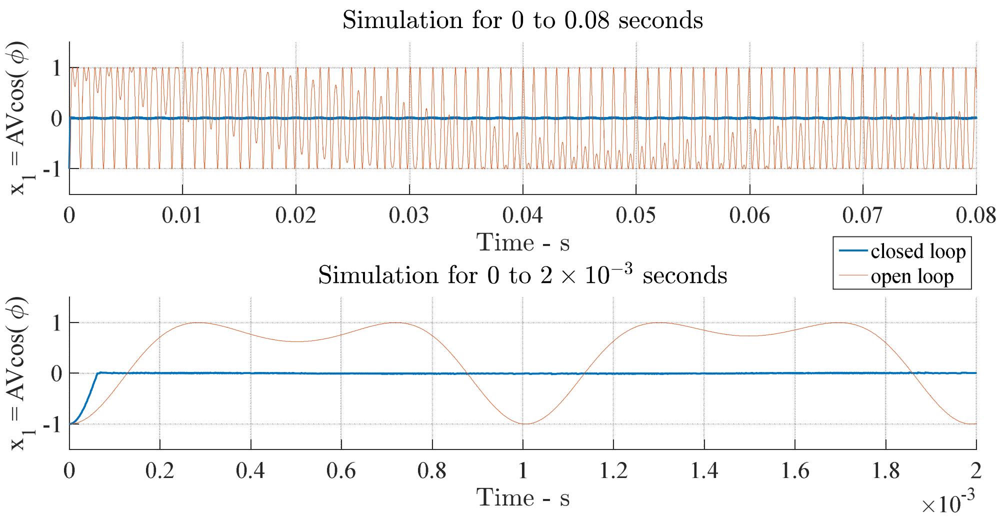

Source: elaborated by the author.

Figure 23 – Open- and closed-loop f signal for initial condition 1.0001π

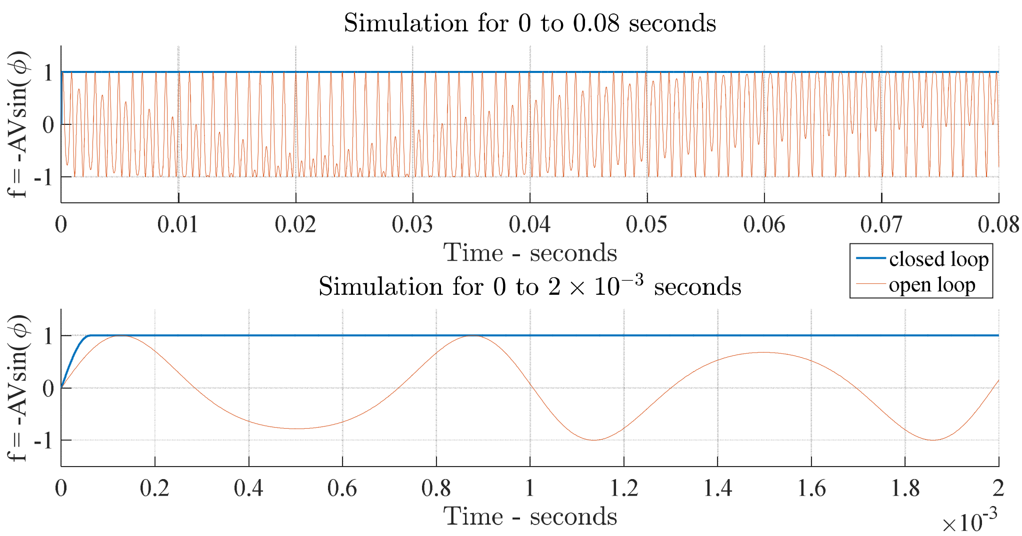

Source: elaborated by the author.

Figure 24 - Input phases and closed-loop correction signal (ϕ_c) for initial condition 1.0001π radians

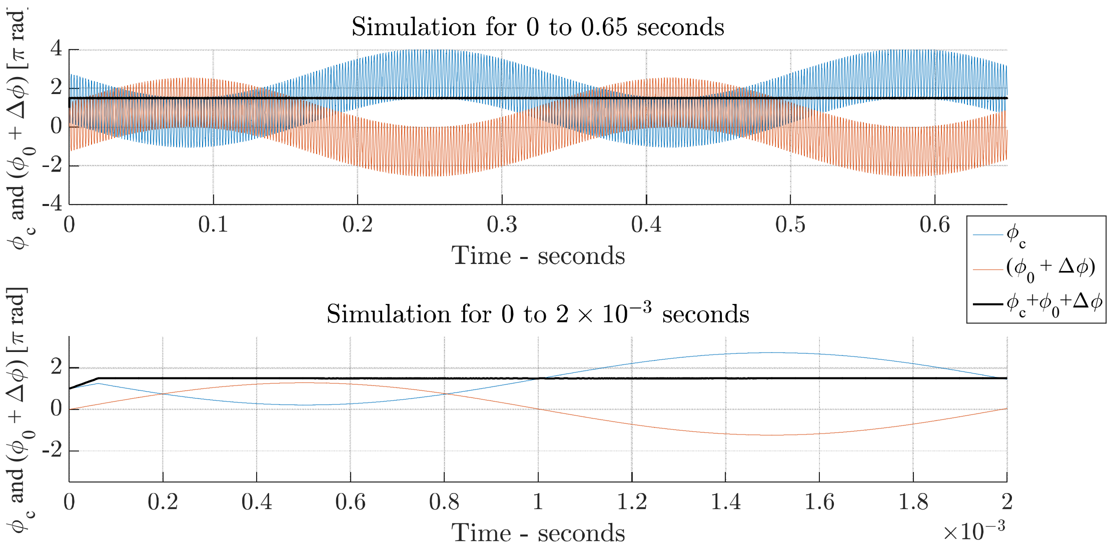

Source: elaborated by the author.

From the stability analysis, if the system is released from the initial condition $(\phi_c + \phi_0 + \Delta\phi) = 1.0001\pi$ radian, it should stabilize in the equilibrium point $(\phi_c + \phi_0 + \Delta\phi) = 1.5\pi$ radians (see Figure 13). As it can be seen in Figure 24, the behavior of the system agrees with the expected convergence.

3.4 Chattering Phenomenon

One drawback of sliding mode control is the so-called chattering phenomenon, which consists of an oscillation around the sliding surface. According to (YOUNG, UTKIN; OZGUNER, 1996), there are two main causes for this oscillation. First, we consider an ideal behavior for the actuators and therefore, the switching mechanism can work at infinite frequency. In this case, parasitic dynamics that were neglected can be excited, generating a small amplitude high frequency oscillation. In the second case, and most common, it is due to non-idealities on the actuator system, such as delay in the switching mechanism rising from the components non-idealities or from sampling periods, in the case of discrete-time processors controlling continuous-time systems.

The control system proposed in this work was implemented in discrete-time, therefore limiting the switching frequency of the control action accordingly to the used sampling period t_s. As mentioned before, this behavior can cause an oscillation of the state space trajectory around the sliding manifold, giving rise to a boundary layer whose thickness $\Delta(t_s)$ is a function of the sampling period. Using the methodology described in (SU; DRAKUNOV; ÖZGÜNER, 2000), it is possible to estimate the upper limit of $|\Delta(t_s)|$ by considering a zero-order holder for the control signal u and integrating the maximum value of the derivate of the sliding variable ($\dot{s}$) in the interval of one sampling period t_s, This last can be obtained from (73), (74) and (76):

$$|\dot{s}| = \left|f.\left(\dot{\phi}_0 + \Delta\dot{\phi} - Csign(x_1 f)\right)\right| \leq |f|(|\phi_0| + |\Delta\phi| + |Csign(x_1 f)|) \ , \qquad (145)$$

from which, with the help of (71), is shown that its maximum value is:

$$|\dot{s}|_{max} = A_1 V_1(|\phi_0| + |\Delta\phi| + C) \ . \qquad (146)$$

Considering now the behavior of the sampled control signal as a zero order holder, actuating in the system during one sampling period t_s, leads to:

$$s_{(k+1)t_s} \leq s_{(kt_s)} + \int_{kt_s}^{(k+1)t_s} A_1 V_1(|\phi_0| + |\Delta\phi| + C)d\tau \ . \qquad (147)$$

The case in which the trajectory of the system is in the vicinity of the sliding manifold, $s_{(kt_s)}$ can be considered zero, therefore, resulting in:

$$\Delta(t_s) = A_1V_1(|\phi_0| + |\Delta\phi| + C)t_s\,. \tag{148}$$

Closed-loop simulations were then performed, with the parameters $A_1V_1 = A_2V_2 = 1$, amplitudes of ϕ_0 and ϕ_c set to 1 radian peak and frequencies respectively set to 3 Hz and 500 Hz. The maximum amplitude peak to peak of the chattering oscillation ($A_{chatt_{pp}}$), in the total phase signal ($\phi_0 + \Delta\phi + \phi_c$), was calculated from equation (148) according to:

$$A_{chatt_{pp}} = A_1V_1 \cos\left\{\frac{[\max(\phi_c + \phi_0 + \Delta\phi) - \min(\phi_c + \phi_0 + \Delta\phi)\,]}{2} + \frac{\pi}{2}\right\}, \tag{149}$$

and the results are arranged in Tables 1 and 2, for different values of gain C and sampling period of $t_s = 10\ \mu$s and $t_s = 1\ \mu s$, respectively, while in the third column of the table, it is showed the theoretically maximum value of the thickness of the boundary layer $\Delta(t_s)$.

Table 1 - Simulated chattering compared with theoretical $\Delta(t_s)$ for t_s = 10 μs.

Gain C	$A_{chatt_{pp}}$	$\lvert\Delta(t_s)\rvert$
3160	0.0417	0.0632
3180	0.0420	0.0634
3200	0.0421	0.0636
4000	0.0449	0.0716
5000	0.0482	0.0816
6000	0.0489	0.0916
7000	0.0521	0.1016
8000	0.0581	0.1116
9000	0.0650	0.1216
10000	0.0717	0.1316
11000	0.0780	0.1416
12000	0.0844	0.1516
13000	0.0908	0.1616
14000	0.0971	0.1716
15000	0.1034	0.1816

Table 2 - Simulated chattering compared with theoretical $\Delta(t_s)$ for $t_s = 1$ μs.

Gain C	$A_{chatt_{pp}}$	$\Delta(t_s)$
3160	0.0042	0.0063
3180	0.0042	0.0063
3200	0.0042	0.0064
4000	0.0045	0.0072
5000	0.0048	0.0082
6000	0.0049	0.0092
7000	0.0052	0.0102
8000	0.0058	0.0112
9000	0.0065	0.0122
10000	0.0072	0.0132
11000	0.0078	0.0142
12000	0.0085	0.0152
13000	0.0091	0.0162
14000	0.0097	0.0172
15000	0.0104	0.0182

From the results summarized in Tables 1 and 2, one can conclude that the chattering of the sliding variable $s = x_1$ remained within the region defined by the boundary layer, for all simulated conditions. Also it can be seen that for a fixed sampling period, the minimum value of the gain C which guarantees the reachability criterion will result in the minimum amplitude of chattering. And, by the last, the amplitude of the chattering also decreases with the reduction of the sampling period.

To mitigate this problem, the most common approach is to define a boundary layer around the sliding manifold, presenting Δ width, within which the discontinuous control action is approximated by a piecewise linear or smooth function (YOUNG, UTKIN; OZGUNER, 1996). Therefore, outside the boundary layer, the reachability criterion guarantees the convergence of the state space trajectory to the 2Δ neighborhood of the sliding manifold; by the other hand, when the state space trajectory of the system lies inside the boundary layer, it presents arbitrary motion. This behavior is called quasi-sliding mode and happens in most cases of real-world implementations.

3.4.2 Sigmoidal approximation

In this implementation we used the following sigmoid approximation, based on previous works reported in literature (SLOTINE; SASTRY, 1983; SLOTINE; LI, 1991; ERTUGRUL *et al*., 1996; BURTON; ZINOBER, 1986):

$$sigm(x_1 f) = \frac{x_1 f}{|x_1 f| + \varepsilon} \ , \tag{150}$$

where ε is a small positive constant, responsible for the slope of the sigmoidal function around the origin. It is important to highlight that with smaller values of ε, closer will be the behavior of the sigmoid to the sign function.

According to Burton and Zinober (1986), the width of the boundary layer (Δ) of a control law using a sigmoidal function obeys the inequation $\Delta < \varepsilon$, where the control action can be rewritten as:

$$u = \begin{cases} -C\, sign(x_1\, f) & for \quad x_1 \geq \varepsilon \\ -C sigm(x_1\, f) & for \quad x_1 < \varepsilon \end{cases} . \tag{151}$$

In order to analyze the control action, considering the closed-loop system confined to the boundary layer, the control signal in equation (151) can be expanded in Taylor series, with relation to the term $\frac{|x_1 f|}{\varepsilon}$ as showed in (BURTON; ZINOBER, 1986):

$$u_{BL} = -C\frac{(x_1\, f)}{|x_1 f| + \varepsilon} = -\frac{C}{\varepsilon}\left\{\frac{1}{\frac{|x_1 f|}{\varepsilon} + 1}\right\} x_1 f \ , \tag{152}$$

or

$$u_{BL} = -\frac{C}{\varepsilon}\left\{\frac{|x_1 f|}{\varepsilon} + 1\right\}^{-1} x_1 f \quad , \tag{153}$$

leading to

$$u_{BL} = -\frac{C}{\varepsilon}\left\{1 - \frac{|x_1 f|}{\varepsilon} + \frac{2|x_1 f|^2}{2!\,\varepsilon} + \cdots\right\} x_1 f \quad . \tag{154}$$

Considering now that within the boundary layer the oscillations around the equilibrium points are small, the higher order terms can be disregarded in a qualitative analysis, resulting in:

$$u_{BL} = -\frac{C}{\varepsilon} x_1 f \quad , \tag{155}$$

therefore substituting equation (155) in (74), leads to:

$$\dot{x}_1 = (\dot{\phi}_0 + \Delta\dot{\phi}) f - \frac{C}{\varepsilon} x_1 f^2 \quad , \tag{156}$$

It is important now, to highlight two main ideas: first, the function $f = -A_1 V_1 \sin(\phi_c + \phi_0 + \Delta\phi)$ in (71) can be approximated to $-A_1 V_1$ or $+A_1 V_1$, for the system lying respectively around the equilibrium points $\left\{ \phi_c^* = \frac{\pi}{2} + 2k\pi \mid k \in \mathbb{Z} \right\}$ or $\left\{ \phi_c^* = -\frac{\pi}{2} + 2k\pi \mid k \in \mathbb{Z} \right\}$; and second, the equation (156) is now a linear dynamic equation with respect to the state space variable x_1. Therefore, let us apply the Laplace transform in equation (156) considering both cases of stable equilibrium points:

a) For $\phi_c^* = \frac{\pi}{2} + 2k\pi$:

$$\begin{gathered} \dot{x}_1 = -(\dot{\phi}_0 + \Delta\dot{\phi}) A_1 V_1 - \frac{C}{\varepsilon} x_1 (A_1 V_1)^2 \overset{\mathcal{L}\{\dot{x}_1\}}{\Longleftrightarrow} \\ s X_1 = -s A_1 V_1 (\Phi_0 + \Delta\Phi) - \frac{C}{\varepsilon} X_1 (A_1 V_1)^2 \quad , \end{gathered} \tag{157}$$

where $X_1 = \mathcal{L}\{x_1\}$, $\Phi_0 = \mathcal{L}\{\phi_0\}$ and $\Delta\Phi = \mathcal{L}\{\Delta\phi\}$, and so:

$$X_1 = -\frac{s(\Phi_0 + \Delta\Phi) A_1 V_1}{\left[s + \frac{C}{\varepsilon} (A_1 V_1)^2 \right]} . \tag{158}$$

b) For $\phi_c^* = -\frac{\pi}{2} + 2k\pi$:

$$\begin{gathered} \dot{x}_1 = (\dot{\phi}_0 + \Delta\dot{\phi}) A_1 V_1 - \frac{C}{\varepsilon} x_1 (A_1 V_1)^2 \overset{\mathcal{L}\{\dot{x}_1\}}{\Longleftrightarrow} \\ s X_1 = s (\Phi_0 + \Delta\Phi) A_1 V_1 - \frac{C}{\varepsilon} X_1 (A_1 V_1)^2 \quad , \end{gathered} \tag{159}$$

and so

$$X_1 = \frac{s(\Phi_0 + \Delta\Phi) A_1 V_1}{\left[s + \frac{C}{\varepsilon} (A_1 V_1)^2 \right]} . \tag{160}$$

One can see that the poles of the transfer function on both cases are located on the left half of the complex plan, characterizing a stable system.

Next, will be studied the behavior of the chattering amplitude of the system with sigmoidal function, as well as the influence of its parameter ε on the maximum amplitude of the chattering, depending on several values of the gain C. Thereby another model of the closed-loop system was assembled on Simulink, substituting the sign block in Figure 14 by the sigmoidal function. The resulting maximum amplitudes of the phase errors between ϕ_c and $\Delta\phi + \phi_0$ for sampling periods $t_s = 10\,\mu$s and $t_s = 1\,\mu$s, with $\varepsilon = 0.01$, are shown in Table 3.

Table 3 - Maximum amplitude of the phase error between $\boldsymbol{\phi_c}$ and $\boldsymbol{\Delta\phi + \phi_0}$ in degrees for $\boldsymbol{u = -Csigm(x_1\, f)}$, with ϵ=0.01.

Gain C	$t_s = 10\ \mu s$	$t_s = 1\ \mu s$
3160	13.1254	13.1252
3180	12.7114	12.7137
3200	12.3123	12.3153
4000	4.1364	4.1370
5000	1.9634	1.9636
6000	2.0236	1.2748
7000	2.7449	0.9431
8000	3.7369	0.7483
9000	4.6006	0.6202
10000	5.0846	0.5295
11000	4.9599	0.4620
12000	5.5224	0.4097
13000	5.9513	0.3681
14000	6.2453	0.3341
15000	6.4048	0.3059

The data obtained, using the sigmoidal function, showed a different behavior from that using the sign function. For the sampling period of 10 μs, as the gain increases, the value of error amplitude decreased until the minimum value of 1.9634 degrees at the gain of 5000 and, for higher gains, the error amplitude rises. On the other hand, for the sampling period of 1 μs, as the gain increased, the error amplitude decreased for the simulated values.

3.4.3 Simulated phase planes

The closed-loop interferometric system has only one first order differential equation that governs its dynamic, and therefore is a first order system. Its behavior was also studied using the phase plan, simulated using the numerical method Runge-Kutta in the function “ode45” of the software Matlab. In Figure 24, the phase plane was obtained for high gain, making $C = 20000$, in order to test if the system goes to instability, while in Figure 25 the gain of the system was configured as $C = 1000$, and the phase plane showed in Figure 26 was obtained with the gain $C = 200$. In all these simulations, the parameter A_1V_1 is equal to the unity.

Figure 25 - Simulated phase plane with gain 20000 and initial phases – 2π and π

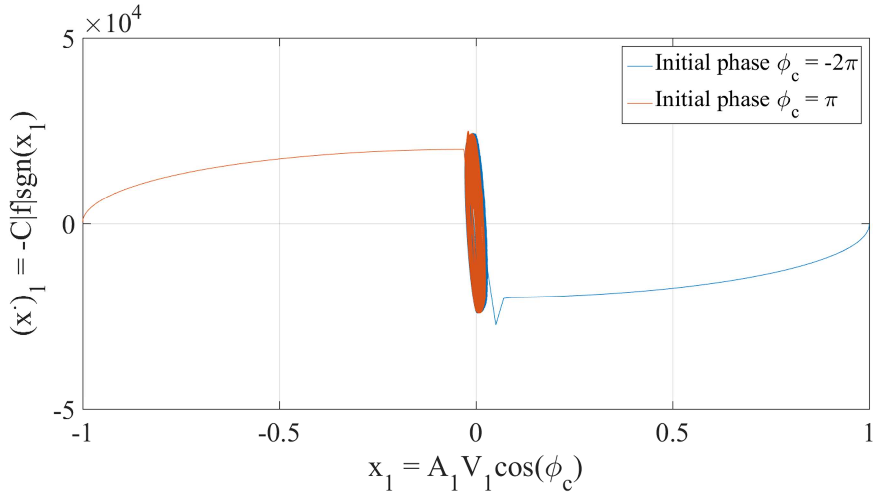

Source: elaborated by the author.

Figure 26 - Simulated phase plane with gain 1000 and initial phases –2π and π

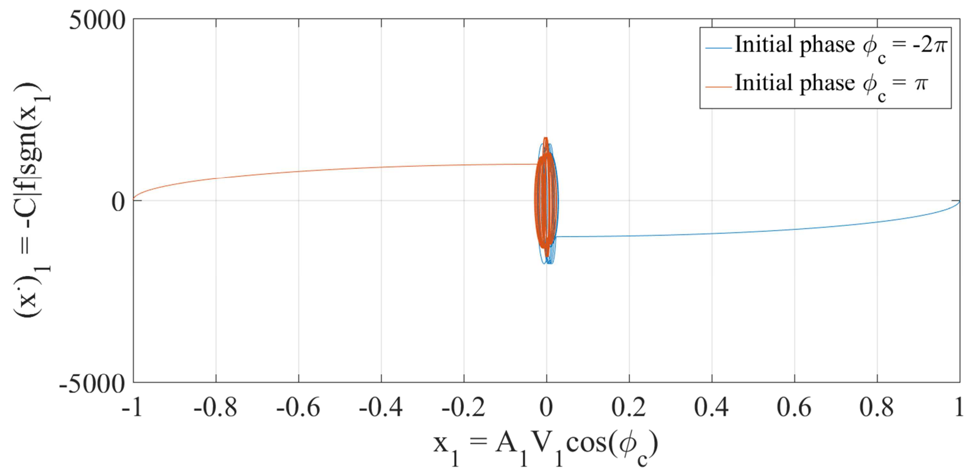

Source: elaborated by the author.

Figure 27 - Simulated phase plane with gain 200 and initial phases –2π and π

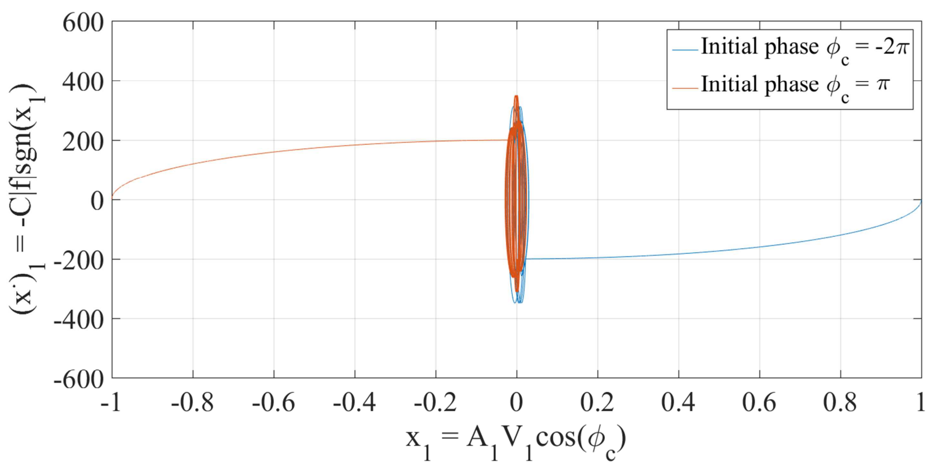

Source: elaborated by the author.

From the phase plans, it is noted the global behavior of the system, once the state variable x_1 has its values lying within [-1,1], for any value of initial phase ϕ_c , the system trajectory always goes to the origin and oscillates around it. It is important to remember that $\dot{x}_1$ is given by equation (91), and therefore the overall gain C is multiplying the sign function and the absolute value of the function f, causing the high values on $\dot{x}_1$ axis. However the output signal $x_1 = A_1V_1\cos(\phi)$ oscillates in small values around the origin, showing that the interferometer is operating in one of its quadrature points and corroborating with the simulation results aforementioned.

The simulation results showed the capacity of the system to operate using the high gain approach, giving important insights about the influence of parameters, such as, the sampling period, overall gain and modifier parameter of the sigmoidal function.

3.5 Equivalent system virtually controlled

Starting from the main idea of the control system explained in the Section 3.1, a new concept of phase demodulation method was designed. In order to understand this concept the reader should refer to Figure 11, where it is shown the closed-loop system block diagram. One can note that the output signals of the quadrature interferometer are given by equations (37) and (38). By withdrawing the DC levels of $v_1(t)$ and $v_2(t)$ the signals v_{ac1} and v_{ac2} are obtained (in Section 3.1), respectively. Besides, as (37) and (38) refer to the open-loop interferometer, the phase shift ϕ_c is added to the argument of the cosine and sine functions ($\phi = \phi_c + \Delta\phi + \phi_0$) for the closed-loop interferometer.

Multiplying the output signal v_{ac2} by the parameter $r = \frac{A_1V_1}{A_2V_2}$ and using the relationship of sum of arcs, these equations can be rewritten as:

$$v_{ac_1} = A_1V_1[\cos(\phi_c)\cos(\Delta\phi + \phi_0) - \sin(\phi_c)\sin(\Delta\phi + \phi_0)] \ , \qquad (161)$$

and

$$v_{ac_2} = -A_1V_1[\sin(\phi_c)\cos(\Delta\phi + \phi_0) + \sin(\Delta\phi + \phi_0)\cos(\phi_c)]. \qquad (162)$$

From this result, the block diagram of the conventional closed-loop system can be expanded into the equivalent form shown in Figure 28.

Figure 28 - Equivalent system virtually controlled

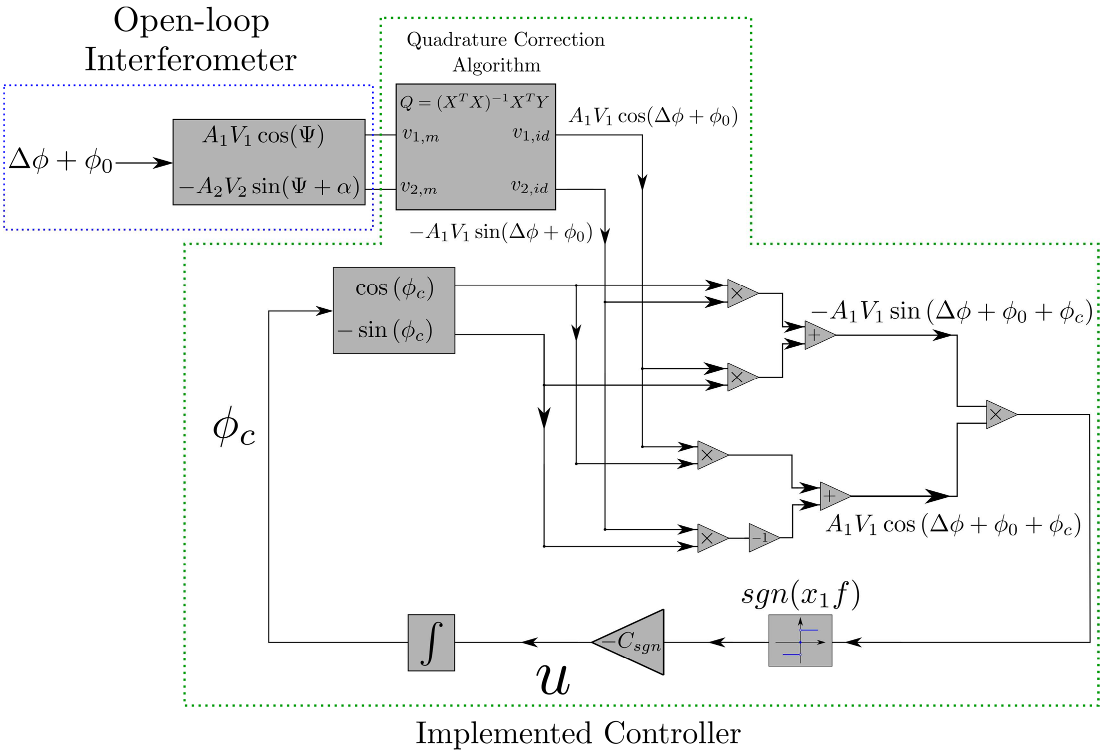

Source:elaborated by the author.

It is noteworthy that the system, highlighted by the blue dotted line, is the open-loop real quadrature interferometer, which provides the signals v_{ac1} and v_{ac2}, while the green dotted line system comprises the quadrature correction algorithm and digitally implemented dynamic system, that operates in closed-loop to calculate the phase correction signal ϕ_c. Therefore the optical interferometer (the hardware) can operate in open-loop while the correction signal ϕ_c is calculated in the chosen digital platform. This procedure obtains the signal $\phi_c = -\Delta\phi - \phi_0$ directly in radians, thereby constituting a primary standard for linear displacement measurement. In this way, there is no need for a feedback PZT in the reference arm, simplifying the hardware needed for the system. Also the overall gain of the feedback system is now limited only by the word length of fixed-point used in the FPGA implementation, and not by the linear voltage amplifier output and feedback PZT in the reference arm. The stability analysis and behavior of the control system performed in the previous subsections is also valid for the equivalent virtually controlled system. But in order to prove such statement, the equivalent virtually controlled system was assembled in software Multisim, as showed in Figure 29, and simulations in closed-loop were performed, using the same parameter configuration as in previous section. Therefore, in Figure 30 it can be seen the same results for the state variable x_1 for different sampling periods, $t_s = 10^{-4}$, 10^{-5} and 10^{-6} s.

Figure 29 - Simulation of the equivalent system virtually controlled

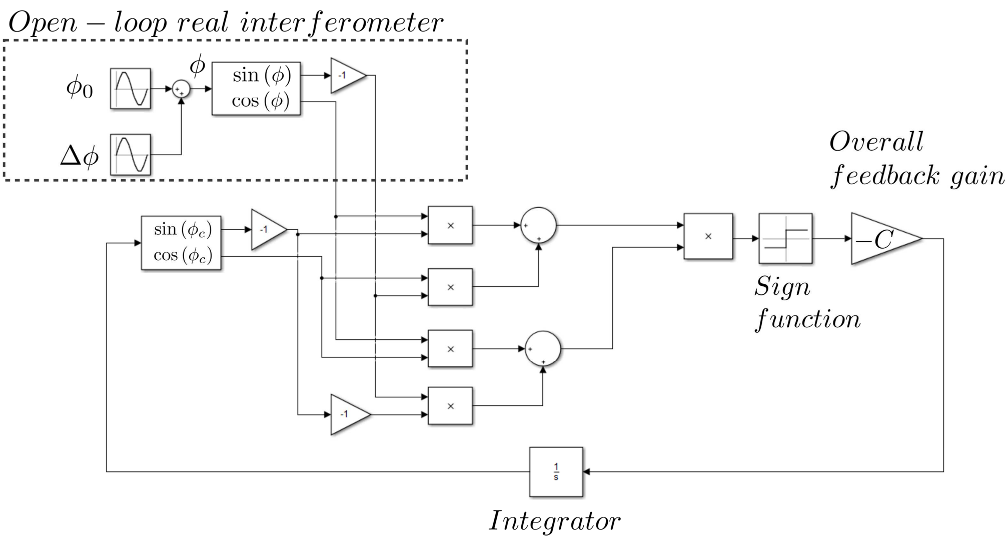

Source: (elaborated by the author).

Figure 30 - Simulated equivalent interferometer signal x_1 for different sampling periods (t_s)

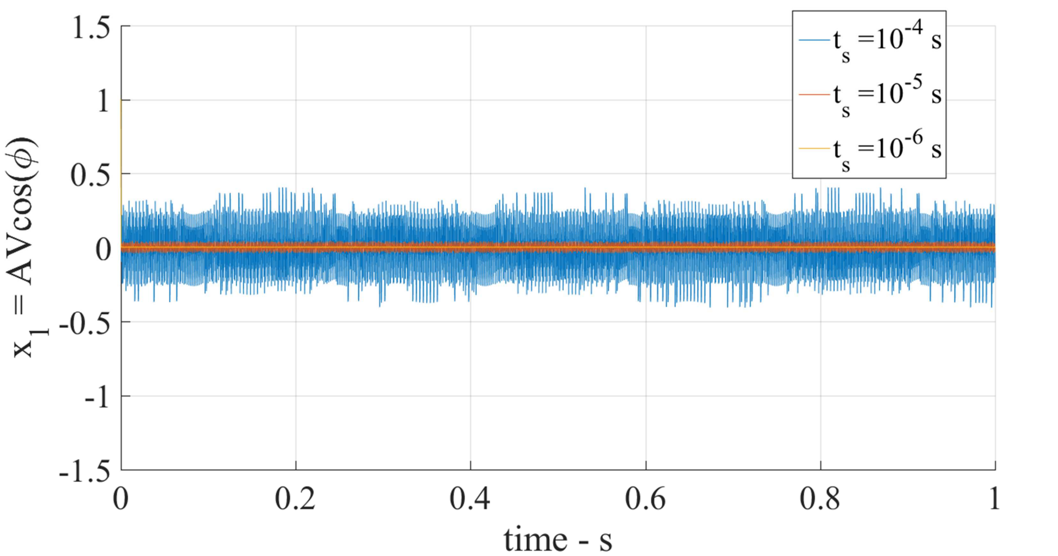

Source: (elaborated by the author).

Simulations were also performed in order to analyze the convergence to different stable equilibrium points, and again, it can be observed the same behavior as the control system discussed in Section 3.1, where for the initial condition chosen as $\phi_c + \phi_0 + \Delta\phi = 0.7\pi$; the results of Figures 31, 32 and 33 shows that the system converges to the equilibrium point $\phi_c + \phi_0 + \Delta\phi = \frac{\pi}{2}$;

Figure 31 – Open- and closed-loop x_1 signal of the equivalent system, for initial condition 0.7π

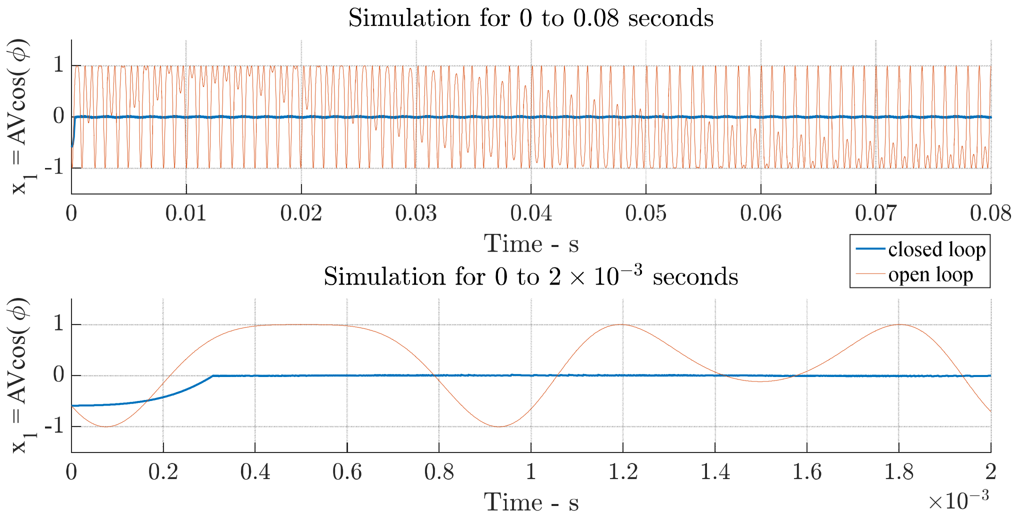

Source: elaborated by the author.

Figure 32 – Open- and closed-loop f signal of the equivalent system, for initial condition 0.7π

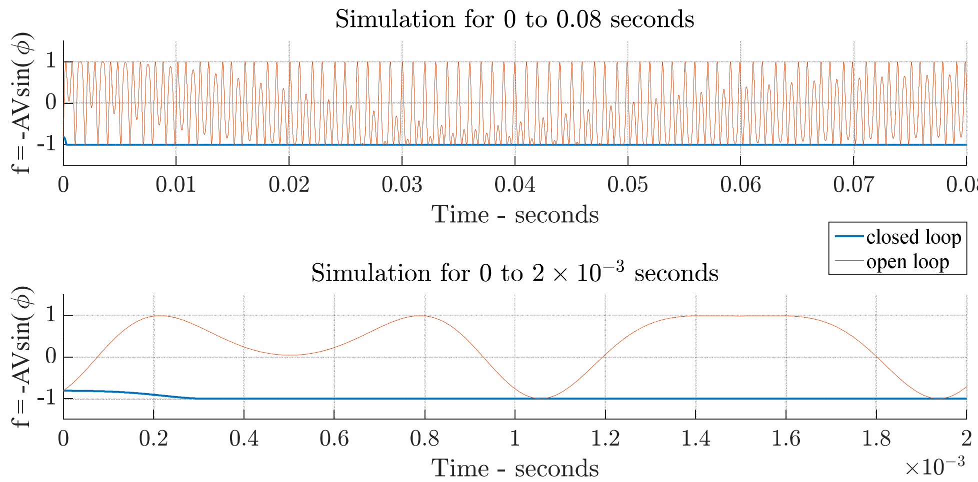

Source: elaborated by the author.

Figure 33 - Input phases and closed-loop correction signal (ϕ_c) of the equivalent system, for initial condition 0.7π radians

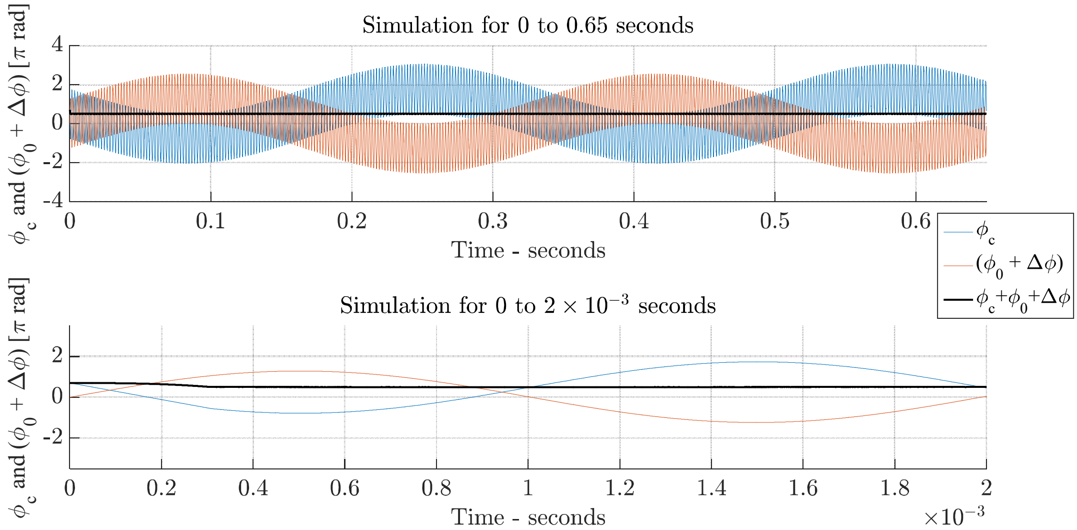

Source: elaborated by the author.

Changing the initial condition to $\phi_c + \phi_0 + \Delta\phi = 1.0001\pi$ results in the convergence of the state trajectory to $x_1 \to 0$, $f \to 1$ and $\phi_c + \phi_0 + \Delta\phi \to \frac{3\pi}{2}$, as it can be seen in Figures 34, 35 and 36.

Figure 34 – Open- and closed-loop x_1 signal of equivalent system, for initial condition 1.0001π

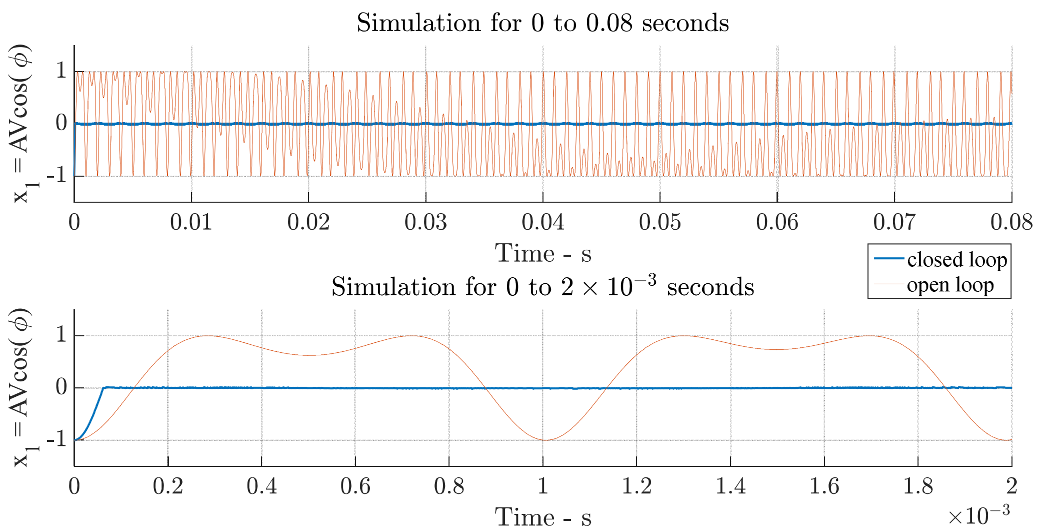

Source: elaborated by the author.

Figure 35 – Open- and closed-loop f signal of equivalent system, for initial condition 1.0001π

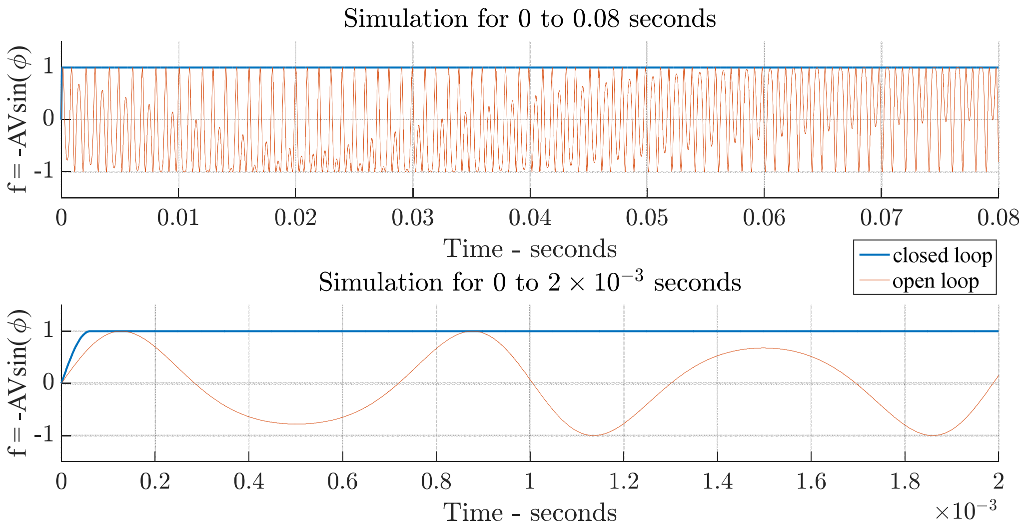

Source: elaborated by the author.

Figure 36 - Input phases and closed-loop correction signal (ϕ_c) of the equivalent system, for initial condition 1.0001π radians

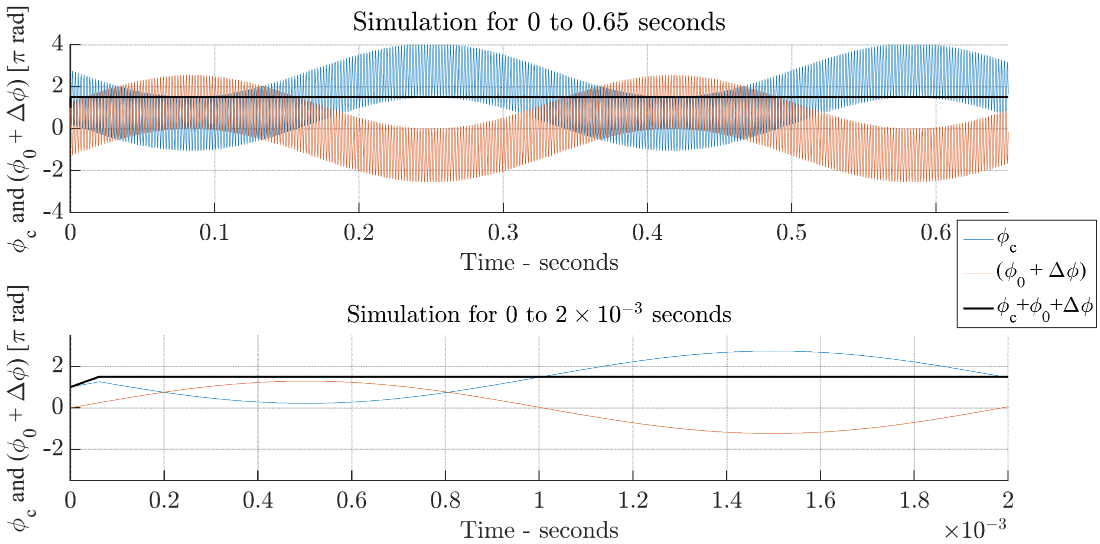

Source 1: elaborated by the author.

In view of the above, it can be seen that the proposed control system and the expanded system, which is virtually controlled, are equivalent and both can be used to measure the phase shifts, induced on interferometers.

3.6 Post processing algorithm

As it will be seen in Chapter 4 – Results, the equivalent system virtually controlled (ES) was able to measure phase shifts in high modulation depth in frequencies up to 500 Hz. However for some applications there is a need to operate at higher frequencies. Aiming to allow such applications, a post processing routine was developed in MatLab and used to demodulate interferometric phase from photodetected data sampled with the oscilloscope.

This processing routine was compared with the method proposed by (LEMES, 2014) in order to evaluate the correct operation of the control algorithm for phase demodulation. It is noteworthy that both algorithms use the procedure for quadrature correction described on Chapter 2, Section 2.4 as idealized by Heydemann (1981).

4 Experimental setup and results

This chapter is dedicated to explain the aspects of the system implementation, used simplifications and experimental procedures that were carried out in this work. The chapter is subdivided in the assembly of the modified Michelson interferometer, implementation of the control system, tests for validation and characterization of the control system, implementation of the equivalent system virtually controlled, implementation of the quadrature correction algorithm and lastly, tests are presented comparing the control system with the equivalent system.

4.1 Assembly of the modified Michelson interferometer

The objective of this step was to assembly and carry out the alignment of the modified Michelson interferometer, which the block diagram is shown in Figure 06. This allows the obtaining of the signals $x_1 = A_1V_1\cos(\Delta\phi + \phi_0 + \phi_c)$ and $f = -A_1V_1 sin(\Delta\phi + \phi_0 + \phi_c)$ ((69) and (71), respectively) necessary to implement the control system.

Firstly the interferometer was assembled as shown in Figure 37, comprising the following components:

1- He-Ne (Helium-Neon) laser operating in 632.8 nm with 5 mW of power (Electro Optics model LHRP-0501) ;

2 – Negative lens;

3 – Beam splitter CMI-BS013;

4 – Feedback PZT actuator (APF CA92630);

5 – Second beam splitter;

6 – Quadratic law silicon based photodetectors model DET36A (Thorlabs);

7 – Quadratic law silicon based photodetector model DET10A (Thorlabs);

8 – Mirror.

Figure 37- Top view of the modified Michelson interferometer

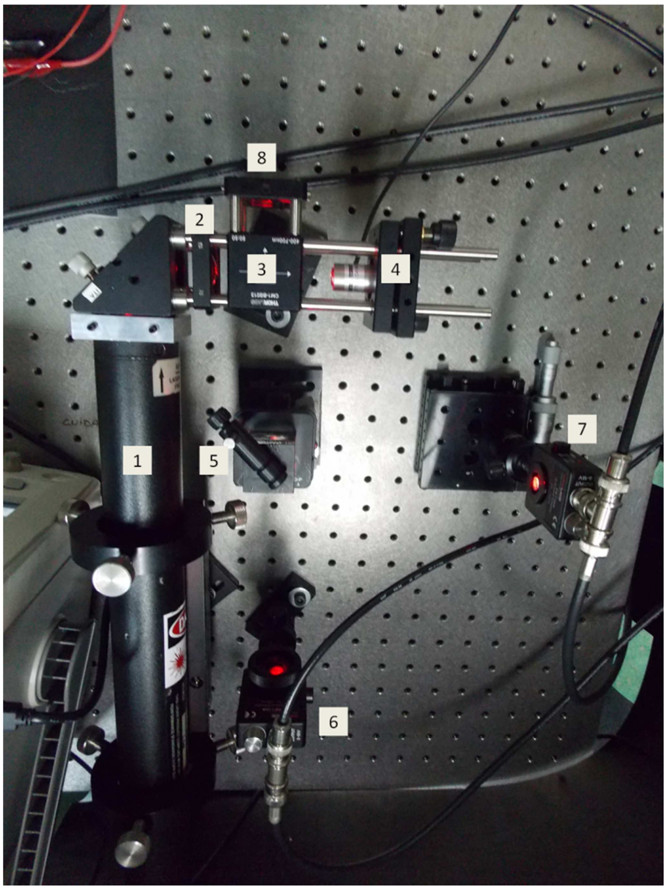

Source: elaborated by the author.

After the assembling of the interferometer, the system was aligned, in such a way that the fringe patterns become as closer as possible to concentric circles. The photodetector indicated by the number 6 in Figure 37 was positioned at the center of the first fringe pattern and fixed in this position. The incident intensity in photodetector 6 was adjusted with the aid of an iris, so that the photodetected signal would not saturate or become too small. The output signals of the photodetectors 6 and 7 were then connected to the oscilloscope (Agilent, model MSO6034A), in the acquisition mode XY and a sinusoidal voltage signal was applied to the PZT actuator 4, allowing the visualization of the Lissajous figure.

The photodetector indicated by 7 in Figure 37 was assembled on a translational stage base positioner with micrometer resolution, and then was positioned also at the center of the other fringe pattern, in such a way the Lissajous figure becomes a straight line, indicating that both photodetected signals were in phase. After, by displacing the photodetector, the relative phase difference changes and the Lissajous figure becomes an inclined ellipse. When the phase difference is adjusted to $\frac{\pi}{2}$ rad, the Lissajous figure becomes an ellipse with the major diagonal and minor diagonal aligned with the X and Y oscilloscope screen axes. Then the amplitude of the photodetected signals can be fitted to approximately the same value, through the adjustment of the iris aperture in 6. In Figure 38 is shown the Lissajous figure for the aligned modified Michelson interferometer with quadrature adjustment, which becomes approximately a circle.

Figure 38 - Lissajous figure of the quadrature interferometer

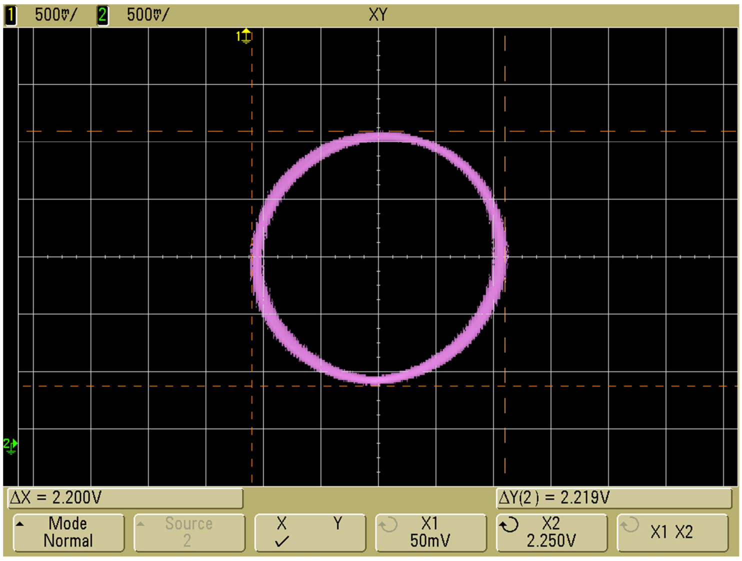

Source: elaborated by the author.

The yellow and green signals, showed in Figure 39 and 40, are respectively from photodetectors 6 and 7, while the purple signal is the applied voltage to the PZT actuator 4.

Figure 39 - Applied voltage to PZT and output signals of the interferometer

Source: elaborated by the author.

In order to verify the quadrature adjustment, the applied voltage to PZT actuator was decreased to low phase modulation index regime, and it was observed that when one of the photodetected signals are operating at quadrature point, the another is operating at one point of maximum or minimum of the interferometer curve. Therefore presenting a signal with attenuated amplitude and twice the frequency of the PZT actuator applied voltage. The output signals and voltage applied to the PZT actuator are shown in Figure 40.

Figure 40 - Output signals with phase difference of $\frac{\pi}{2}$ radians and applied voltage to PZT

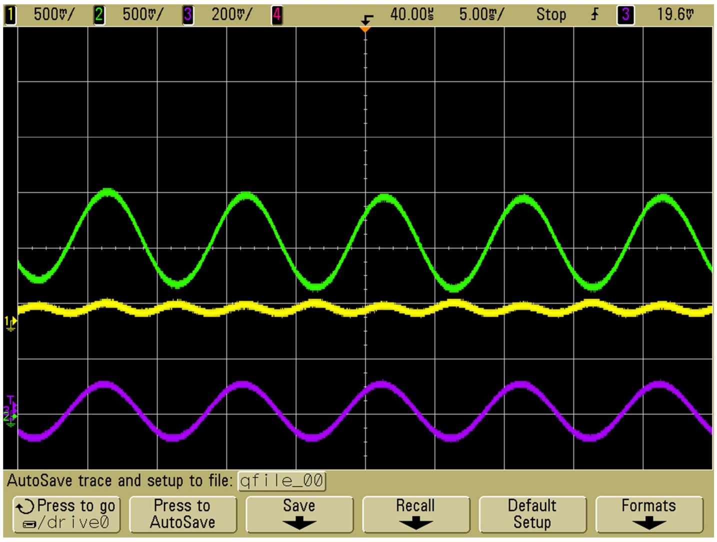

Source: elaborated by the author.

After this procedure the output signals needed by the control law $x_1 = A_1 V_1 \cos(\Delta\phi + \phi_0 + \phi_c)$ and $f = -A_1 V_1 \sin(\Delta\phi + \phi_0 + \phi_c)$ were obtained with success, therefore, the next stage was to implement the control system.

4.2 Implementation of the control system

The previous stage provided the interferometer output signals, with the phase difference of $\frac{\pi}{2}$ rad, comprising thus, the block with cosine and sine outputs in the block diagram of Figure 10. In order to implement the control law given by equation (81), it is necessary to acquire both output signals x_1 and f, perform their multiplication and apply the sign function. The result then, must be multiplied by the appropriate gain, integrated for generating the voltage v_{out} and lastly, applied it to the voltage amplifier that drives the feedback control PZT. This closes the feedback control loop as it can be seen in Figure 41.

As will be discussed later, the shaded region in Figure 41 was embedded within a digital platform comprising two analog inputs (v_1 and v_2), two subtractors, a multiplier, the sign function, an inverter amplifier and an integrator. The voltage v_{out} corresponds to an analog output which will constitute the output signal for the high gain approached interferometer.

Figure 41 – Closed-loop control system block diagram

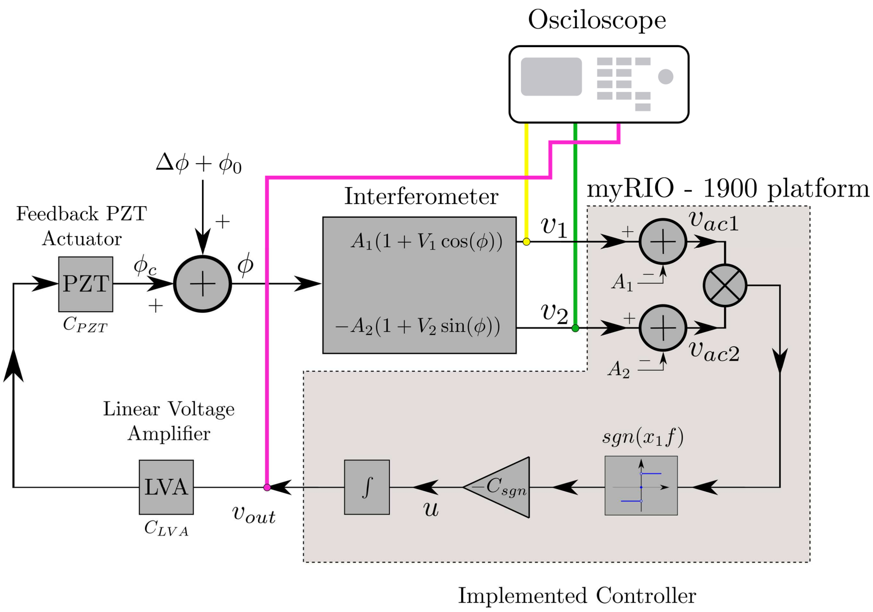

Source: elaborated by the author.

It can be seen in the implemented system of Figure 41, that the overall gain "C" is subdivided into three gains, the gain of the signal function C_{sgn}, the gain C_{LVA} of the linear voltage amplifier (LVA) and the gain of the feedback PZT actuator C_{PZT}, resulting in:

$$C = C_{sgn} C_{LVA} C_{PZT} \, , \tag{163}$$

where the gain C_{sgn} can be digitally configured. The gain C_{LVA} of the amplifier is approximately $21 \, V/V$ and the gain C_{PZT} of the feedback PZT, measured in rad/V, is a function of the frequency. Therefore this actuator must be previously characterized, as it will be explained further in section 4.3.

Digital controllers are capable of performing complex computations at high speed with constant accuracy. Besides that, they present more flexibility, since changes can be made in the implemented system, without rearranging the hardware, which allows the implementation of more complex functions. This type of controller is often implemented in microcontrollers, Digital Signal Processors (DSP) and Field Programmable Gate Arrays (FPGA).

To implement the proposed nonlinear control system, we have chosen myRIO-1900 (National Instruments), which contains a Xilinx Zynq-7010, comprising a Real-Time Dual Core Arm cortex A9 processor and a FPGA. It is noteworthy that LabVIEW Toolkit for programming and deployment of the FPGA device allows the hardware design to be carried out without prior knowledge of Hardware Description Language (HDL).

This Section gives a brief explanation about the functions comprising the nonlinear control system and the synchronization of the real-time processor algorithm with the hardware which were implemented in FPGA. The hardware block diagram of the chosen platform is shown in Figure 42 (National instruments, 2017). One can see that the analog inputs and outputs are connected directly to the FPGA, which means that, compared with the real-time processor's performance, this configuration provides a higher sampling rate and is able to execute different tasks concurrently.

Figure 42 - Hardware block diagram of myRIO-1900 embedded plataform

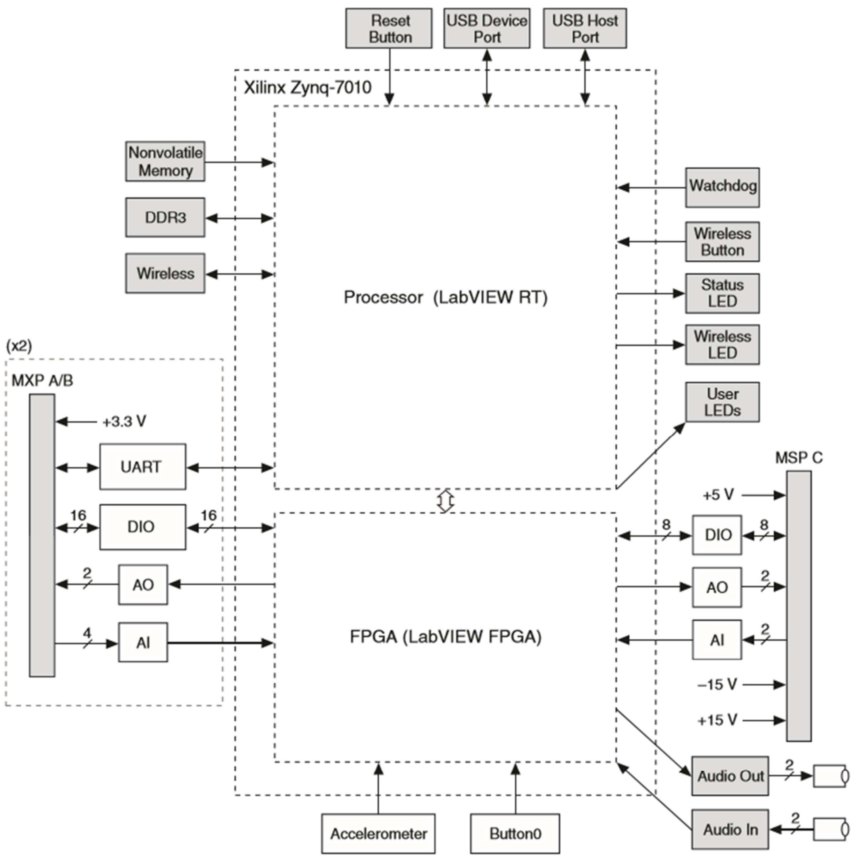

Source: (National Instruments)

As showed by the simulation results of Section 3.3, it is recommended to use high sampling frequencies in the control system, therefore the output signals v_1 and v_2 of the photodetectors were firstly sampled at 100 kHz by the analog inputs, using a voltage resolution of 4.883 mV. The DC levels A_1 and A_2 are experimentally determined by $A_1 = \frac{\left[v_{1_{max}} + v_{1_{min}}\right]}{2}$ and $A_2 = \frac{\left[v_{2_{max}} + v_{2_{min}}\right]}{2}$, as described in (XU et. al., 2010) where the maximum and minimum values of v_1 and v_2 are measured with the interferometer operating in open-loop and with an induced phase shift, large enough to operate multi-fringe mode. Following the Figure 41, these two values are then suppressed from the sampled signals, originating $v_{ac1} = x_1$ and $f = \frac{A_1 V_1}{A_2 V_2} v_{ac2}$, according to (69) and (75) respectively.

Both signals are then multiplied, and the sign function $sgn(x_1 f)$ is approximated by the sigmoidal function, calculated as (150), that is:

$$sigm(x_1 f) = \frac{x_1 f}{|x_1 f| + \epsilon}, \tag{164}$$

The sigm function is multiplied by the gain $-C_{sgn}$ and applied to the input of the digital integrator shown in Figure 41.

In case of arbitrary signals, since there is not an anti-derivative in terms of known functions, we use methods which approximate the finite integral. Two of the most popular methods for approximating the evaluation of definite integrals are the Trapezoidal and Simpson's Rules (ALAOUI; MOHAMAD, 1993; DAVIS; RABINOWITZ, 2007).

We employed the Simpson's rule to the integrator, which was implemented in FPGA for the nonlinear control system. This method approximates a definite integral by using quadratic polynomials instead of straight lines segments used in the trapezoidal rule. The implemented integrator is explained in more detail in (MARTIN, 2018).

When the actuator, responsible to apply the control signal, reaches the saturation level, the feedback loop does not act properly and the calculated values of the regulator may then drift to undesirable values. This phenomenon is referred to as windup.

According to (TARBOURIECH; TURNER, 2008), the first academic work published regarding the problem of saturation in control systems was (LOZIER, 1956), highlighting that this type of system may present two different behaviors: one dictated by the original differential equation of the system model, and another one due to a saturated mode, which could originate premature saturation, hysteresis in the input-output relationship, jump resonance and other anomalous effects, denigrating the steady state performance.

Many authors described this problem and proposed ways to overcome it (BERGER; GUTMAN, 2015; TURNER; SOFRONY; HERRMANN, 2016; KAPOOR; TEEL; DAOUTIDIS, 1998; PENG; VRANCIC; HANUS, 1996; ZHENG; KOTHARE; MORARI, 1994; RAN; WANG; DONG, 2016; ASTROM; RUNDQWIST, 1989), mainly based on two approaches: the first one handle the saturation on the design of the control law, ensuring the nominal performance specifications, while the second separates the controller in two, one for the original system without considering saturation and the other is the anti-windup compensation.

The output of myRIO-1900 embedded platform (v_{out} in Figure 42) is limited in the range of ± 10 V. Therefore, considering the interferometer subjected to a phase shift high enough to make the analog output to lie out of this range, the integrator would keep increasing the internally calculated value. Meanwhile the output value would stay fixed in the saturation level and, after the end of disturbance; it would take a long time for the integrator output reaches again values in the range of the analog output. A simple way to avoid such problem is to stop the integration when the calculated value is out of the analog output voltage range and return to normal operation when the result lies within ± 10 V. Therefore, a structure comprising a case condition loop was implemented in cascade with Simpson integrator, preventing windup phenomenon. It is noteworthy that the controller does not need a reset system as those used by (FRITSCH; ADAMOWISKY, 1981; BASILE *et al*., 1991) to name a few. After the integrator with anti-windup, the signal is converted to a voltage signal by one analog output in the range of ± 10 V. This signal is then applied to the analog voltage amplifier, which multiplies the input signal by 21 V/V and drives the PZT feedback actuator, inducing the phase correction signal ϕ_c, closing the control loop.

In order to log the acquired data of control signal and photodetector output signal from the FPGA, data must be transferred to the real-time processor. A recommended approach to transfer a large amount of sequential data is through a Target to Host FIFO (First-In First-Out). The details of the configuration of the FIFO and its use in the transfer of the sampled data can be found in (MARTIN, 2018).

With the assembled control law and data log system, tests were performed in order to evaluate the implemented system.

4.3 Tests for validation and characterization of the control system

This Section shows the procedures used and tests performed to evaluate the closed-loop control system operating in high gain approach.

It is important to highlight that in order to estimate the phase shift using the high gain approach, the gain of the PZT actuator on the feedback loop (C_{PZT} in Figure 40) must be known, because the measurement is carried out using the control voltage v_{out}, which is then multiplied by the gain C_{LVA} of the linear voltage amplifier and lastly, applied to this PZT. On the other hand, this approach does not require the periodic estimation of the AV factor in (69) or (75) to guarantee the accuracy of the system (UDD; SPILMANN, 2011), representing thus, a tradeoff of this approach.

After the implementation of the control law, the system was tested in the assembly shown in Figure 37, where, in open-loop, the interferometer was disturbed in low frequencies, by exerting pressure on the mirror indicated by the number 8. The disturbance level was high enough to shift several fringes in the interferometric curve and during this procedure, the control system was turned on, stabilizing the output x_1 of the interferometer at zero and, therefore, rejecting any induced disturbance.

In Figure 43 it is presented the acquisition data of the oscilloscope during the test, where channel 1 (yellow signal) is the x_1 output, channel 2 (green signal) is the f output of the interferometer and the purple signal in channel 3 is the voltage control signal v_{out} (see Figure 41) applied to the voltage amplifier. The disturbance ($\Delta\phi + \phi_0$) compensated by the proposed control system in this test was 25.2 radians, once the amplitude peak-to-peak of the analog output voltage (v_{out}) was approximately 4.8 V, the linear voltage amplifier gain (C_{LVA}) is equals to 21 V/V and the feedback PZT gain (C_{PZT}) for low frequencies is approximately 0.25 radians per volt, as will be shown in the following. Therefore the system was capable to compensate phase shifts greater than $\pi/2$ rad, while maintaining a straight line relationship between the phase shift and the control voltage signal v_{out}.

Also the phase plane of the system was acquired for the overall gain $C = 700$ and simulated for sign function, for the system operating at the sample frequency of 100 μs. The experimental data is compared to the simulated results in Figure 44, for two initial phase conditions, -2π and π rad.

Figure 43 – Open-loop and closed-loop operation

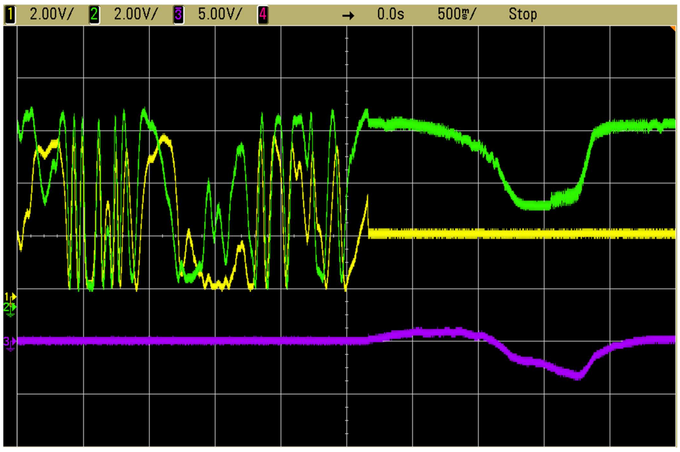

Source: elaborated by the author.

Figure 44 - Comparison between simulated and experimental phase planes

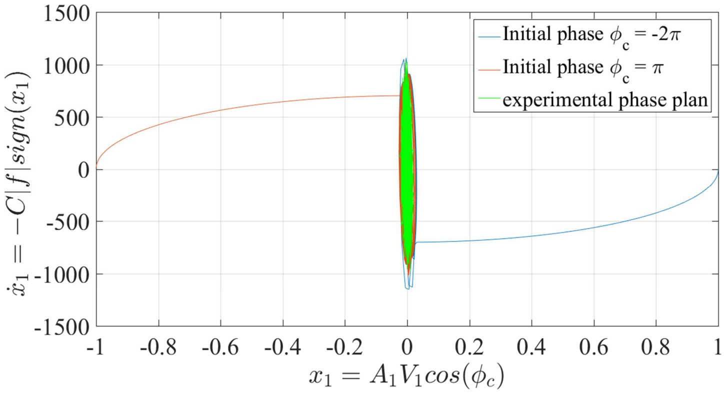

Source: elaborated by the author.

It can be seen the similarity between the behavior of the simulations with the sign function and the practical system implemented with the sigm function, showing that the mathematical modeling, and approximations used in the control law where implemented with success.

The experimental setup was then modified to include the PZT actuator PK2FVF1 (PK2) from *Thorlabs*, in replacement of the mirror indicated by the number 8 in Figure 36. This PZT stack actuator is capable to produce displacements in the order of $420\ \mu m$ for applied voltages in the range of $0 - 75\ V$. Therefore, phase shifts greater than π radians could be induced in frequencies up to 500 Hz. In Figure 45 it is shown the modified experimental setup, with the numbers 1 to 7 indicating the same optical components of Figure 37.

It is well known that the gain of PZT actuators (measured in rad/V) is a function of the input signal frequency; therefore the actuator on the feedback loop (indicated by 4) needed to be characterized. This was carried out through the low modulation index method, allied with the control system proposed in (MARTIN *et al.*, 2017), which constitutes a primary standard for calibrated nanodisplacement measurements.

Figure 45 - Bulky modified michelson interferometer

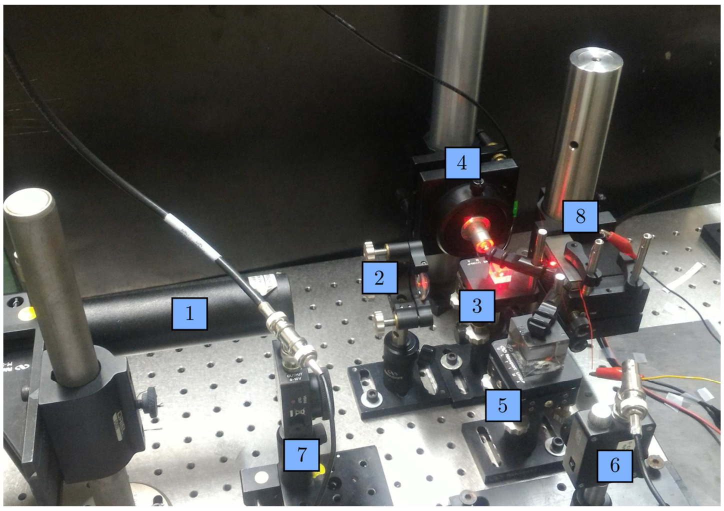

Source: elaborated by the author.

The magnitude frequency response, shown in Figure 46, was obtained from the average of five tests and then, it was used to calculate the induced phase shifts in the high gain approach. As can be seen, for the low frequency range, the linear phase-to-voltage sensitivity (or simply, the feedback PZT actuator gain) is approximately 0.25 rad/V.

Figure 46 - Frequency response of the feedback PZT actuator

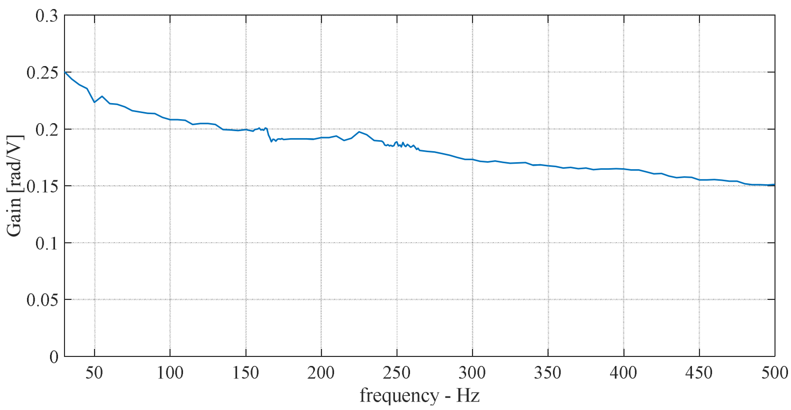

Source: elaborated by the author.

With the frequency response of the feedback actuator known, the proposed control system can be used to measure phase shifts in both modulation depths, low and high. Therefore, a sinusoidal voltage signal of 10 Hz was applied to PK2, producing a phase shift of several radians, when the system is operating in open-loop. The control system was then turned on, and the phase control signal (ϕ_c) becomes proportional to the voltage signal v_{out} applied to the input of the LVA, while the outputs of the interferometer are stabilized. In Figure 46 are presented the open- and closed-loop output signals x_1 and f, given by the green and yellow waveforms, the inverted phase control voltage signal v_{out} in pink, and the input applied voltage to the PK2 actuator on the sensor arm, in purple.

Figure 47 - Interferometer output signals in high modulation depth for applied signal at 10 Hz

(a) – Open-loop interferometer **(b) – Closed-loop interferometer**

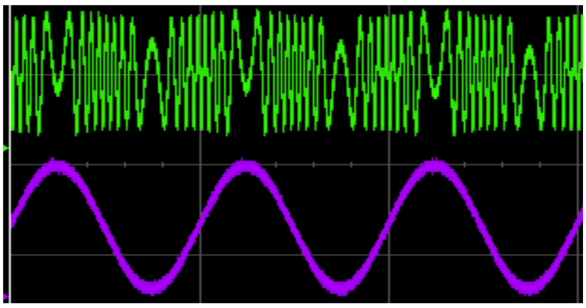

(c) – Detail of the open-loop output x_1(green) of the interferometer and the applied PZT voltage (purple).

It can be seen the multi-fringe behavior of the interferometer output signals (yellow and green) shown in Figures 47(a) and 47(c). By using fringe counting, it is observed that there are between 8 and 9 fringes between the interval of minimum and maximal applied voltage to the PK2 actuator, therefore the total phase shift (peak-to-peak) can be estimated as being between the range of $\Delta\phi_{counting} \in [50.27\ 56.55]\,rad$. Comparing now with the system operating in closed-loop with a gain $C_{sgn} = 40000$ (Figure 47(b)) one can see that multiplying the amplitude of 10 V (peak-to-peak) of the control signal by $C_{LVA} = 21\ [V/V]$ and by $C_{PZT} = 0.25\ [rad/V]$, the phase shift induced by the PZT stack actuator PK2 is $\Delta\phi = 52.5\ [rad]$, corresponding to a linear displacement of (UDD; SPILMANN, 2011) $\Delta\, l = \frac{\lambda}{4\pi}\Delta\phi = 2.64\ \mu m$. Both results are in agreement, once the phase shift measured with the control system lies within the range estimated by the fringe counting method, showing the capability of the system to measure large displacements (large enough to cause multi-fringe operation) without requiring phase-unwrapping algorithms, and with higher accuracy.

The transition from open-loop operation to closed-loop operation for sinusoidal excitation signal is shown in Figure 48(a), while a test using an arbitrary excitation signal is shown in Figure 48(b). It is important to note that for narrow-band signals the system is capable to detect phase shifts with arbitrary waveform and not only sinusoidal signals. This is an interesting feature in sensors such as gyroscopes, accelerometers and temperature sensors, among others.

Figure 48 – (a) Open- to closed-loop transition. (b) Arbitrary signal applied to PK2.

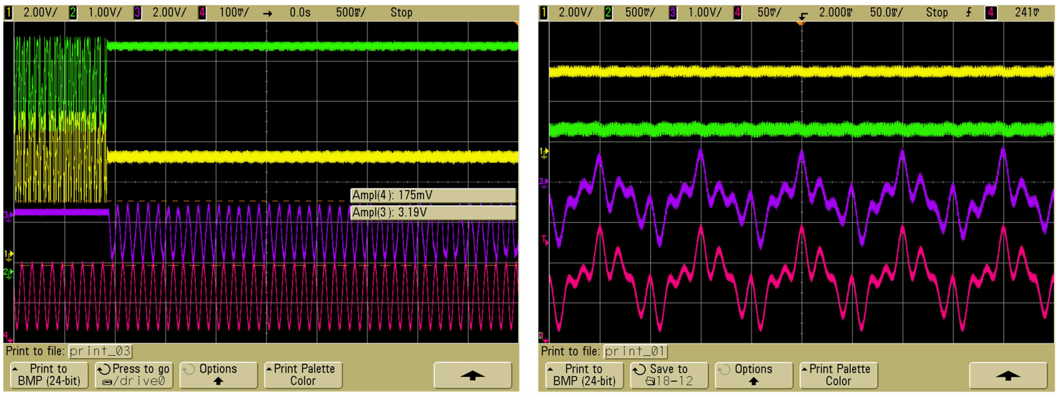

(a) (b)

Source: (elaborated by the author)

In order to verify the phase shift suppression capability of the system, for different values of gain C_{sgn}, sinusoidal signals were applied to the PZT stack actuator PK2, at different frequencies. While the system was operating in closed-loop, the amplitude of the applied voltage was increased, until the last value in which the relationship between phase control (ϕ_c) signal and the PK2 applied voltage was proportional. The obtained values of voltage amplitude (v_{out} in Figure 41) were multiplied by the gain of the linear voltage amplifier C_{LVA} and after, by the gain of the feedback PZT actuator C_{PZT} for each frequency (according to Figure 46). It can be seen, in Figure 49, that for higher values of C_{sgn}, higher amplitudes of phase shift ($\Delta\phi + \phi_0$) can be suppressed and therefore, measured through the control signal (ϕ_c) in a proportional relationship.

Figure 49 - Supressing capability for different values of gain.

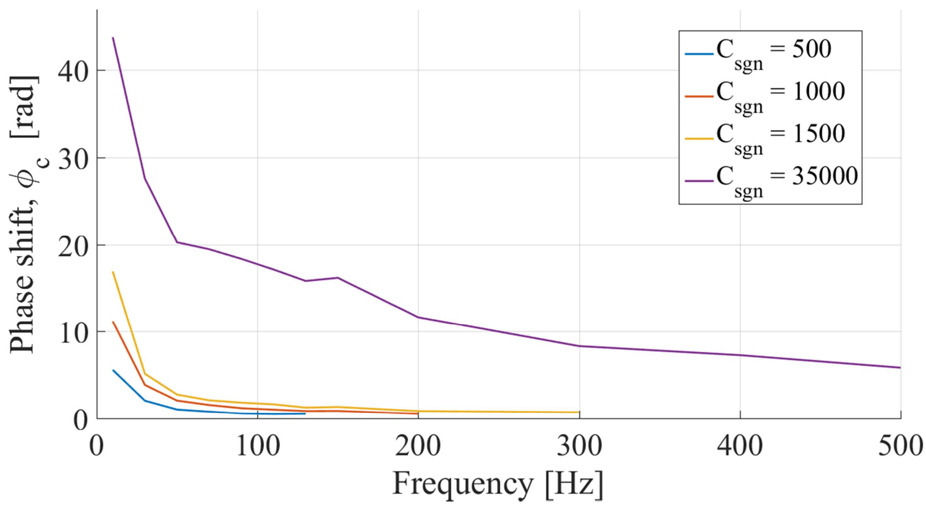

Source: elaborated by the author.

This approach was applied then, to characterize the magnitude frequency response of the PZT actuator PK2 (indicated by 8), under testing, and the results were compared with the frequency response of the same actuator obtained with the low modulation depth method, allied with the control system proposed by (MARTIN et. al, 2017). The results are shown in Figure 49.

The magnitude frequency response of PK2 was obtained for the range from 30 Hz up to 500 Hz, where the phase shift, measured as explained before, was divided by the amplitude of the voltage signal applied to PK2. This procedure was carried out on two tests in different days, resulting in the red dotted and traced green lines shown in Figure 50. The blue, yellow and traced purple lines were obtained for the same actuator (PK2) using low modulation depth associated with the control system proposed by (MARTIN, et. al., 2017).

From Figure 50 one can see the similarity between the frequency responses obtained with high gain approach and with the low modulation depth method, where a main resonance is observed near 253 Hz and anti-resonance near 280 Hz.

Also, the signals of the phase shift were plotted against the input voltage applied on PK2, showing the linearity and hysteresis of the actuator at different frequencies. The results are shown in Figures 51 to 54, together with the phase shift ϕ_0 and the mean slope. The value of ϕ_0 was obtained from the DC value of the phase correction control signal ϕ_c, and the signal of interest $\Delta\phi$ was obtained from the subtraction of ϕ_0 from the phase correction signal, therefore calculated as follows:

$$\phi_0 = \frac{1}{T}\int_{t_0}^{t_f} -\phi_c \, dt \,, \tag{165}$$

and

$$\Delta\phi = -\phi_c - \phi_0 \,, \tag{166}$$

where in (165) T is the total time of the acquired data, t_0 is the initial time and t_f the final time of the acquired data.

It is noted that, as the frequency of the applied signal approaches the resonance, of 254 Hz the phase shift curve widens (the hysteresis increases), meaning an increment in the time delay between the applied signal and the mechanical displacement generated by the PZT actuator PK2.

Figure 50 - Comparison of frequency response of the PK2FVF1 PZT actuator.

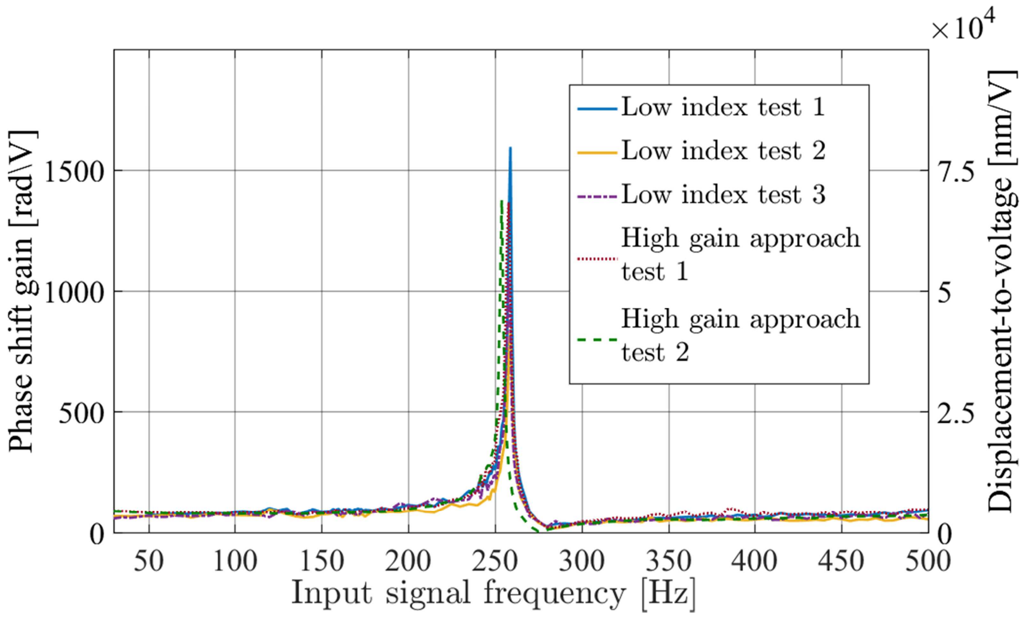

Source: elaborated by the author.

Figure 51 – Phase shift and mechanical displacement versus applied voltage signal at 30Hz.

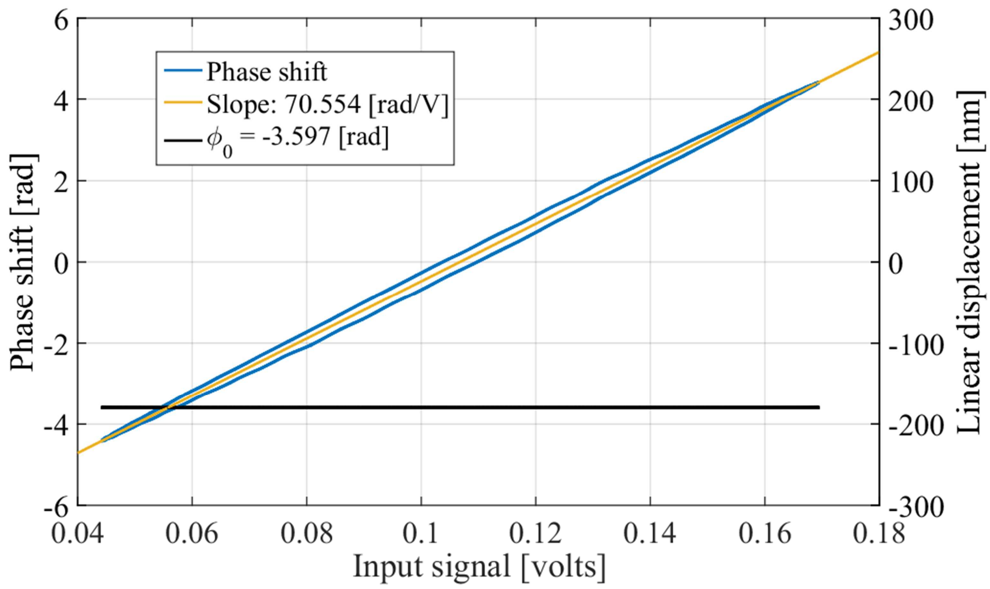

Source: elaborated by the author.

Figure 52 - Phase shift and mechanical displacement versus applied voltage signal at 250Hz.

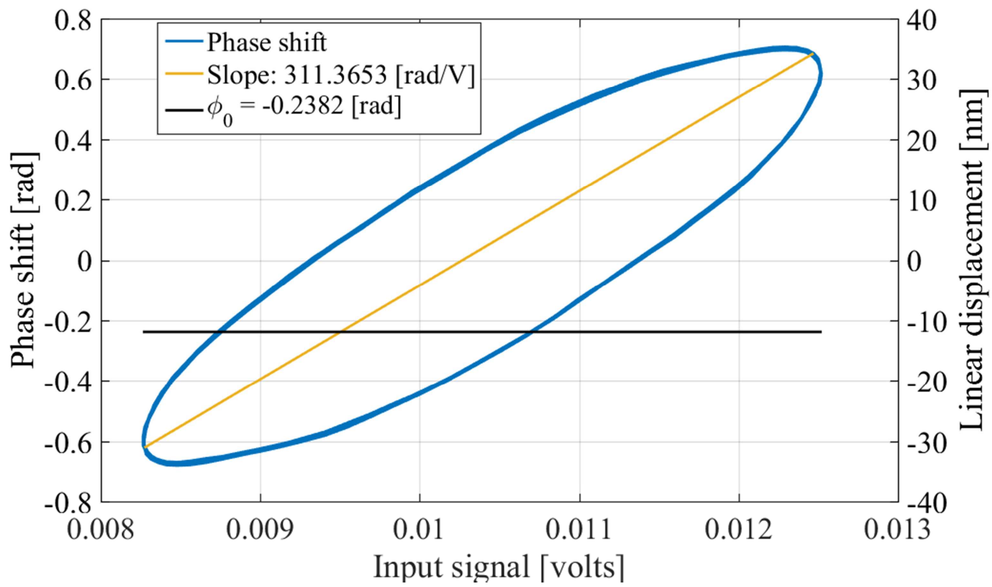

Source: elaborated by the author.

Figure 53 - Phase shift and mechanical displacement versus applied voltage signal at 254Hz.

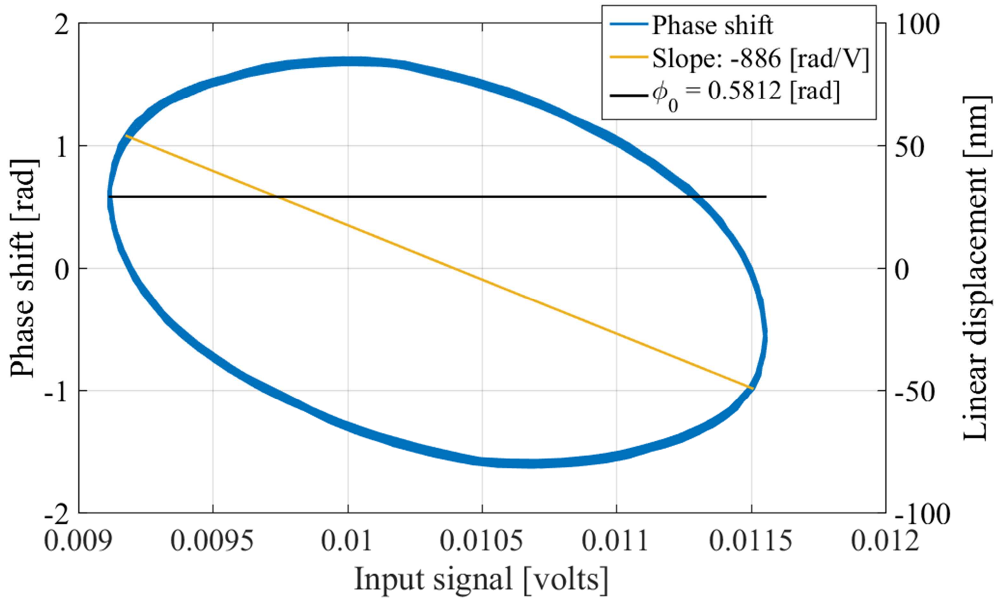

Source: elaborated by the author.

Figure 54 - Phase shift and mechanical displacement versus applied voltage signal at 258Hz.

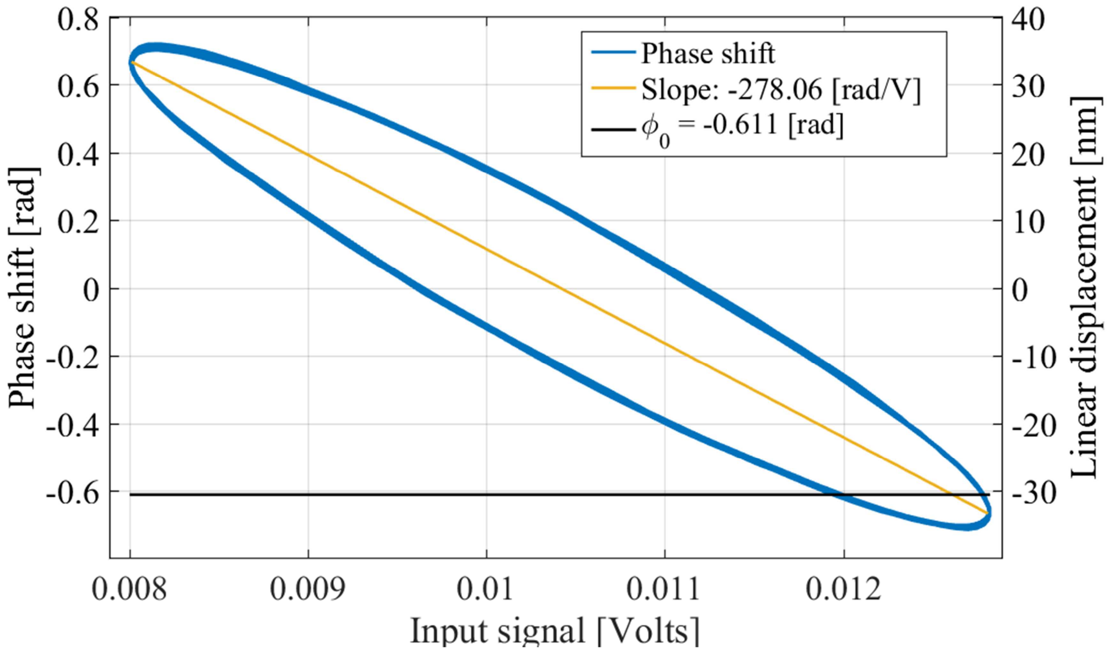

Source: elaborated by the author.

4.4 Implementation of the equivalent system virtually controlled

After the tests and experimental results obtained with the control system using the high gain approach, the equivalent system virtually controlled (see Section 3.5) was implemented in the myRIO-1900 platform. In order to facilitate and abbreviate the writing, let us refer to this system as equivalent system or ES.

As explained before, the chosen platform is subdivided into a Dual Core real-time processor and a FPGA, therefore constituting a platform of heterogeneous computing. This concept of combining different architectures and processor cores has increased the parallelism in high-performance computing. A good review of the state of the art in this topic can be found in (BRODTKORB et. al, 2010).

In order to optimize the routines and computing of the control algorithm and data logging, the overall application was divided in three tasks running concurrently, being respectively: the time critical task running on FPGA; the supervisory system running on the Desktop PC or notebook; and the task that demands a higher degree of complexity, which runs on the Dual-Core real-time processor.

On Section 4.2, the DC levels A_1 and A_2 of the output signals where determined using the procedure described in (XU et. al, 2010), and this procedure was also used in the initial implementation of the equivalent system. After the initial implementation and verification of the correct work of the application, the quadrature correction algorithm was add to the system, performing the online correction of quadrature mismatches in the output signals of the interferometer. This feature increases the practicality of operation and also the insensibility to the position variations of the photodetectors.

In order to better understand the working of the overall application, let us refer to Figure 55, where it is shown the total implemented system.

Figure 55 - Overall implementation of the equivalent system

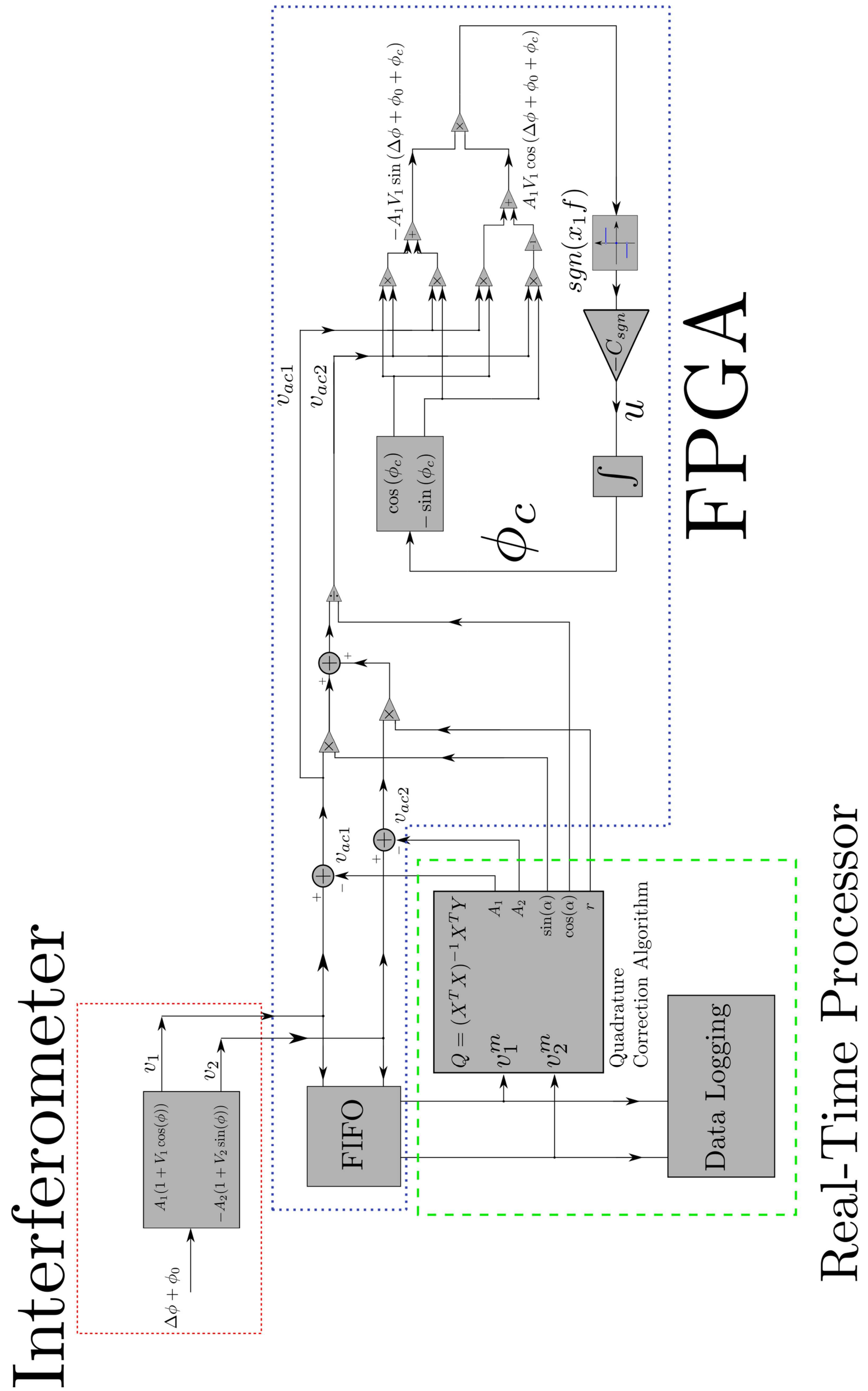

Source: elaborated by the author.

The FPGA is responsible for sampling the output signals of the open-loop interferometer, v_1 and v_2 given by (37) and (38) respectively, correcting them using the values given by the quadrature correction algorithm (Section 2.4) and then apply these signals on the control algorithm (Section 3.1), responsible for calculating ϕ_c. By the other hand, the Real-Time Processor is responsible to receive the data stored in the FIFO buffer (1000 samples of v_1 and v_2 every 100 ms) and to execute the quadrature correction algorithm, writing to the FPGA the calculated result for the parameters A_1 , A_2, r and α.

It is important to note that on initial conditions, the parameters are configured as $A_1 = A_2 = 0,\ r = 1$, and $\alpha = 0\ [rad]$, then, after 100 ms the algorithm generates the first result and updates the FPGA. The control loop is configured to 100 kHz of execution frequency, while the sampling frequency for the signals that are transferred to the FIFO is 10 kHz.

In order to be able to measure the phase correction signal ϕ_c also with the oscilloscope (Agilent, model MSO6034A), an analog output is used to convert the calculated phase correction in a voltage signal. Once the phase correction signal can assume values beyond the output voltage limits, a scale factor was used to divide ϕ_c, therefore, avoiding saturation. It is noteworthy that, as the analog output is used to measure the signal ϕ_c, and not to control a physical system, the output of the integrator does not require an anti-windup system.

The implemented system was also used to evaluate the frequency response of the PZT stack actuator PK2, where two tests were performed on different days, characterizing the frequency response of magnitude and phase of PK2 with ES. The results are shown in Figures 56 and 57 where they are compared with the results using the high gain approach.

Figure 56 - Comparison of frequency response of the PK2FVF1 PZT actuator.

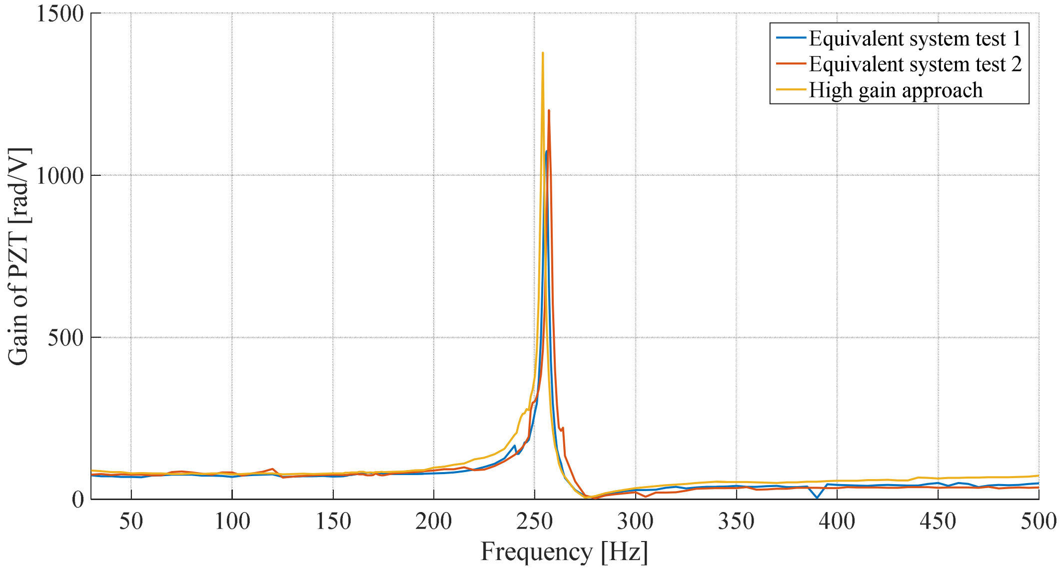

Source: elaborated by the author.

Figure 57 - Comparison of phase frequency response of the PK2FVF1 PZT actuator.

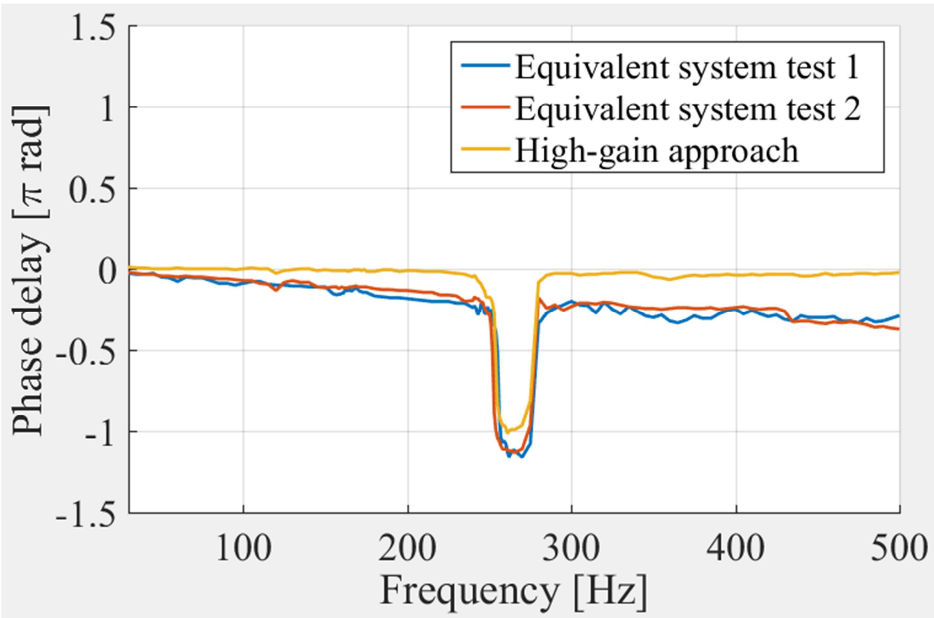

Source: elaborated by the author.

The magnitude frequency responses of Figure 55 show a great similarity between themselves and also with the results shown in Figure 49, with the presence of a resonance also around 253 Hz. However it can be seen a discrepancy between the phase frequency responses obtained with the ES virtually controlled and the obtained with the high gain approach.

When compared to the high gain approach, and due to the shape of the phase frequency responses, it is reasonable to say that this discrepancy is due to a transport delay between the input and output of the system, once that a constant transport delay does not bring distortion to the signal in time domain and its phase frequency response is a straight line with constant slope.

The control loop algorithm by itself is not responsible for a delay of such magnitude, meanwhile the quadrature correction task is executed on the real-time processor, and each time this task is accomplished, the real-time processor transfers the coefficients for the correction to the FPGA. However, this process is time consuming and subjected to an effect called jitter.

Such effect is characterized as a stochastic delay (varying around the mean value, td, following a probabilistic distribution). Therefore in order to estimate the transport delay of the implemented control system, a linear fitting operation was carried out with the data of phase frequency response from test 1, but without the interval from 175 until 280 Hz (in order to remove the phase change introduced by PZT actuator). It was obtained the value of $td = 6.4271 \times 10^{-4}\pi$ constituting a total transport delay of approximated 2 ms.

The phase frequency responses where plotted again in Figure 58, but with the influence of the transport delay compensated. These results show now a great similarity between the phase frequency responses. It is noteworthy that the result of only one test was used to estimate the transport delay and correct the phase frequency response for both tests.

Figure 58 - Phase frequency response of ES with transport delay correction.

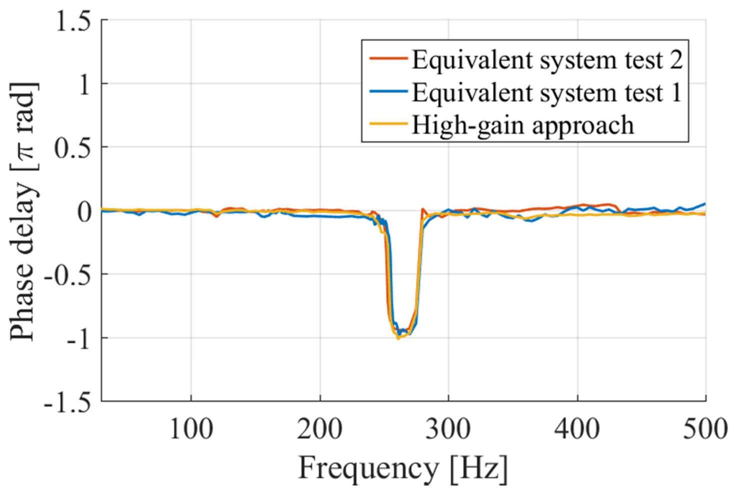

Source: elaborated by the author.

As in previous section, the signals of the phase shift were plotted against the input voltage applied on PK2, showing the linearity and hysteresis of the actuator at different frequencies; the results are shown in Figures 59 to 62, together with the phase difference ϕ_0 and the mean slope.

Figure 59 – Phase shift and mechanical displacement versus applied voltage signal at 30Hz

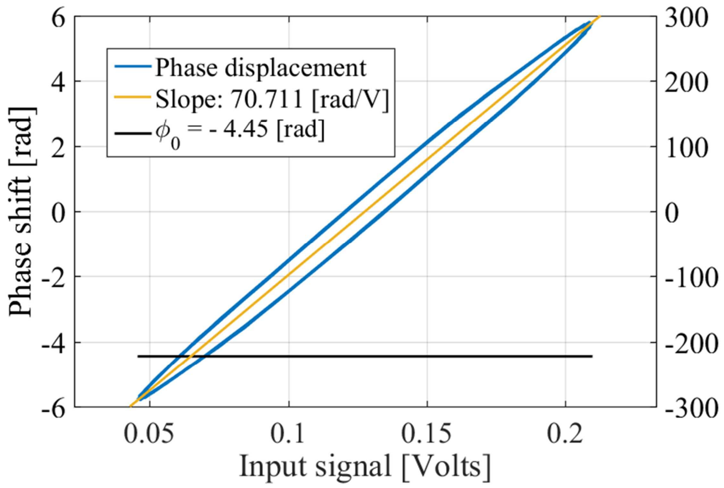

Source: elaborated by the author.

Figure 60 - Phase shift and mechanical displacement versus applied voltage signal at 250Hz.

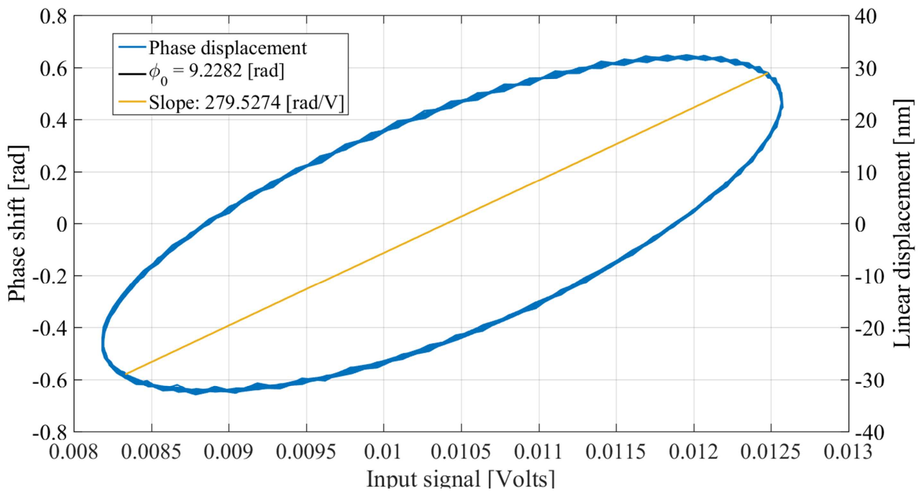

Source: elaborated by the author.

Figure 61 - Phase shift and mechanical displacement versus applied voltage signal at 255Hz.

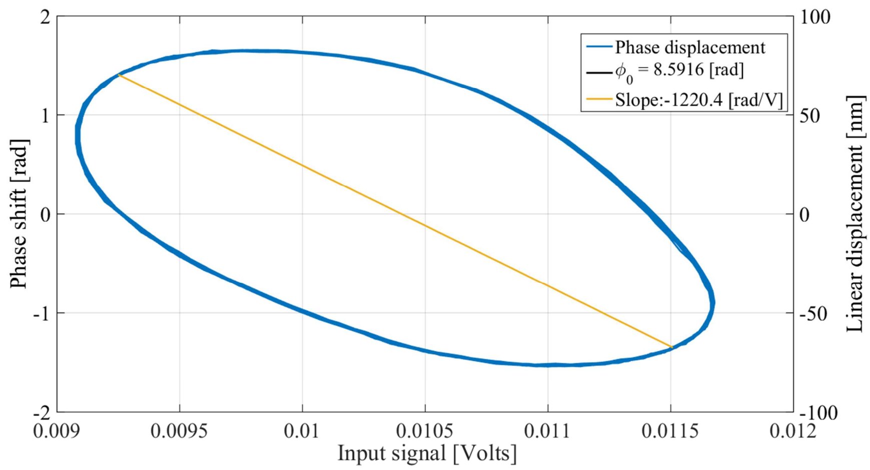

Source: elaborated by the author.

Figure 62 - Phase shift and mechanical displacement versus applied voltage signal at 258Hz

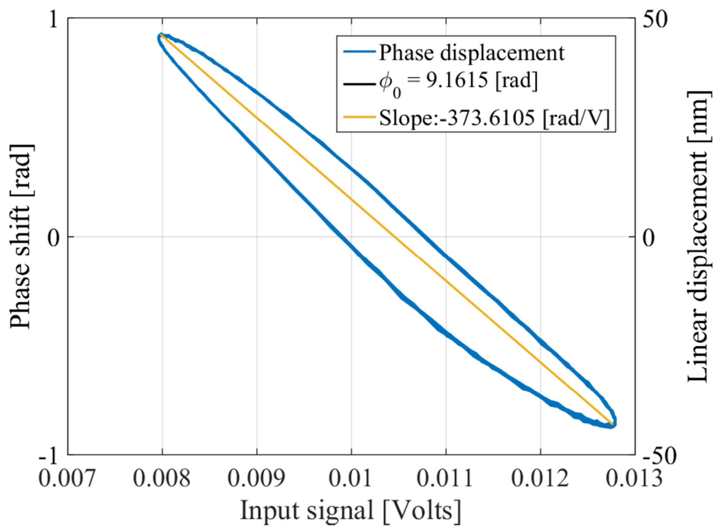

Source: elaborated by the author.

The results obtained with the ES virtually controlled also point to the presence of a resonance surrounding the frequency of 254 – 255 Hz, as it can be seen in the magnitude frequency response, in Figure 56, and by the phase shift in function of the applied voltage signal in Figures 59 to 62, where it is noted that as the frequency of the applied signal approaches the resonance, the phase shift curve widens, meaning an increment in the time delay between the applied signal and the mechanical displacement produced by the PZT actuator PK2.

4.5 Tests of the post processing algorithm

Due to technological aspects of the chosen platform, the implemented system was able to compensate phase shifts on frequencies up to 500 Hz, however some applications require higher operating frequencies. In order to show that the control law can be still applied, regarding increasing the sampling frequency, a post processing algorithm was elaborated using the software “MatLab” and tested on experimental data sampled with an oscilloscope.

In this Section, the experimental setup had two changes from the one used in Figure 44: the PZT actuator PK2 was substituted by the PFX-2 PZT flextensional actuator, which was used in previous works developed by (NADER, 2002; LEMES, 2014; SAKAMOTO, 2006; MENEZES, 2009; TAKIY, 2010), and the oscilloscope was changed to the Tektronix - TDS2024C which samples 2500 points of each channel of the presented waveforms. In Figure 62 it is presented the PFX-2 PZT actuator.

Figure 63 - PXF-2 PZT actuator.

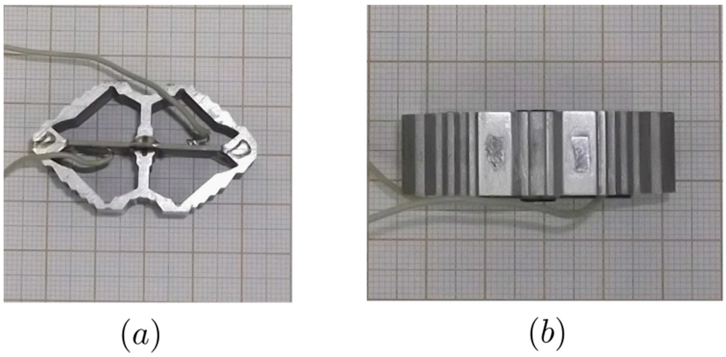

Source: (modified from MARTINEZ, 2018)

This solid state actuator operates by compliant mechanism, having no moving parts such as pins or joints. The design and manufacture of this device was performed by mechatronics group of EPUSP (Polytechnic School of the University of Sao Paulo) (NADER, 2002). It consists of a piezoceramic (PZT-5A, American Piezoceramics, 30mm x 18mm x 1mm in the directions a,b and c) coupled to a flexible aluminum structure that changes the direction of the main displacement generated by the PZT (from extensional to flexural), as well as works as a displacement transformer, amplifying its amplitude. The single piezoceramics is poled in the c direction. The flextensional actuator has four points of maximum displacement, which are the measuring points, and the displacement generated in the center of the structure is null. Due to symmetry, only one measurement point will be tested in this Section.

The results shown in the Figures 64 to 68 consist of the capture of the oscilloscope and the total phase shift $\Delta\phi + \phi_0$ demodulated, where the Channel 1 and Channel 2 of the oscilloscope are connected to the photodetectors (yellow and blue waveforms in Figure 64(a), for example), measuring the interferometric outputs x_1 and f respectively, while Chanel 3 is measuring the PZT applied voltage (purple waveform in Figure 64(a)). The blue waveform in (b) presents the total phase shift obtained with the algorithm proposed by (LEMES, 2014), while in red is the phase shift demodulated through the high-gain approach control algorithm.

In Figure 64 are shown the results for a sinusoidal voltage signal with frequency of 3 kHz applied to the PFX-2 PZT actuator, where the sampling period in this test was configured to $t_s = 0.2\ \mu$s, once the oscilloscope samples 2500 points in the total display time of $500\ \mu$s. In Figure 64(b) the overall gain was configured to $C = 5000$ and it can be seen a poor convergence with the phase demodulated from ATAN algorithm (LEMES, 2014), therefore a linear interpolation was used in the same sampled data, inserting 19 points equally distanced by $t_s/20$. The results are shown in Figures 64(c) and 64(d).

It is important to highlight that the demodulated phase presented initially an offset difference, once the phase correction sign is given by equation (78), and there is a constant term $\frac{k\pi}{2}$, where k is odd, adding $\Delta\phi + \phi_0$. This term is one of the infinity equilibrium points to which the control algorithm converges. In Figures 65 and 66, the demodulated phase shifts obtained by each method are plotted but subtracted by its minimum values, in order to remove the offset.

Figure 64 - (a) Open-loop interferometer signals. (b) $\Delta\phi + \phi_0$ demodulated by ATAN (LEMES, 2014) in blue and high-gain approach in red, C=5000. (c) signals $\Delta\phi + \phi_0$ demodulated by ATAN (LEMES, 2014) in blue and high-gain approach in red, C=5000 and dt/20. (d) Detailed view from (c) near the origin of time.

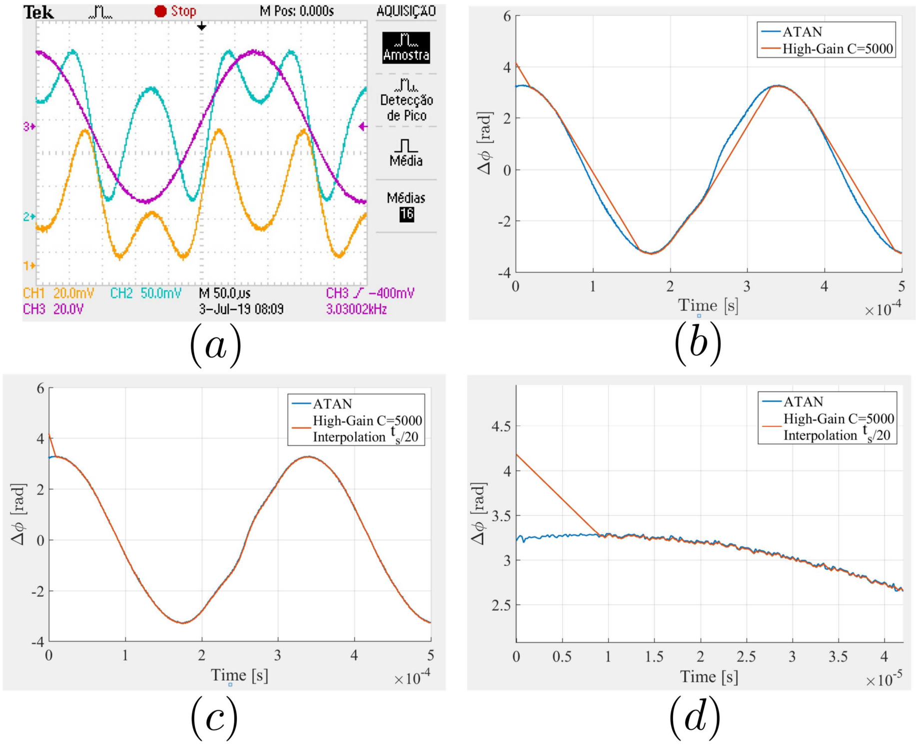

Source: (elaborated by the author)

Figure 65 - (a) Open-loop interferometric signals. (b) Demodulated phase shift using ATAN (blue) and High-gain approach (red). (c) Detail using interpolations ($t_s/50$). (d) Detail using $t_s/20$.

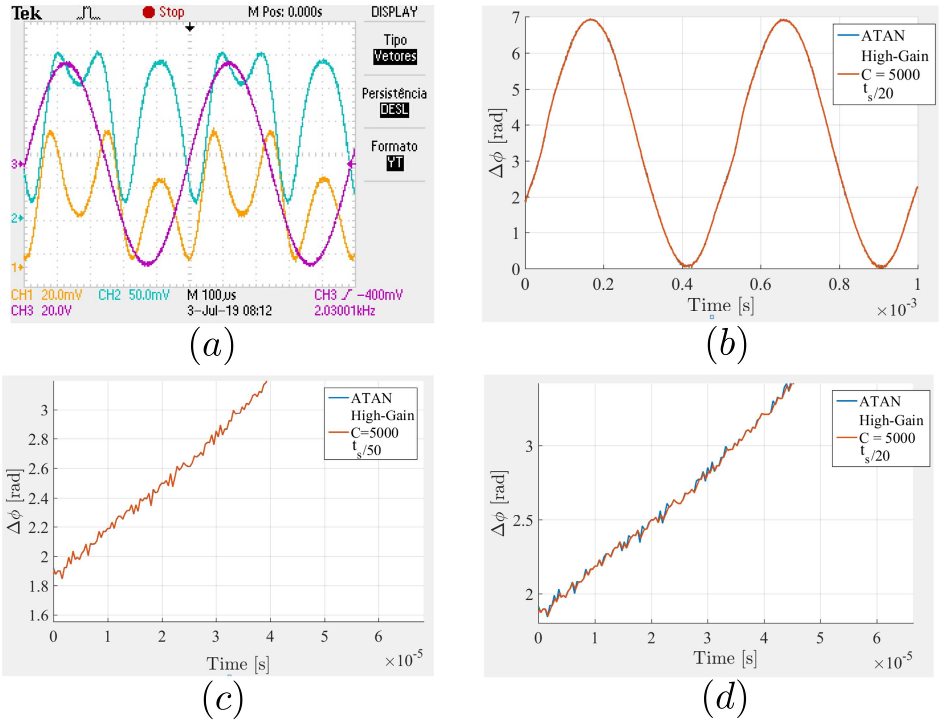

Source: (elaborated by the author)

The result shown in Figure 65(d), using linear interpolation with $t_s/20$, presents slight differences between the demodulated phases, while, using $t_s/50$ it can be seen the superposition between both demodulated phase shifts in Figure 65(c).

In the results of Figure 66(a) to (d), the test was carried out by applying an arbitrary voltage waveform with first harmonic in 2400 Hz. It can be seen that by increasing the gain C, the demodulated phase shift obtained from the high gain approach converges to the phase demodulated with the ATAN method.

Figure 66 - Tests for arbitrary signal. (a) Osciloscope data. (b) Demodulated phase shifts, C = 5000, ts/20. (c) C = 7000, ts/20. (d) C = 20000, ts/20.

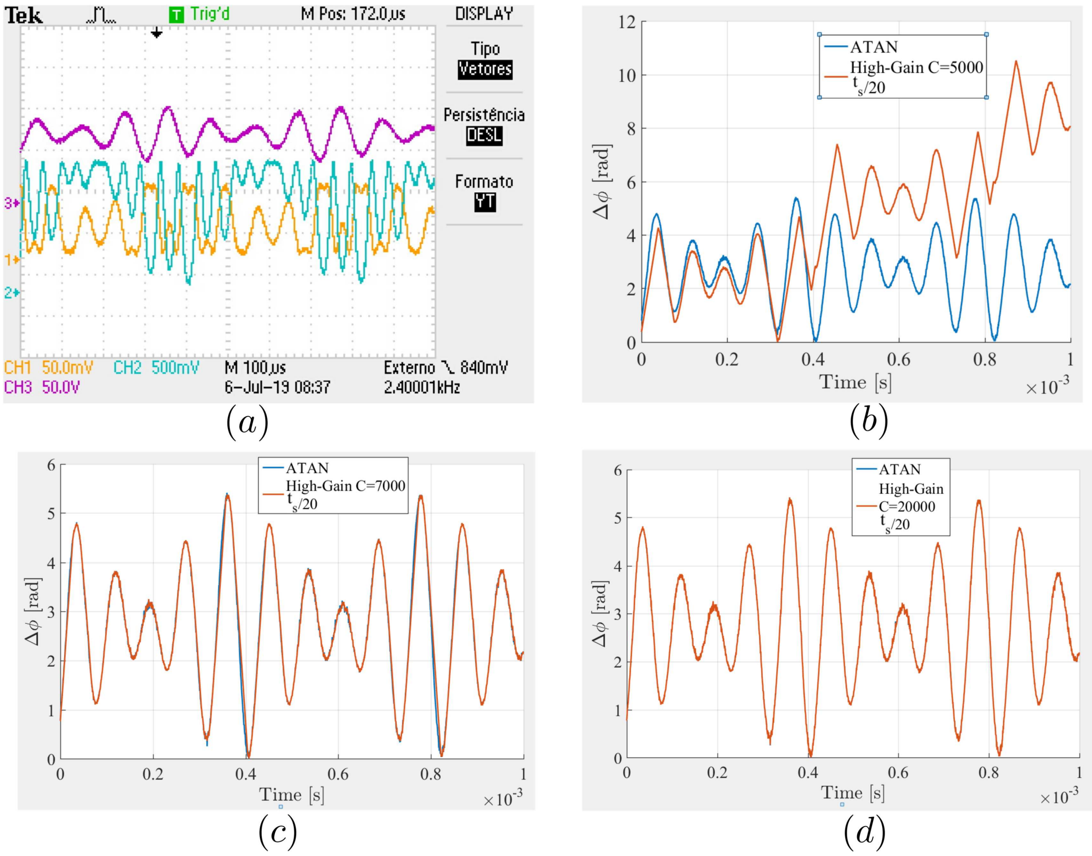

Source: (elaborated by the author)

A second test (Test 2) using an arbitrary voltage waveform applied to PFX-2 PZT was recorded and the results are shown in Figures 67 and 68. In Figure 67 it is presented the oscilloscope data, while in Figure 68 the results for the demodulated phase shift and the error between both algorithms are shown, for different number of points inserted by the interpolation. One can see the expected behavior of the error with the increase in the number of points inserted by the interpolation. The larger the number of points inserted by the interpolation smaller the thickness of the boundary layer and consequently the error.

Figure 67 - Oscilloscope data of Test 2 with arbitrary voltage signal applied to PFX-2

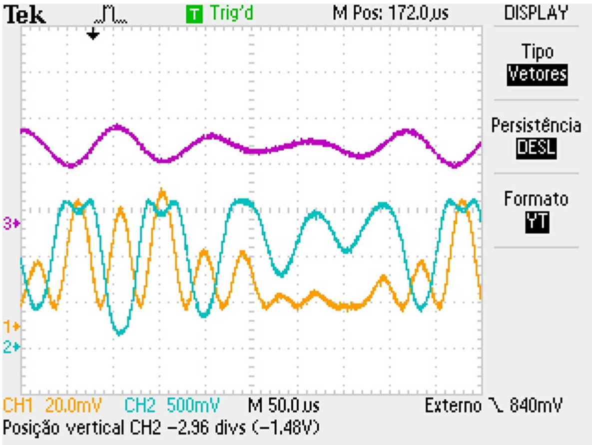

Source: (elaborated by the author)

Figure 68 - Arbitrary voltage signal applied to PFX-2. (a) Demodulated phase shift. (b) Detail of the demodulated phase shift. (c) Error between ATAN and High-gain approach for different ts. (d) Detail of (c).

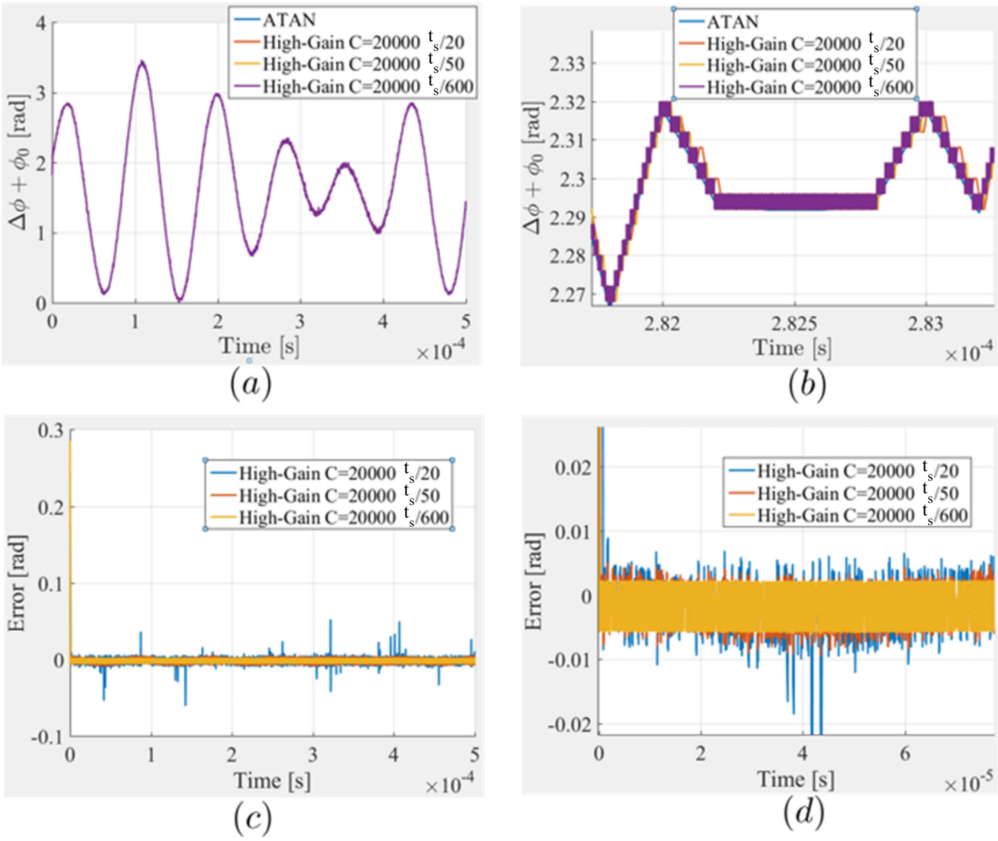

Source: (elaborated by the author)

5 Conclusion and future work

This thesis presented, firstly a theoretical study about two beam interferometry, starting from Young`s experiment and, as it was shown in the previous work of (LEMES, 2014), how spatial displacement on the fringe pattern can be used to obtain a quadrature interferometer without using complex polarizing optics.

Then, a suitable state space modeling for the interferometer was found, in order to apply a control strategy based on sliding mode control and high-gain approach. The objective of this method is to fully compensate the phase shift induced on one of the interferometers arms. The major advantages are that the induced phase shift can be retrieved from the voltage control signal, once they hold a proportional relationship. Consequently there is no need to use phase unwrapping algorithms. This leads to the capability of the system to operate in real-time. The stability of the closed system was studied, and the proposed system showed to be stable in all quadrature points.

Simulations and a theoretical study about the boundary layer were carried out to analyze the behavior of the system when changing its parameters, such as gain and sampling period. It is highlighted that for the smallest value of gain that still is greater than $|\Delta\dot{\phi} + \dot{\phi}_0|$, the sign function operating with the higher sampling frequency showed a smaller boundary layer when compared with the sigmoidal function. By the other hand, for values of gain much greater than $|\Delta\dot{\phi} + \dot{\phi}_0|$, the sigmoidal function showed smaller boundary layer, when compared to the sign function. As a drawback, the sigmoidal function decreases the robustness of the control system, representing a tradeoff between chattering and robustness. Also the behavior of the system trajectory, inside the boundary layer defined by the sigmoidal function, was studied.

In the laboratory stage, the modified Michelson interferometer was assembled, and experimental tests were carried out using the implemented control system. The results showed similarity with the simulations, and comparing with other high gain approach systems described in literature. This work showed an improvement of dynamic range and bandwidth. It is noteworthy that the results of the frequency characterization of the PZT stack actuator PK2 are in agreement with the results obtained with the low modulation depth method.

The current systems discussed in literature, operating in high-gain approach, still use the linearization around the equilibrium point, as example, utilizing PI controllers which presents the reset limitation. It is important to note that high-gain approach interferometry topologies, operating with the physically closed-loop, has as main drawback the need of a precise calibration of the PZT feedback actuator on the reference arm of the interferometer, and therefore the interferometer no more constitutes a primary standard for displacement measurements, as happens with the low gain approach versions.

Attempting to solve this problem, the new concept of the equivalent system virtually controlled showed to be a suitable alternative to measure interferometric phase shifts, presenting the great advantage of not needing a physically feedback PZT actuator and linear voltage amplifier to drive it, reducing cost and hardware requirements. The implemented quadrature correction algorithm showed to be of easy implementation, while also showed to be capable to deal with slow variations of the photodetectors error positioning. The overall system implements the feedback loop by software and therefore, the phase correction signal ϕ_c is obtained in radians. This feature allows the interferometer to be again a primary standard for calibrated displacement measurement and the system can operates in real-time.

The results obtained with the ES for the characterization of the PZT stack actuator PK2 presented an imperfection on the phase frequency response, due to a transport delay between the input and output of the implemented control system. The transport delay was experimentally determined and corrected in the phase frequency response, which does not introduce a distortion to phase correction ϕ_c.

The ES was able to operate in real-time with frequencies up to 500 Hz, however for applications that demands higher frequencies of operation it would not be suitable. In order to attempt such demands, a post processing routine based on the same algorithm used in the ES was designed, tested for higher frequency signals and compared to the algorithm proposed by (LEMES, 2014). The results shown convergence between both methods and also the error between them was presented, that can be minimized through the adjustment of the boundary layer.

The proposed next steps on the development of this work are:

a) To optimize the FPGA code of the implemented equivalent system, decreasing the length of the words of the fixed point data, while taking care to not induce significant quantization errors; change the period of quadrature correction algorithm, in order to decrease the time delay (t_d) and to change the sine and cosine functions implemented in the FPGA by look up tables. These improvements should reduce the transport delay of the system.

b) To assemble an optical fiber quadrature interferometer, in order to also apply the proposed control system.
c) To implement the strategy described by (Su; Drakunov; Özgüner, 2000), where the proposed boundary layer can be made a function of T^2 instead of only a function of T, therefore, reducing the thickness of the boundary layer and by consequence, the chattering of the system.
d) Develop a study using terminal sliding modes and discrete time sliding modes.
e) Implement the analogic version of the ES virtually controlled.
f) Develop an algorithm to adaptively change the gain and the sigmoid parameter ϵ in order to minimize the boundary layer, while obeying the reachability criterion.

It is also important to highlight that the conventional operation of interferometer based sensors working in high modulation depth mode, requires phase unwrapping algorithms in order to estimate the phase shifts unambiguously. Usually those algorithms are post processed, bringing limitations to real-time operation of the sensors. Therefore, most of the applications restrict the end of scale of the sensor to operate at low modulation depth. With the control system proposed in this work, the measurement of phase shift becomes a simple multiplication of the voltage signal applied to the feedback PZT by its frequency response, or using the ES virtually controlled, the phase shift is directly obtained from the voltage control signal. This makes the operation in high modulation depth possible without the need of phase unwrapping algorithms and therefore, increasing the maximum sensibility that could be reached.

References

AMERICAN PHYSICAL SOCIETY. **Michelson and morley**. Available in: http://www.aps.org/programs/outreach/history/historicsites/michelson-morley.cfm. Accessed in: 22 nov. 2017.

ALAOUI, A. ; MOHAMAD, A. Novel digital integrator and differentiator. **Electronics Letters**, Stevenage, v. 29, n. 4, p. 376-378, 1993.

ASTROM, K. J.; RUNDQWIST, L. Integrator windup and how to avoid it. *In*: AMERICAN CONTROL CONFERENCE IEEE, 1989, Pittsburgh. **Conference** […]. Pittisburgh: IEEE, 19898. p. 1693-1698.

BARBASHIN, E. A. **Introduction to the theory of stability**. Nauka: Wolters-Noordhoff, 1967.

BASILE, G.; BERGAMIN, A.; CAVAGNERO, G.; MANA, G. Phase modulation in high-resolution optical interferometry. **Metrologia**, Bristol, v. 28, p. 455-461, 1991.

BERGER, A.; GUTMAN, P. O. A new view of anti-windup design for uncertain linear systems in the frequency domain. **International Journal of Robust and Nonlinear Control**, Oxford, v. 26, p. 2116-2135, 2015.

BIRCH, K. P. Optical fringe subdivision with nanometric accuracy. **Precision Engineering**, Philadelphia, v. 12, n. 4, p. 195 – 198, 1990.

BORN, M.; WOLF, E. **Principles of optics**. Oxford: Pergamon Press, 1986.

BRODTKORB, A. R.; DYKEN, C.; HAGEN, T. R.; HJELMERVIK, J. M. ; STORAASLI, O. O. State-of-the-art in heterogeneous computing. **Scientific Programming**, New York, v. 18, p. 1-33, 2010.

BURTON, J. A. ; ZINOBER, A. S. Continuous approximation of variable structure control. **International Journal of Systems Science**, Abingdon, v. 17, n. 6, p. 875 – 885, 1986.

CHAO, Z.; FA-JIE, D. Closed-loop phase stabilizing and phase stepping methods for fiber-optic projected-fringe digital interferometry. **Review of Scientific Instruments**, Melville, v. 82, 6 p. 113105, 2011. Available: https://aip.scitation.org/doi/pdf/10.1063/1.3658480?class=pdf. Access in: 07 out. 2019.

CHEN, X. H.; ZENG, X. L.; FAN, D.; LIU, Q. C.; BIE, B. X.; ZHOU, X. M.; LUO, S. N. Note: phase retrieval method for analyzing single-phase displacement interferometry data. **Review of Scientific Instruments**, Melville, v. 85, 4 p., 026106, 2014. Available: https://aip.scitation.org/doi/pdf/10.1063/1.4865113?class=pdf. Access in: 07 out. 2019.

CHEUNG, D. C. L.; BARNES, T. H.; HASKEL, T. G. Feedback interferometry with membrane mirror for adaptive optics. **Optics Communications**, Amsterdam, v. 218, p. 33-41, 2003.

DAVIS, J. P. ;RABINOWITZ, P. **Methods of numerical integration**. Chelmsford: Courier Corporation, 2007. 612 p.

DENG, W.; LI, H.; ZHANG, C.; WANG, P. Optimization of detection accuracy of closed-loop optical voltage sensors based on pockels effect. **Sensors**, Basel, v. 17, n. 1723,13 p., 2017. Available: https://www.ncbi.nlm.nih.gov/pmc/articles/PMC5579804/. Access in: 07 out. 2019.

DHAR, V. K.; TICKOO, A. K.; KAUL, S. K.; KOUL, R. ; DUBEY, B. P. Artificial neural network-based error compensation procedure for low-cost encoders. **Measurement Science and Technology**, Bristol, v. 21, p. 1 – 9, 2010.

EOM, T.; KIM, J. Y.; JEONG, K. The dynamic compensation of nonlinearity in a homodyne laser interferometer. **Measurement Science and Technology**, Bristol, v. 12, 4 p., 1734-1738, 2001. Available: https://iopscience.iop.org/article/10.1088/0957-0233/12/10/318/pdf. Access in: 07 out. 2019.

ERTUGRUL, M.; KAYNAK, O.; SABANOVIC, A. ;OHNISHI, K. A generalized approach for Lyapunov design of sliding mode controllers for motion control applications. **Advanced Motion Control, Proceedings of IEEE**, Piscataway, v. 96, n. 1, 407-412, 1996.

FISHER, A. D.; WARDE, C. Simple closed-loop system for real-time optical phase measurement. **Optics Letters**, Washington, v. 4, 131-133, 1979.

FLEMING, A. J. ; ROUTLEY, B. S. A closed-loop phase-locked interferometer for wide bandwidth position sensing. **Review of Scientific Instruments**, Melville, v. 86, 7 p., 115001, 2015. Available: https://aip.scitation.org/doi/10.1063/1.4935469. Access in: 07 out. 2019.

FRITSCH, K. ;ADAMOWSKY, G. Simple circuit for feedback stabilization of a single-mode optical fiber interferometer. **Review of Scientific Instruments**, Melville, v. 52, p. 996-1000, 1981.

GAO, Z.; ZHOU, B.; HOU, B.; LI, C.; WEI, Q. ; ZHANG, R. Self-calibration of angular position sensors by signal flow networks. **Sensors**, Basel, v. 18, p. 1-18, 2018. Available: https://www.ncbi.nlm.nih.gov/pmc/articles/PMC6111312/. Access in: 07 out. 2019.

GIALLORENZI, T. G.; BUCARO, J. A.; DANDRIDGE, A.; SIEGEL, G. H.; COLE Jr., J. H.; RASHLEIGH, S. C.; PRIEST, R. G. Optical fiber sensor technology. **IEEE Transactions on Microwave Theory and Technology**, Piscataway, v. 30, n. 4, 472 – 511, 1982.

GREGORCIC, P.; POZAR, T.; MOZINA, J. Quadrature phase-shift error analysis using a homodyne laser interferometer. **Optics Express**, Washington, v. 17, n. 18, p. 16322 – 16331, 2009.

HARIHARAN, P. **Basics of interferometry**. San Diego: Academic Press, 2007.

HARIHARAN, P. **Optical interferometry**. San Diego: Academic Press, 2003.

HECHT, E. **Optics**. 4. ed. San Francisco: Addison Wesley, 2002.

HEYDEMANN, P. L. M. Determination and correction of quadrature fringe measurement errors in interferometers. **Applied Optics**, Washington, v. 20, n. 19, p. 3382-3384, 1981.

HUI, L.; LAN, B.; LIJING, L.; SHULING, H.; XIUJUAN, F.; CHUNXI, Z. Tracking algorithm for the gain of the phase modulator in closed-loop optical voltage sensors. **Optics & Laser Technology**, London, v. 47, p. 214–220, 2013.

JOHNSON, M. L. ; FAUNT, L. M. Parameter estimation by least-squares methods. **Methods in Enzymology**, Maryland Heights, v. 20, p. 1 – 37, 1992.

KAPOOR, N.; TEEL, A. R.; DAOUTIDIS, P. An anti-windup design for linear systems with input saturation. **Automatica**, Oxford, v. 34, n. 5, p. 559-574, 1998.

KARHADE, O. G.; DEGERTEKIN, F. L.; KURFESS, T. R. Active control of microinterferometers for low-noise parallel operation. **IEEE/ASME Transactions on Mechatronics**, Piscataway, v. 15, p. 1-8, 2010.

LEMES, A. S. **Novas configurações de interferômetros de quadratura e de técnicas de detecção de fase óptica baseadas em *Phase Unwrapping***. 2014. 143 f. Dissertação (Mestrado em Engenharia Elétrica) – Faculdade de Engenharia, Universidade Estadual Paulista, Ilha Solteira, 2014. Available: https://repositorio.unesp.br/handle/11449/111112. Access in: 07 out. 2019.

LI, H.; CUI, L.; WNAG, X.; LIN, Z.; ZHANG, C. “Analysis and design of loop gains to optimize the dynamic performance of optical voltage sensor based on pockels effect. **Journal of Lightwave Technology**, Piscataway, v. 33, p. 3108-3115, 2015.

LI, H.; CUI, L.; LIN, Z.; LI, L.; ZHANG, C. An analysis on the optimization of closed-loop detection method for optical voltage sensor based on pockels effect. **Journal of Lightwave Technology**, Piscataway, v. 32, p. 1006-1013, 2014.

LOZIER, J. A steady state approach to the theory of saturable servo systems. **IRE Transactions on Automatic Control**, Piscataway, v. 1, n. 1, p. 19 – 39, 1956.

LYRA, S.; MARTIN, R. I.; PEREIRA, F. C.; SILVA, E. C. N.; TEIXEIRA, M. C. M.; KITANO, C. Digital control system for two-beam optical interferometry using variable structure and sliding modes method. **Proceedings of SPIE**, v. 10917, 109171N, 2019. Available: https://www.spiedigitallibrary.org/conference-proceedings-of-spie/10917/109171N/Digital-control-system-for-two-beam-optical-interferometry-using-variable/10.1117/12.2510385.full?SSO=1. Access in: 07 out. 2019.

MARTINEZ, G. A. **Análise interferométrica da influência dos suportes de fixação de piezoatuadores ao bredboard**: alteração da resposta em frequência para nanodeslocamentos. 2018. 106 f. Dissertação (Mestrado em Engenharia Elétrica) – Faculdade de Engenharia, Universidade Estadual Paulista, Ilha Solteira, 2018. Available: https://repositorio.unesp.br/handle/11449/181661. Access in: 07 out. 2019.

MARTIN, R. I.; SAKAMOTO, J. M. S.; TEIXEIRA, M. C. M.; MARTINEZ, G. A.; PEREIRA, F. C.; KITANO, C. Nonlinear control system for optical interferometry based on variable structure control and sliding modes. **Optics Express**, Washington, v. 25, p. 6335-6348, 2017a.

MARTIN, R. I.; SAKAMOTO, J. M. S.; TEIXEIRA, M. C. M.; KITANO, C. Variable structure and sliding modes nonlinear control system applied to a fiber optic interferometer. **Proceedings SPIE**, v. 10453, 5 p., 10453W, 2017b. Available: https://www.spiedigitallibrary.org/conference-proceedings-of-spie/10453/2272548/Variable-structure-and-sliding-modes-nonlinear-control-system-applied-to/10.1117/12.2272548.full. Access in: 07 out. 2019.

MARTIN, R. I. **Nonlinear control system based on variable structure and sliding modes for two beam optical interferometry**. 2018. 127 f. Thesis (Doctorate Degree in Electrical Engineering) – Faculty of Engineering, Sao Paulo State University, Ilha Solteira, 2018. Available: https://repositorio.unesp.br/handle/11449/153459?locale-attribute=en. Access in: 07 out. 2019.

MELCHIONNI, D.; MAGNANI, A.; PESATORI, A.; NORGIA, M. Development of a design tool for closed-loop digital vibrometer. **Applied Optics**, Washington, v. 54, n. 32, p. 9637-9643, 2015.

MENEZES, J. P. C. **Análise teórica e experimental de um método interferométrico de detecção de fase óptica auto-consistente e com elevada faixa dinâmica, aplicado à caracterização de atuadores piezoelétricos flextensionais**. 2009. 146 f. Dissertação (Mestrado em Engenharia Elétrica) – Faculdade de Engenharia, Universidade Estadual Paulista, Ilha Solteira, 2009. Available: https://repositorio.unesp.br/handle/11449/87033. Access in: 07 out. 2019.

NADER, G. **Desenvolvimento de técnicas de caracterização de transdutores piezoelétricos**. 2002. 182 f. Tese (Doutorado em Engenharia Elétrica) – Escola Politécnica, Universidade de São Paulo, São Paulo, 2002. Available: https://www.teses.usp.br/teses/disponiveis/3/3132/tde-20052003-185121/pt-br.php. Access in: 07 out. 2019.

NATIONAL INSTRUMENTS. **myRIO-1900 user guide and specifications**. Available in: www.ni.com/pdf/manuals/376047a.pdf. Access in: 07 ago. 2018.

PARK, T. J.; CHOI, H. S.; HAN, C. S.; LEE, Y. W. Real-time precision displacement measurement interferometer using the robust discrete time Kalman filter. **Optics & Laser Technology**, London, v. 37, p. 229-234, 2005.

PENG, Y.; VRANCIC, D.; HANUS, R. Anti-windup, bumpless, and conditioned transfer techniques for PID controllers. **IEEE Control Systems**, Piscataway, v. 16, n. 4, 48-57, 1996.

POZAR, T.; MOZINA, J. Enhanced ellipse fitting in a two-detector homodyne quadrature laser interferometer. **Measurement Science and Technology**, Bristol, v. 22, p. 1 – 8, 2011.

RAN, M.; WANG, Q.; DONG, C. Anti-windup design for uncertain nonlinear systems subjected to actuator saturation and external disturbance. **International Journal of Robust and Nonlinear Control**, Oxford, v. 26, n. 15, p. 3421-3438, 2016.

RIBEIRO, J. M. S. **Controle discreto com modos deslizantes em sistemas incertos com atraso no sinal de controle**. 2006. 126 f. Tese (Doutorado em Engenharia Elétrica) – Faculdade de Engenharia, Universidade Estadual Paulista, Ilha Solteira, 2006. Available: https://repositorio.unesp.br/handle/11449/100364. Access in: 07 out. 2019.

RUBINOWICZ, A. Thomas young and the theory of diffraction. **Nature**, Washington, v. 180, n.4578, 160-162, 1957.

SAKAMOTO, J. M. S. **Sensor em fibra óptica aplicado à caracterização de atuadores piezoelétricos flextensionais**. 2006. 154 f. Dissertação (Mestrado em Engenharia Elétrica) – Faculdade de Engenharia, Universidade Estadual Paulista, Ilha Solteira, 2006. Available: https://repositorio.unesp.br/handle/11449/87227. Access in: 07 out. 2019.

SALEH, B. E. A.; TEICH, M. C. **Fundamentals of photonics**. New Jersey: John Wiley & Sons, 2007.

SHEEM, S. K.; GIALLORENZI, T. G.; KOO, K. Optical techniques to solve the signal fading problem in fiber interferometers. **Applied Optics**, Washington, v. 21, n. 4, p. 689-693, 1982.

SHIRAI, T.; BARNES, T. H.; HASKEL, T. G. Surface-profile measurement by means of a polarization Sagnac interferometer with parallel optical feedback. **Optics Letters**, Washington, v. 24, p. 297-299, 1999.

SLOTINE, J. J.; SASTRY, S. S. Tracking control of non-linear systems using sliding surfaces, with application to robot manipulators. **International Journal of Control**, Abingdon, v. 38, n. 2, p. 465-492, 1983.

SLOTINE, J. J. ; LI, W. **Applied nonlinear control**. New Jersey: Prentice Hall, 1991.

SU, W.; DRAKUNOV, S. V. ; ÖZGÜNER, Ü., “An O(T^2) boundary layer in sliding mode for sampled-data systems. **IEEE Transactions on Automatic Control**, Piscataway, v. 45, n. 3, 482 – 485, 2000.

TAKIY, A. E. **Análise teórica e experimental de uma nova técnica de processamento de sinais interferométricos baseada na modulação triangular da fase óptica**. 2010. 148 f. Dissertação (Mestrado em Engenharia Elétrica) – Faculdade de Engenharia, Universidade Estadual Paulista, Ilha Solteira, 2010. Available: https://repositorio.unesp.br/handle/11449/87038. Access in: 07 out. 2019.

TARBOURIECH, S.; TURNER, M. Anti-windup design: an overview of some recent advances and open problems. **IET Control Theory and Applications**, Stevenage, v. 3, n. 1, p. 1 – 9, 2009.

TURNER, M. C.; SOFRONY, J.; HERRMANN, G. An alternative approach to anti-windup in anticipation of actuator saturation. **International Journal of Robust and Nonlinear Control**, Oxford, v. 27, n. 6, p. 963-980, 2016.

UDD, E. ; SPILLMAN, W. B. J. **Fiber optic sensors**: an introduction for engineers and scientists. New York: Wiley, 2011.

UTKIN, V. I. Sliding mode control design principles and applications to electric drives. **IEEE Transactions on Industrial Electronics**, Piscataway, v. 40, n. 1, p. 23-36, 1993.

UTKIN, V. I. **Sliding modes on control and optimization**. Heidelberg: Springer-Verlag, 1992.

UTKIN, V. I. Variable structure systems with sliding modes. **IEEE Transactions on Automatic Control**, Piscataway, v. 22, n. 2, p. 212 – 222, 1977.

WU, C.; SU, C.; PENG, G. Correction of nonlinearity in one-frequency optical interferometry. **Measurement Science and Technology**, Bristol, v. 7, p. 520 – 524, 1996.

XIE, F.; CHEN, X.; ZHANG, L. High stability interleaved fiber Michelson interferometer for on-line precision displacement measurements. **Optics and Lasers in Engineering**, London, v. 47, p. 1301-1306, 2009c.

XIE, F.; CHEN, Z.; REN, J. Design and analysis of a highly stabilized optical fiber Michelson interferometer measurement system. **Sensors and Actuators A: Physical**, Washington, v. 152, p. 176-181, 2009b.

XIE, F.; CHEN, Z.; REN, J. Stabilisation of an optical fiber Michelson interferometer measurement system using a simple feedback circuit. **Measurement**, Amsterdam, v. 42, p. 1335-1340, 2009a.

XIE, J.; YAN, L.; CHEN, B.; ZHANG, S. Iterative compensation of nonlinear error of heterodyne interferometer. **Optics Express**, Washington, v. 25, n. 4470, 13 p., 2017.

XU, J.; XU, Q.; CHAI, L.; LI, Y. ; WANG, H. Direct phase extraction from interferograms with random phase shifts. **Optics Express**, Washington, v. 14, n. 2, p. 20620—20627, 2010.

YOUNG, K. D.; UTKIN, V. I. ; OZGUNER, U. A control engineer's guide to sliding mode control. **IEEE Transactions Control System Technology**, Piscataway, v. 7, n. 3, p. 328-342, 1999.

ZHENG, A.; KOTHARE, M. V.; MORARI, M. Anti-windup, design for internal model control. **International Journal of Control**, Abingdon, v. 60, n. 5, p. 1015-1024, 1994.

Appendix

Ellipse Fitting Simulation and Quadrature correction algorithm

```
A1V1 = 1; % Cossine function amplitude;

A2V2 = 3; % Sine function amplitude;

B = 5; % Amplitude of the phase displacement signal

r = A1V1/A2V2; % ratio between the amplitudes A1V1 and A2V2

A1 = 2; % offset of v_m1

A2 = 2.5; % offset of v_m2

alpha = pi/6; % Quadrature phase error

w = 3*pi/4;  % Angular frequency of the phase displacement signal

wt = 0:0.001:6*pi; % Total range of phase displacement signal

t = wt/w; % time vector

phi = B*sin(wt); % phase displacement signal
```

Ideal quadrature signals

```
v_id1 = A1V1*cos(phi);

v_id2 = A1V1*sin(phi);
```

Distorted quadrature signals (with noise)

```
noise1 = random('norm',0,0.05,[1 length(wt)]);
noise2 = random('norm',0,0.05,[1 length(wt)]);

v_m1 = v_id1 + A1 + noise1;

v_m2 = (1/r)*(v_id2*cos(alpha)+v_id1*sin(alpha)) + A2 + noise2;

% Matrix of the sampled data
X = [(v_m1').^2 (v_m2').^2 v_m1'.*v_m2' v_m1' v_m2'];

% Y matrix
Y = ones(length(t),1);

% Matrix of the coefficients Q = [A,B,C,D,E]';
Q = inv(X'*X)*(X')*Y;

% Calculated parameters
```

```
alpha_fit = asin(Q(3)/(sqrt(4*Q(1)*Q(2))));

r_fit = sqrt(Q(2)/Q(1));

A1_fit = (2*Q(2)*Q(4)-Q(5)*Q(3))/((Q(3)^2)-4*Q(1)*Q(2));

A2_fit = (2*Q(1)*Q(5)-Q(4)*Q(3))/((Q(3)^2)-4*Q(1)*Q(2));

%Corrected signals
v_d1 = v_m1-A1_fit;

v_d2 = (r*(v_m2-A2_fit)-sin(alpha_fit)*(v_m1-A1_fit))/cos(alpha_fit);

%Fitted ellipse
vd1_fit = v_id1 + A1_fit;

vd2_fit = (1/r_fit)*(v_id2*cos(alpha_fit)+v_id1*sin(alpha_fit)) + A2_fit;

% Ploting figures
figure(1);
plot(t,v_m1,t,v_m2)
set(gca,'FontSize',32,'LineWidth',1,'FontName', 'Times new roman')
xlabel('time - s');
ylabel('Simulated $v_1^m$ and $v_2^m$');

figure(2)
plot(v_m1,v_m2,vd1_fit,vd2_fit)
set(gca,'FontSize',32,'LineWidth',1,'FontName', 'Times new roman')
xlabel('time - s');
ylabel('Simulated $v_1^m$ and $v_2^m$');

figure(3)
plot(v_d1,v_d2)
set(gca,'FontSize',32,'LineWidth',1,'FontName', 'Times new roman')
xlabel('$v^d_1$');
ylabel('$v_2^d$');
```